Advanced Carbon Nanomaterials as Non-Precious Metal Catalysts for Fuel Cells

by

Pouyan Zamani

A thesis
presented to the University of Waterloo
in fulfillment of the
thesis requirement for the degree of
Doctor of Philosophy
in
Chemical Engineering

Waterloo, Ontario, Canada, 2017

Examining Committee Membership

The following served on the Examining Committee for this thesis. The decision of the Examining Committee is by majority vote.

External Examiner	Dr. Bradley Easton Professor, University Of Ontario Institute Of Technology
Supervisor(s)	Dr. Zhongwei Chen Professor, University of Waterloo
Internal Member	Dr. Mark Pritzker Professor, University of Waterloo
Internal Member	Dr. Aiping Yu Associate Professor, University of Waterloo
Internal-external Member	Dr. Bo Cui Associate Professor, University of Waterloo

Author's Declaration

This thesis consists of material all of which I authored or co-authored: see Statement of Contributions included in the thesis. This is a true copy of the thesis, including any required final revisions, as accepted by my examiners.

I understand that my thesis may be made electronically available to the public.

Statement of Contributions

This thesis is based on a combination of published works.

P. Zamani, X. Fu, J. Choi, F. Hassan, G. Jiang, D. Higgins, Y. Zhang, A. Hoque, Z. Chen, "In-Situ Polymer Graphenization Ingrained with Nanoporosity in Nitrogenous Electrocatalyst Boosting the Performance of Polymer Electrolyte Membrane Fuel Cells", *Advanced Materials*, 29 (2017) 1604456.

Dr. Fu and I synthesized the catalyst. Dr. Fu, Dr. Choi and I did the characterization and analysis of the material, as well as the writing of the paper. Dr. Hassan, Dr. Jiang, Dr. Higgins, Dr. Hoque, and Dr. Zhang all contributed in the experimental design and review.

P. Zamani, D. Higgins, F. Hassan, X. Fu, J. Choi, A. Hoque, G. Jiang, Z. Chen, "Highly active and porous graphene encapsulating carbon nanotubes as a non-precious oxygen reduction electrocatalyst for hydrogen-air fuel cells", *Nano Energy*, 26 (2016) 267-275.

Dr. Higgins, Dr. Hassan and I designed the experiment together. I carried out the lab experiments, collected and analyzed the experimental data. Dr. Higgins assisted with the writing of the paper. Dr. Choi aided in analyzing the experimental data. Dr. Fu and Dr. Hoque helped in the synthesis of the material, and Dr. Jiang helped in the manuscript revision.

H. Chung, G. Wu, D. Higgins, **P. Zamani,** Z. Chen, P. Zelenay, "Heat-Treated Non-precious Metal Catalysts for Oxygen Reduction", *Springer International Publishing*, (2016) 41-68.

Dr. Chung, Dr Wu., and Dr. Higgins, participated in the writing of the book chapter and Dr. Chen, Dr. Zelenay, and I helped in the review.

X. Fu, J. Choi, **P. Zamani**, G. Jiang, A. Hoque, F. Hassan, and Z. Chen "Co–N Decorated Hierarchically Porous Graphene Aerogel for Efficient Oxygen Reduction Reaction in Acid", *ACS applied materials & interfaces*, 8 (2016) 6488-6495.

Dr. Hassan and Dr. Fu designed the experiments, and Dr. Fu synthesized the material. Dr. Choi and I characterized and analyzed the material with Dr. Fu., Dr. Jiang and Dr. Hoque reviewed the manuscript.

D. Higgins, **P. Zamani,** A. Yu, Z. Chen, "The application of graphene and its composites in oxygen reduction electrocatalysis: a perspective and review of recent progress", *Energy & Environmental Science, 9* (2016) 357-390.

Dr. Higgins and I contributed in the writing of the review paper. Dr. Yu and Dr. Chen reviewed the manuscript.

P. Zamani, D. Higgins, F. Hassan, G. Jiang, J. Wu, S. Abureden, Z. Chen "Electrospun Iron–Polyaniline–Polyacrylonitrile Derived Nanofibers as Non–Precious Oxygen Reduction Reaction Catalysts for PEM Fuel Cells", *Electrochimica Acta, 139* (2014) 111-116.

The experiments were carried out and collected by me. Dr. Higgins, Dr. Fathy, and I analyzed the data and contributed equally to the writing of the paper. Dr. Jiang and Mr. Wu reviewed the manuscript. Dr. Abureden helped in the lab management, regular access to the lab facilities, and being trained to use them properly.

Abstract

Polymer electrolyte membrane fuel cells (PEMFCs) are electrochemical devices that efficiently convert hydrogen and oxygen into electricity and water. Their clean point of operation emissions and continuous operation have resulted in PEMFCs being highly touted as integral components of sustainable energy infrastructures, most notably in the transportation sector as a green alternative to the internal combustion engine. The issues associated with hydrogen production and distribution aside, the commercial viability of PEMFCs into the automotive sector is hindered by their high cost and inadequate long-term operational stability. The main factor behind both of these problems is the platinum-based electrocatalysts used at the cathode to facilitate the inherently sluggish oxygen reduction reaction (ORR). These expensive precious metal catalysts comprise almost half of the overall PEMFC stack cost and tend to degrade in the cathode environment that is very corrosive due to the acidic and potentiodynamic conditions. The current cost targets for PEMFCs are unattainable unless the extensive reliance on this precious metal is alleviated. The cost reduction can ultimately be accomplished by developing alternative cathode catalysts for the ORR. Research on new platinum catalyst supports or nanostructured platinum alloys to increase ORR activity on a precious metal mass basis have been largely successful. This approach is not ideal, however, due to the volatile pricing and geopolitical instabilities that can likely affect the supply of platinum. For these reasons, the development of entirely non-precious metal catalysts (NPMCs) for the ORR is highly desirable. This is the objective of this thesis, as will be presented in the following sections.

Chapter 4 describe the operation of one-dimensional nanofibers are prepared by electrospinning an iron–polyaniline/polyacrylonitrile (Fe–PANI-PAN) metal-polymer blend, followed by subsequent heat treatment. PANI was selected as it has previously been shown to be an ideal nitrogen precursor to produce some of the most active NPMCs to date, owing to its aromatic ring structure with a high content and uniform distribution of nitrogen species that can readily form nitrogen-doped graphitic carbon structures during heat treatments. PAN was also helpful as a low-cost polymer carrier to overcome the poor solubility of PANI in solution and as a secondary source of nitrogen. The addition of 10 wt. % PANI to the electrospinning mixture provides 100 and 70 mV improvements to the ORR onset potential and half-wave potential, respectively, rendering the most active NPMCs prepared by electrospinning to date. The high activity is attributed to the porous structure of the nanofibers, combined with the increased nitrogen content provided by the PANI incorporation. This unique synthetic approach, therefore, provides practical progress towards the development of one-dimensional NPMCs for PEMFC applications.

Nitrogen-functionalized graphene substances have proved to be promising electrocatalysts for the ORR due to their high activity and exceptional stability in the alkaline environment. However, they exhibit much lower catalytic activity in acidic electrolytes. Hence, in Chapter 5, a hierarchically porous Co-N functionalized graphene aerogel is provided as an active catalyst for the ORR in an acid medium. In the synthesis procedure, PANI is introduced as a pore-forming substrate to promote the self-assembly of graphene structures into the porous aerogel networks and as a nitrogen precursor to induce *in-situ* nitrogen-doping. Accordingly, a Co-N decorated graphene aerogel framework with a large surface area (485 m^2 g^{-1}) and a

plenty of meso/macropores are formed after pyrolysis. Such complex structures provide an excess amount of exposed active sites for the ORR and also ensure secure mass transfer. These advantages render significant catalytic activity with the improved onset and half-wave potentials, low peroxide yield and remarkable stability in acid medium.

In the next project (Chapter 6), we apply an ammonia treatment to tune the structure and activity of electrocatalysts derived from iron, polyaniline and carbon nanotubes (CNTs). By controlling the NH_3 reaction conditions, we were able to tune the chemistry of nitrogen incorporation, including concentration and dopant type. The final catalyst had a robust morphology consisting of highly porous 2-D *in-situ* formed graphene-like structures that, along with the intermixed 1-D CNTs, were decorated with an abundance of nitrogen and iron species. The catalyst derived under the optimized condition (F-P-C_Ar-NH900) exhibited high catalyst activity, including an $E_{1/2}$ of 0.80 V *vs* RHE through RDE testing. Under H_2-air conditions that are application-friendly, current densities of 77 mA cm^{-2} at 0.8 V and 537 mA cm^{-2} at 0.6 V were achieved. Furthermore, a maximum power density of 335 mW cm^{-2} at 0.6 V was observed. The number of electrons transferred per reduced oxygen molecule was determined to be 3.90 by RRDE indicating that the catalyst exhibited very good selectivity toward the 4-electorn transfer reaction. These electrochemical evaluations indicate that the chemical modification of Fe-PANI-CNT catalyst by NH_3 results in a highly promising Pt-free PEMFC ORR electrocatalyst.

In Chapter 7, we report the design of 3-dimensional graphitic meso-porous carbon spheres wrapped with 2-dimensional graphenized sheets. This heterostructure has a large electroactive surface area, abundant pore channels and tuned chemical structures that leads to

improved electrocatalytic performance. The nano-channels, acting as nanoscale reactors, provide easily accessible active sites, effective mass transfer and smooth charge transfer across the highly conductive carbon matrix. The obtained catalyst delivers a high maximum power density of 0.82 W cm^{-2} in a single H_2−O_2 fuel cell measurement, ranking it as one of the most promising NPMCs in PEMFCs. Moreover, fairly good fuel cell stability was also observed through accelerated degradation testing. This work provides a new avenue for NPMC design that can be a step towards practical commercial PEMFCs.

Following the previous studies, an efficient strategy of utilizing dual nitrogen sources for preparing highly active Fe-N-C electrocatalyst with in-situ formed graphene-like structures and tuned micro/meso/macro-porous morphology is reported in Chapter 8. This approach is achieved by simultaneously using PANI as a graphene precursor and introducing phenanthroline (Phen) as a pore-forming agent, followed by several post–treatments. This research was accomplished via introducing Phen into the pores of carbon support by ball-milling, which was then covered with a PANI shell through polymerization of aniline, followed by several subsequent pyrolysis and acid leaching steps leading to the formation of *in-situ* 3D porous graphene-like morphologies with multiple types of pores. Here, Phen acts as a pore-forming agent that is capable of expanding the external PANI shell during the decomposition. Simultaneously, PANI shell converted to graphene-like structures through graphenization in the presence of iron species during pyrolysis processes. Extensive physical characterization indicates the final catalyst provides rich, porous graphene frameworks decorated with uniformly dispersed active sites. The catalyst exhibits high maximum power densities of 1.06 W cm^{-2} and 0.38 W cm^{-2} in H_2−O_2 and H_2−air fuel cell tests, respectively, representing one of

the highest reported values to date for NPMCs in PEMFCs. Moreover, good fuel cell durability is also observed through accelerated degradation testing. The unprecedented performance of this electrocatalyst in fuel cell is linked to the highly porous graphene frameworks with a vast distribution of pore sizes that maximizes the number of active sites with enhanced accessibility, facilitates the mass-transport properties, and improves the carbon corrosion resistance.

Chapter 9 provides a summary of the conclusions of this body of work, along with strategies that can be engaged to capitalize on the scientific advancements made in this thesis. In summary, this research extends from catalyst synthesis to their actual use in a PEMFC, in order to develop commercially viable NPMCs. Various suggestions for prospect works are recommended in the last part of this chapter to further relate the knowledge to design highly active, durable, and low-cost NPMCs.

Acknowledgements

First and foremost, I would like to thank my supervisor, Professor Zhongwei Chen, and all of the outstanding colleagues I have had at the University of Waterloo. The support, discussions, and sharing of ideas have been crucial to research progress throughout the last several years. I have learned a lot from all of you and am very appreciative to have made some great friends during this time.

I would also like to thank my Ph.D. examining committee, including Professor Mark Pritzker, Professor Aiping Yu, Professor Bo Cui and Professor Bradley Easton (from the University Of Ontario Institute Of Technology) for their contributions to this process.

I would like to acknowledge my fiancee and family most gratefully. I also like to appreciate my friends and group members for sharing their knowledge and experiences with me. Specifically, I like to thank Dr. Fathy Hassan, Dr. Xiaogang Fu, and Dr. Drew Higgins. You all provide a constant (and important!) reminder that life is not all about scientific research, and I thank you for all the support, fun and smiles that you provide every day.

Dedication

This thesis is dedicated to my lovely fiancée, Leila, whose wisdom and support constantly encouraged me when the tasks seemed difficult and overwhelming.

Table of Contents

List of Figures

List of Tables

List of Abbreviations

Here, a list of acronyms and abbreviations are provided alphabetically:

ADT	Accelerated Durability Testing
BET	Brunauer, Emmet, Teller Adsorption Isotherm
CCM	Catalyst Coated Membrane
CHP	Combined Heat and Power
CNT	Carbon Nanotube
CV	Cyclic Voltammetry
EDX	Energy Dispersive X-ray Spectroscopy
EELS	Electron Energy Loss Spectroscopy
GDE	Gas Diffusion Electrode
GDL	Gas Diffusion Layer
GO	Graphene Oxide
HOR	Hydrogen Oxidation Reaction
HRTEM	High-Resolution TEM
ICE	Internal Combustion Engine
KJ	Ketjenblack carbon

K-L	Koutecky-Levich plot
LSCV	Linear Staircase Voltammetry
MEA	Membrane Electrode Assembly
M-N-C	transition Metal-Nitrogen-Carbon complexes
MOF	Metal Organic Framework
NPMC	Non-Precious Metal Catalyst
ORR	Oxygen Reduction Reaction
PAN	Polyacrylonitrile
PANI	Polyaniline
PEMFC	Polymer Electrolyte Membrane Fuel Cell
Phen	Phenanthroline
PPy	Polypyrrole
RDE	Rotating Disk Electrode
RHE	Reversible Hydrogen Electrode
RRDE	Rotating Ring Disk Electrode
SEM	Scanning Electron Microscopy
STEM	Scanning Tunneling Electron Microscopy
TEM	Transmission Electron Microscopy

XPS	X-ray Photoelectron Spectroscopy
XRD	X-Ray Diffraction

Chapter 1

Introduction

D. Higgins, **P. Zamani**, A. Yu, Z. Chen, *Energy & Environmental Science*, 9 (2016), 357-390

H. Chung, G. Wu, D. Higgins, **P. Zamani**, Z. Chen, P. Zelenay, *Springer International Publishing*, Electrochemistry of N4 Macrocyclic Metal Complexes, (2016), 41-68

Part of the work described in this chapter has been published as reference [1] with permission of the Royal Society of Chemistry and reference [2] with permission of Springer.

1.1 Electrochemical energy challenges

In the 21st century, the topic of energy has become one of the most important technological issues that must be addressed to guarantee the sustainability of human technologies. Global energy demands continually soar to new highs with average growth rates in the consumption of energy rising by over 50% in the 25 year period from 1987 to 2012 [3]. Fossil fuel resources are thereby being consumed at unprecedented rates, leading to greenhouse gas emissions of more than 31 billion tons of CO_2 due to the relatively "dirty" combustion process. It is clear that, as a society, we require clean transformative technologies that can revolutionize the way we produce, transport and use energy. The requirements of such technologies are no easy feat. They must be sustainable, clean, practically viable with regard to performance capabilities and efficiency, and most importantly, affordable.

Electrochemical devices have demonstrated the capacity to satisfy all of these requirements, operating with only environmentally benign emissions and boasting excellent

operational efficiencies. As one of the most capable renewable energy technologies to deal with the global energy concerns, fuel cells, principally polymer electrolyte membrane fuel cells (PEMFCs) are receiving increasing attention due to their high power density, high energy conversion efficiency, and environmental friendliness.

PEMFCs operate by converting stored chemical energy in the reactants (generally hydrogen and oxygen) into electrical energy that can be used for a variety of different purposes including transportation, stationary, and backup power applications. When operating with hydrogen produced from renewable resources, PEMFCs offer a sustainable energy conversion technology emitting only environmentally benign products water and heat, at the point of operation.

While the target markets exist and are anxiously awaiting the arrival of practically viable clean energy technologies, remaining technical challenges for PEMFCs must be addressed mostly related to cost and stability [4-8]. Cost reductions and stability improvements must be achieved to render these electrochemical devices commercially competitive with conventional technologies, such as the internal combustion engine (ICE) used in transportation applications. Although several functional components of PEMFCs work in tandem to produce electricity from the chemical energy stored in oxygen and hydrogen, the majority of cost and durability problems arise at the cathode [9-13]. This issue is most notable when the sluggish electrochemical oxygen reduction reaction (ORR) occurs and must be facilitated by catalysts that are commonly comprised of platinum or other expensive constituents. Reducing the dependency on expensive catalyst technologies can only be accomplished by developing new catalysts that can achieve improved activity and performance, while simultaneously reducing costs.

1.2 Polymer membrane electrolyte fuel cells (PEMFCs)

Fuel cells are electrochemical devices which convert chemical energy sources (often H_2 or H_2-containing fuels and O_2 from the air) directly to electricity, heat, and water, with a greater efficiency that that obtained by current means of energy conversion [4,14,15]. Among all the fuel cell systems, PEMFCs are can achieve high power densities (> l W cm^{-2}) required for portable, automobile, and stationary applications. The principal advantages of PEMFCs are their high electrical efficiencies (up to 60%), high energy densities, quiet operation and zero emissions [14,16].

A PEMFC stack consists of several cells connected in series to achieve useful voltage levels and practical power output. Each cell is comprised of three components: i) anode where the hydrogen oxidation reaction (HOR) occurs, ii) membrane which conducts protons from the anode to the cathode while being impermeable to electron flow and iii) cathode where the oxygen reduction reaction (ORR) occurs. Figure 1-1 provides a simplified schematic of what is commonly referred to as a membrane electrode assembly (MEA) [14,15].

In a typical PEMFC, hydrogen and oxygen/air continuously enter the anode (negative electrode) and the cathode (positive electrode), respectively. The fuel hydrogen undergoes the HOR at the anode (Equation 1-1):

Equation 1-1

$$H_2 \rightarrow 2H^+ + 2e^- \qquad E^o = 0\ V\ vs\ RHE$$

Following this reaction, the generated protons diffuse across the electrolyte membrane towards the cathode. In PEMFC systems, the electrolyte membrane is Nafion, a perfluorinated

sulfonic acidic polymer. The negatively charged SO_3^- groups strongly interact with the positively charged protons generated by the HOR. When the membrane is hydrated during PEMFC operation, the attraction between the protons and the SO_3^- groups weakens to provide the protons with mobility and allow them to diffuse through the membrane towards the region of lower concentration. It is a stringent requirement that the electrolyte membrane is resistant to electron flow, causing the electrons to flow through the external circuit power the attached load. After reaching the cathode, the electrons combine with the protons from the HOR along with oxygen molecules continuously fed to the cathode where the ORR occurs according to Equation 1-2:

Equation 1-2

$$O_2 + 4H^+ + 4e^- \rightarrow 2H_2O$$

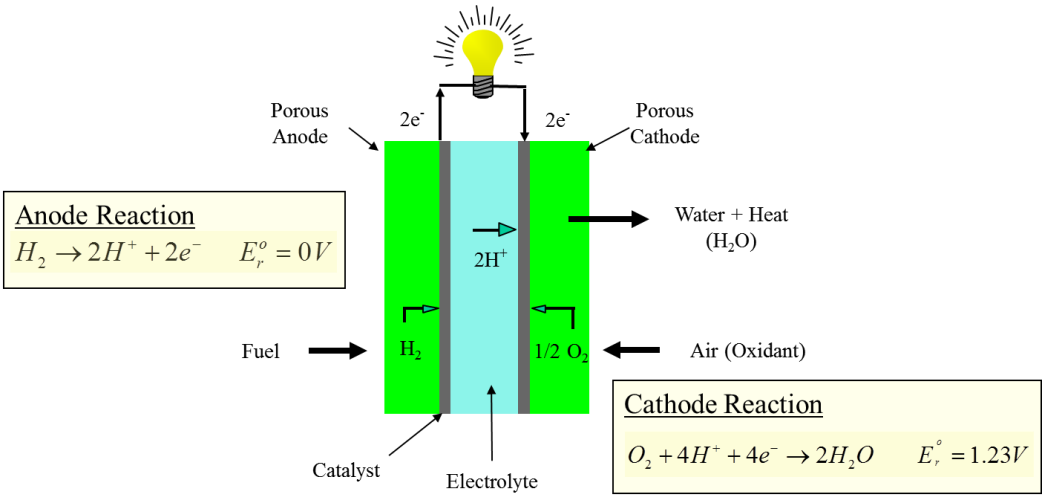

Figure 1-1 Simplified MEA and PEMFC schematic

In acidic electrolytes similar to the Nafion that is employed in PEMFCs for transportation applications, the ORR occurs either by the 4-electron reduction (Equation 1-3) the 2-electron reduction (Equation 1-4) or a combination of both. The overall 4-electron reduction mechanism is favorable owing to its obvious efficiency advantages (four electrons per oxygen molecule), and because it avoids the formation of hydrogen peroxide species in the electrode that can degrade the membrane and ionomer [17-19].

Equation 1-3

$$O_2 + 4H^+ + 4e^- \rightarrow 2H_2O$$

Equation 1-4

$$O_2 + 2H^+ + 2e^- \rightarrow H_2O_2$$

Under acidic conditions, platinum is the only catalyst that has been shown to provide suitable activity and stability to date. The acidic ORR is inherently several orders of magnitude slower than the HOR [20] and therefore, rapid oxygen reduction kinetics is a necessity from a performance standpoint. Efforts are being undertaken to develop catalysts with higher activity towards the ORR, allowing for a decrease or elimination of expensive platinum required to achieve the appropriate power output. With the HOR and ORR coinciding during PEMFC operation, the theoretical open circuit voltage is given as 1.229 V and the overall fuel cell reaction can be summarized according to Equation 1-5:

Equation 1-5

$$H_2 + {}^1\!/_2\, O_2 \rightarrow H_2O \quad E^o = 1.229\, V$$

Despite boasting a theoretical open circuit voltage of 1.229 V, the observed voltages during actual operations are always significantly lower than this value [14,15,21]. This practically lower voltage is due to a phenomenon referred to as overpotential or irreversible voltage losses that can be attributed to different factors. Figure 1-2 provides an example of a typical PEMFC polarization curve. The first thing that can be noticed from it is that the open circuit voltage (no current being drawn) is significantly lower than the theoretical 'No loss' voltage marked by the dashed line. This voltage loss can be attributed to fuel crossover across the membrane [22] and platinum catalyst oxidation to some extent.

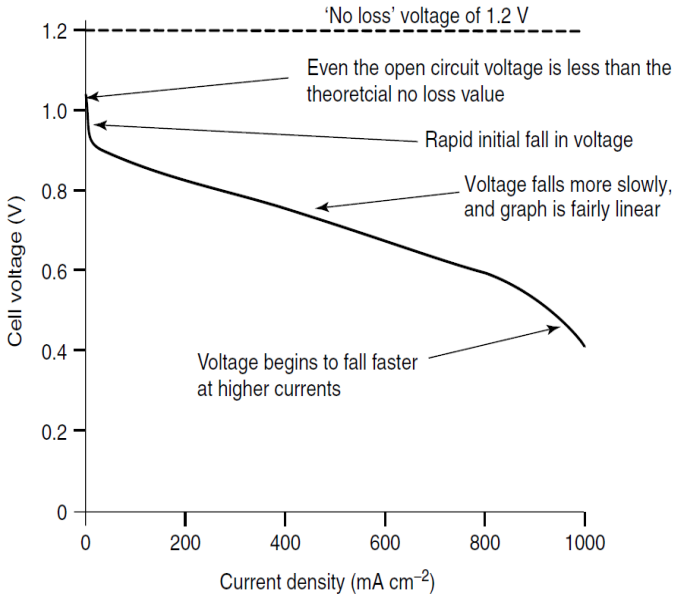

Figure 1-2 Typical PEMFC polarization curve is showing the various regions of overpotential, or irreversible voltage losses.

Reported with permission from[22] copyright John Wiley and Sons, 2003.

Moving to the region where current begins to be drawn from the PEMFC, a sharp drop in cell voltage with increasing currents is observed. This region is due to activation overpotential and is directly related to the slow kinetics of the necessary electrode reactions. This overpotential arises primarily at the cathode due to the very sluggish ORR kinetics in comparison to the HOR which involves negligible losses. Using more efficient catalysts with deliberately designed nanostructures can serve to overcome these irreversible voltage losses and is a primary research objective of scientists and engineers [23,24].

The region displaying a linear loss of cell voltage with increasing currents in the polarization curve in Figure 1-2 is attributed primarily to ohmic losses. The sources of resistance in PEMFCs can arise from the polymer electrolyte, cell connections or bipolar plates. These issues can be mitigated by appropriate selection of materials, including electrode structures with high conductivity [23,24].

Finally, at substantial current densities, the voltage of the PEMFC will drop off dramatically as observed in Figure 1-2. This behavior arises because the necessary electrode reactions are proceeding at a rate faster than the reactants can be delivered to the catalyst surface. Using pure reactant feeds, or increased gas pressures can help to mitigate this occurrence, but also using well-designed catalyst layer architectures conducive to good reactant flow and accessibility will increase the current densities attainable in a PEMFC system [23,24].

1.3 Advantages and Limitations of PEMFCs

In principle, one main characteristic of PEMFCs is high efficiency. The chemical energy is directly converted to the electrical energy which makes them more efficient than piston- or

turbine-based ICEs [15,22,25]. As fuel cells contain no moving parts except an air blower and hydrogen recirculation pump, they are very quiet and thereby, more reliable than ICEs or gas turbine power plants. This feature is of great significance in both portable power devices and local power generation in combined heat and powers (CHPs) [22,25]. Low emission is one of the most important characteristics of fuel cells. When hydrogen is used as the fuel (such as in PEMFCs), the by-product is pure water, so that a fuel cell can be 'zero emission' in practice. In these cases, no NO_2, NO_3, SO_2, or CO_2 is released in a PEMFC system and therefore, is beneficial to lower urban air pollution, ozone levels and acid rain and mitigate global warming issues. This principle advantage is of great importance, as there is a need to decrease and eliminate vehicle emissions within cities.

Despite the fact that PEMFCs have found marginal commercial success in niche markets such as backup power (i.e., telecommunications) and materials handling fleets (i.e., forklifts), [26] the ultimate target is at scale placement in the transportation area. One significant disadvantage is the preference of using hydrogen as a fuel for which no production and distribution infrastructure is currently in place. Besides the issues with storage, handling and distribution of hydrogen, two other factors limit the attractiveness of fuel cells in the automotive market: cost and durability/stability.

In order to assist PEMFC projects to the point that they can eventually be integrated into efficient and clean driving light-duty vehicles, technical targets have been defined by the U.S. Driving Research and Innovation for Vehicle efficiency and Energy sustainability (DRIVE) Fuel Cell Technical Team (FCTT). In the FCCT Roadmap [4], the technical objectives of PEMFC systems, stacks, MEAs and the various components integral to their performance are outlined. Among the different elements, the catalysts needed to expedite the proper

electrochemical reactions are the biggest contributors to PEMFC price and durability issues [8]. As electrocatalyst development is the subject of this thesis, all subsequent discussions focus on this important area of research.

When considering the mass production of 500,000 units per year, the share of the electrocatalyst is estimated to be almost half of the entire PEMFC stack cost [27]. Platinum is a precious metal with highly monopolized global distribution and is therefore does not benefit from the economy of scale production of other component substances. In order to decrease the cost of PEMFC systems, the essential platinum content must hence be lowered or ultimately replaced. Intensive studies have primarily focused on ORR catalyst development at the cathode where the ORR is several orders of magnitude slower than the anodic HOR and demands significantly higher platinum content to reach sufficient reaction rates. To minimize the platinum dependency at the cathode without sacrificing power productivity or efficiency, new catalysts must be developed with improved activity. This achievement must also be completed with a simultaneous advance in catalyst durability during long-term PEMFC service and during periods of fuel cell start-up/shutdown.

1.4 Non-precious (Non-Platinum) ORR catalysts

Currently, platinum-based catalysts are the only commercially available options for the ORR which are highly active and stable in both acidic and alkaline conditions. Thus, these catalysts are attractive options to be used in both technological applications. The issue with using platinum catalysts is their high cost which will significantly increase the cost of the device in which it is used and introduce further barriers to the commercialization of PEMFC.

The challenges with ORR catalysts emphasize the need to develop advanced materials. Three common directions have been followed in the various research and development activities to reduce or replace the platinum content and simultaneously increase the catalyst lifetime. These approaches include the development of (i) unique platinum nanoparticle supports and (ii) extended surface platinum alloy nanostructures. Although many efforts have been made to reduce the necessary amount of platinum, it does not eliminate the problem that the Earth has a small supply of platinum metal. Thus, the ultimate alternative to platinum-based catalysts is (iii) to employ non-precious metal catalysts (NPMCs) for the reduction of oxygen. The latter is the main subject of the current thesis, after providing some background and literature on recent developments of NPMCs.

The first reported research in this direction was done by Jasinksi in 1965 regarding the ORR catalytic activity of cobalt phthalocyanine [28]. Jasinski evaluated cobalt phthalocyanine as a potential cathode catalyst in KOH electrolyte and found it could catalyze the ORR. Often, this type of transition metal macrocycle catalyst [29-35] has been supported on high surface area carbon black and found to increase the stability of the catalysts significantly. Cobalt based macrocycles such as Co/phthalocyanine or Co/porphyrin have been shown to reduce oxygen through a 2-electron pathway to produce H_2O_2, whereas Fe-based macrocycles, such as Fe/phthalocyanine and Fe/porphyrin (Figure 1-3), were found to reduce oxygen through a 4-electron pathway to produce H_2O [12,30,36-38]. Although providing a new avenue of research and showing great promise, the transition metal macrocycles, such as phthalocyanines and porphyrins, exhibit extremely low stability and cannot maintain their catalytic activity after few cycles in acidic conditions [39,40].

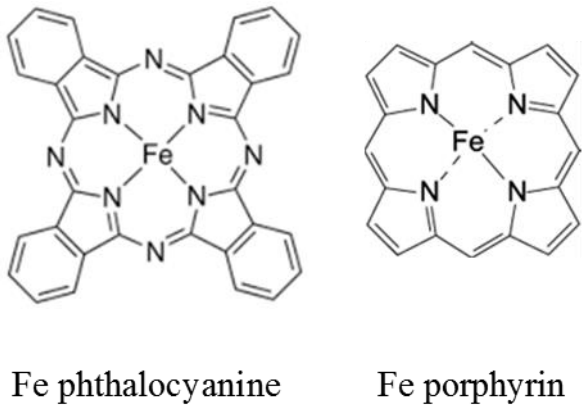

Figure 1-3 Structure of Fe/phthalocyanine and Fe/porphyrin macrocycles.

Later on, significant improvements to the stability and activity of these types of NPMCs were achieved by carrying out high-temperature pyrolysis of the carbon-supported macrocycles [12,36,41-47]. Characterization of the resulting heat-treated catalysts indicated that the macrocycle underwent partial, if not, full decomposition of its structure. This led to significant questions regarding the active site of the heat-treated catalyst, where certain surface configurations were found after high-temperature treatment of the carbon-supported macrocycles [48,49]. By employing various spectroscopic techniques, including X-ray [50-52] and mass spectroscopy [48,49,53,54], M-N_x/Cy and N-C (M is a transition metal) surface configurations were detected and believed to represent the active sites formed after high-temperature pyrolysis [48,49]. From this knowledge, a significant breakthrough was made regarding the synthesis of heat-treated ORR catalysts when it was proposed and shown that the M-N_4 chelating structure of a macrocycle is not essential to forming active heat-treated catalysts. Instead, it is possible to synthesize active and stable ORR catalysts by pyrolyzing separate nitrogen, carbon, and transition metal precursors. A typical procedure involves filling the pores of a high surface area carbon material with a nitrogen and transition metal precursor followed by heat treatment in an inert atmosphere

at temperatures above 600 °C [12,36,55,56]. Depending on the structure of the precursors and the heating temperature, it was possible to obtain different types of surface configurations, such as M-N_2/C or M-N_4/C [48,49] which have been proposed to represent various kinds of active sites. It is also worth noting that the nature of the active sites in NPMCs is still under debate. This dispute derives from the fact that the function of the transition metal during the catalyst synthesis remains unresolved. Regardless, the catalytic activity was found to strongly depend on the synthetic chemistry, including the structure of the nitrogen precursor, transition metals, heat treatment temperatures and the inclusion of support materials (i.e., carbon black). By describing recent breakthroughs in this field, a brief outline of the synthesis pathways for such heat-treated catalysts will be provided.

1.5 Pyrolyzed M-N-C Catalysts

Carbon and nitrogen precursors, combined with iron and/or cobalt precursors and heat treated at high temperatures to yield the transition metal-nitrogen-carbon complexes (M-N-C) have been deemed the most promising class of NPMCs to date. Unfortunately, these M-N-C catalysts still suffer from insufficient activity and stability during operation that pales in comparison to platinum-based materials. It is well understood that the performance of these NPMCs is directly linked to their nanostructure [57]. To achieve well-performing catalysts, the selection of precursors, supports and synthesis conditions are critical. These factors play major roles in obtaining materials with the high activity and long-term durability required for effective catalysts [44,58].

1.5.1 Nitrogen – Carbon Precursors

Heat-treated M-N-C catalysts are currently derived from various nitrogen precursors, which can be divided into three categories: (i) C≡N-based; (ii) C-N-based; and (iii) aromatic-compound-based. According to the available experimental data, the C≡N and aromatic nitrogen precursors appear to be advantageous over the C-N based ones regarding resulting catalyst activity and durability. For example, catalysts derived from heteroatomic polymers show higher activity than catalysts obtained from simple amines, such as ethylenediamine [59]. Two types of polymer-based catalysts were systematically compared using either polyaniline (PANI) or polypyrrole (PPy) as nitrogen precursors for catalyst synthesis. Electrochemical experiments with rotating disk electrode (RDE) show a higher overpotential (smaller onset potential) for ORR with the PPy-Fe-C (~ 0.85 V vs. reversible hydrogen electrode or RHE) than with PANI-Fe-C (~ 0.91 V vs. RHE). Rotating ring disk electrode (RRDE) data further point out the superior selectivity of the PANI-based catalyst for the 4-electron reaction [60].

On the other hand, PANI-Fe-C exhibits very good stability during the 200-hour life test. The difference in the durability of the two catalysts' may be caused by the nature of the active ORR sites, water tolerance and/or other factors. There are some indications that precursors with an aromatic structure may stabilize interactions between the metal and nitrogen species that become embedded into the graphitic structure of the catalyst during heat treatment [2]. This morphology can lead to improved stability of the active reaction sites and maybe one possible reason for the much better stability of PANI-derived catalysts.

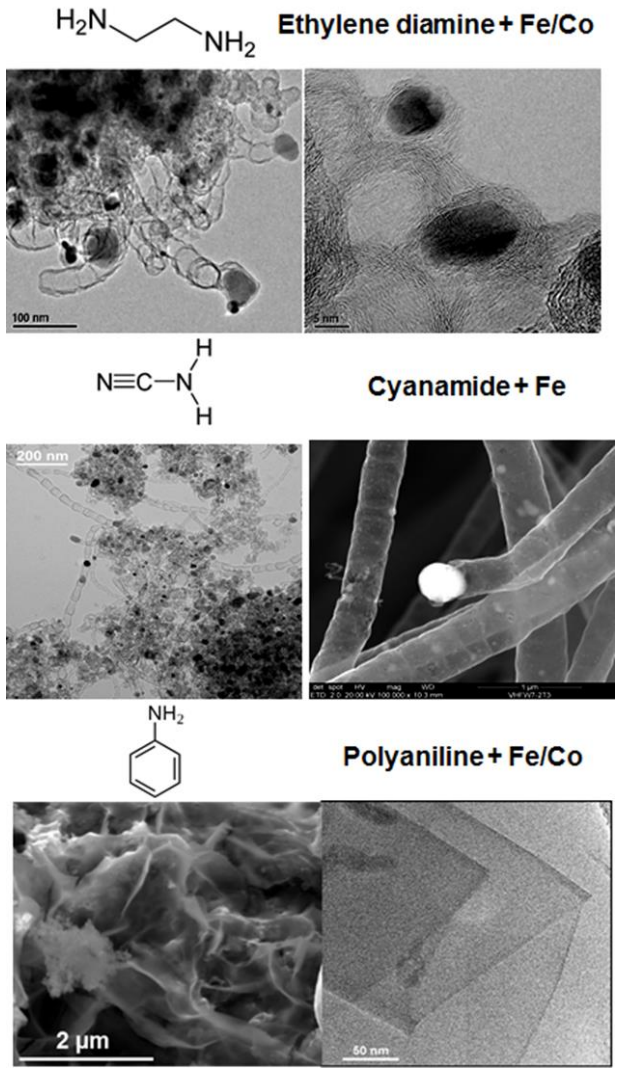

Figure 1-4 Various carbon nanostructures observed from the catalysts derived from different nitrogen precursors.

Figure 1-4 shows different carbon nanostructures that result using various nitrogen/carbon precursors during synthesis [61]. It is worth noting that no graphitized carbon structure was formed when PANI was heat treated in the absence of transition metals. This result indicates the crucial role of the transition metal in the formation of highly graphitized carbon during heat treatment. The use of ethylenediamine and Co yields an abundance of onion-

like carbon nanostructures formed during heat treatment (Figure 1-4, top). When cyanamide is used with Fe, bamboo-like carbon nanotubes tend to appear (Figure 1-4, mid part). Among the other extensively investigated precursors, PANI-derived catalysts are the only ones to demonstrate substantial graphene content following the heat treatment (Figure 1-4, bottom). This conclusion shows that the aromatic structure of PANI may be a factor in forming graphene, possibly arising due to their structural similarities.

1.5.2 Transition Metal Precursors

Metal-free nitrogen-doped carbon materials exhibit some ORR activity in alkaline media. In the more challenging acidic media, they become inactive and are not durable. The addition of transition metal is necessary to achieve good catalytic activity and improved durability [36,62]. Some studies have shown the important effect of the type of transition metal ions used during synthesis on the oxygen reduction activity. Among other approaches, this effect was demonstrated with polyacrylonitrile-derived catalysts in both acidic and alkaline solutions [63]. The nature of the metallic center in the precursors played a governing role in the resultant ORR catalysis. It has become well established that the most active catalysts in an acidic electrolyte are formed by using either iron or cobalt. Iron-derived catalysts especially lead to more positive onset potentials for the ORR than cobalt-derived catalysts, indicating higher intrinsic activity. The iron-containing catalysts also exhibit the highest 4-electron selectivity among the transition metals [63]. In alkaline media, however, iron- and cobalt-based electrocatalysts often show similar activity [63].

In a recent report [64], Liao and co-workers systematically studied the effects of the addition of transition metals (Mn, Fe, Co, Ni, Cu) on the structure and performance of doped carbon catalysts derived from PANI and melamine. The results show that the doping of these transition metals significantly affects the structures and performance of the catalysts. Doping with Fe or Mn led to catalysts with graphene-like structures, whereby doping with Co, Ni, or Cu yielded disordered structures. As shown in Figure 1-5, the doping of transition metals can enhance the performance of the catalysts. The ORR activity of these doped catalysts in acidic solution decreases in the following order: Fe > Co > Cu > Mn > Ni. It is suggested that this trend is the result of the impact that the transition metal has on three properties: (i) N content of the catalyst, (ii) amount and type of residual metal species, and (iii) resulting catalyst surface area and pore structure.

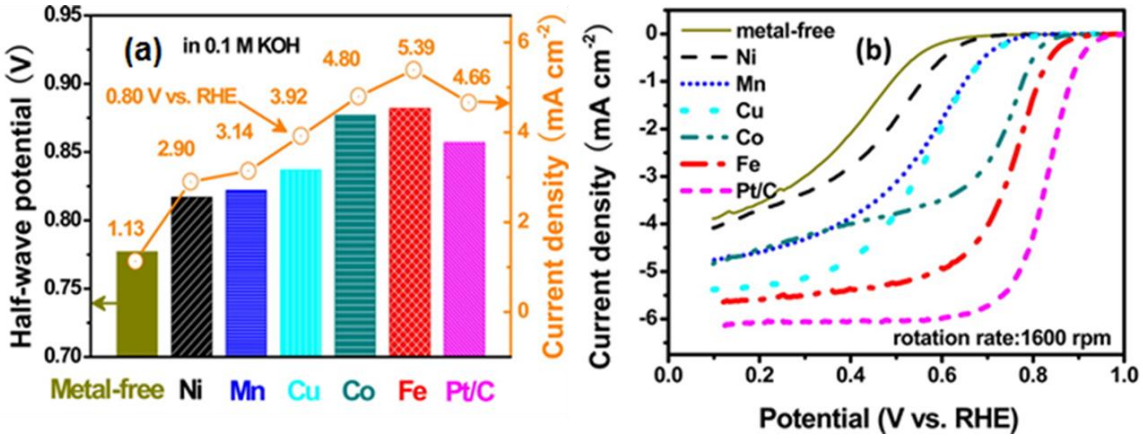

Figure 1-5 ORR polarization for catalysts derived from different transition metal precursors in (a) 0.1 M KOH and (b) 0.1 M $HClO_4$ at 298 K.

1.5.3 Mass Transport Facilitation

The cathode consists of a GDL coated with catalyst that consists usually of platinum nanoparticles dispersed on a high surface area carbon support, commonly abbreviated as Pt/C. The GDL is a carbon paper or carbon cloth that serves as the reinforcement for the electrode structure and also delivers and distributes the reactant gases over the whole electrode surface.

Boosting the ORR performance of the electrocatalysts should significantly reduce the overall platinum requirement and costs while maintaining and even improving the performance. Following the progress in enhancing the activity of the NPMCs reported in the literature, recent efforts have turned in the direction of optimizing the catalyst layer instead of strictly concentrating on ORR activity enhancements. As NPMCs are only a fraction of the cost of conventionally used precious metals, it is economically feasible to use significantly higher loadings in the catalyst layer to achieve performance targets. The NPMC layers in fuel cells are as much as 100 μm in thickness. At this length scale, mass transport through both the electrode and catalyst structures becomes an important technological challenge that must be addressed [65,66]. If the developed catalysts have poor intrinsic mass-transport properties, electrode utilization will be very poor and PEMFC performance will suffer accordingly. It has become well established that a high content of meso- and macropores are essential for the efficient transport of the ORR species [67,68]. This active transport includes the access of oxygen and proton to the catalytically active sites, along with the removal of the product water. To capitalize on the many recent advances, which have dramatically increased the intrinsic ORR activity of heat-treated M-N-C catalysts, rational meso- and macrostructure design strategies must be applied to facilitate effective mass transport. To accomplish this, a few different catalyst preparation strategies have been employed with varying degrees of success.

1.5.4 Recent Developments of M-N-C catalysts

Various approaches have been applied to sinthesize alternative NPMCs [11,12,69], such as metal-organic framework (MOF) precursors [70], the sacrificial support method [71-75] and polymerization of nitrogen-containing monomers (i.e., aniline) [55,57,58,76]. Serov *et al.* [75,77,78] have incorporated silica templates into the reaction mixture that consists of iron, nitrogen and carbon precursors. After a high-temperature heat treatment, the silica template particles are removed using an etchant such as hydrofluoric acid (HF). What remains are highly porous structures that are inverse replicas of the initial silica templates. By this approach, pore size and property tuning can be acheived by careful selection of the silica templates being employed. This technique not only leads to PEMFC performance gains but also can yield basic information regarding the effect of pore sizes and structures on catalyst activity and MEA performance.

Another interesting approach taken to control M-N-C catalysts structurally was first pioneered by Ma *et al.* [79] and involves MOF-derived catalysts. In this work, they heat treated an in-house prepared cobalt imidazolate MOF to prepare a catalyst that showed promising half-cell electrochemical activity towards oxygen reduction. Proietti *et al.* [65] advanced on this work by using a commercial zinc imidazolate framework mixed with 1,10-phenanthroline and iron acetate as iron and nitrogen precursors based on their previous investigations [56]. Interestingly, after an initial pyrolysis in argon and subsequent heat treatment in ammonia, they attained a highly porous catalyst resulted with high content of both mesopores and micropores [65]. This MOF approach is relatively straightforward and feasible, although only a limited number of MOFs are commercially available.

Recently, an interesting study by Wu et al. [55,57] has shown that their developed approach to preparing M-N-C catalysts using PANI as a nitrogen precursor is capable of forming a high

proportion of nitrogen-doped graphene-like structures during the pyrolysis step. Formation of this structure can only be accomplished when a transition metal precursor is included in the reaction mixture. The ability of PANI to form graphene-based structures likely arises due to the similarity between the aromatic structures of PANI and graphene.[55,57] Other carbon-nitrogen precursors, for example, amine-based ethylenediamine (EDA) [80] or melamine [81] mostly formed carbon nanotube structures. Interestingly, the abundance of graphene structures was partially credited for the increased current density at a low MEA voltage owing to the high surface areas and excellent conductivity. Improved MEA stability assessed by holding the cell potential at 0.4 V for up to 550 hours was also demonstrated. This increased stability was also attributed to the abundance of graphene sheets and bubbles. This finding is consistent with a previous report that linked increased catalyst stability with the emergence of graphene-like structures [55].

Chapter 2

Thesis objectives and approaches

The ultimate purpose of this thesis is to develop and deliver new catalyst technologies that are capable of improving the performance of PEMFCs, while simultaneously replacing the expensive platinum. The approaches to meet the objective will include the development and investigation of NPMCs derived from metal-nitrogen-carbon complexes (M-N-C) at high-temperature pyrolysis. To accomplish this, the following strategies will be pursued:

(a) Electrospinning of one-dimensional nanostructured PAN/PANI nanofibers in the presence of iron precursor

- We learned from this project that increasing nitrogen content using a rich source of N (PANI), can improve the catalytic activity.
- We then tried to use PANI and GO to form N-doped graphene structures with improved activity and durability.

(b) Apply a hydrothermal self-assembly technique to prepare a 2D porous graphene framework

- We learned from this project that N-doped graphene with open structures are very well capable to catalyze ORR.
- We then tried to form in-situ N-doped graphene structures directly from PANI

(c) Hybrid porous graphene encapsulating carbon nanotubes via high-temperature pyrolysis, acid leaching, and subsequent ammonia treatment

- We were able to optimize a heat treatment protocol to get the highest activity
- The poor durability of the catalyst could likely be due to the poor mass transfer properties of commercial CNT

(d) *In-situ* polymerization of PANI on graphitic meso-porous carbon spheres to form a 2D/3D hybrid carbon composite catalyst

- We learned that introducing nano-channels inside the carbon support can be beneficial for mass transfer of catalyst layer
- We tried to use this advantage to increase active site densities by introducing nitrogen dopants inside the pores of carbon support

(e) In-situ graphenization of dual nitrogen precursors ingrained with nanoporosity to form porous graphene-like frameworks with enhanced density and accessibility of active sites as well as facilitated mass-transport through the porous voids

- We were able to make catalyst with excellent activity and durability delivery.

This project links several critical areas of electrocatalyst research and development. Figure 2-1 depicts a simplified breakdown of the project tasks conducted throughout this thesis.

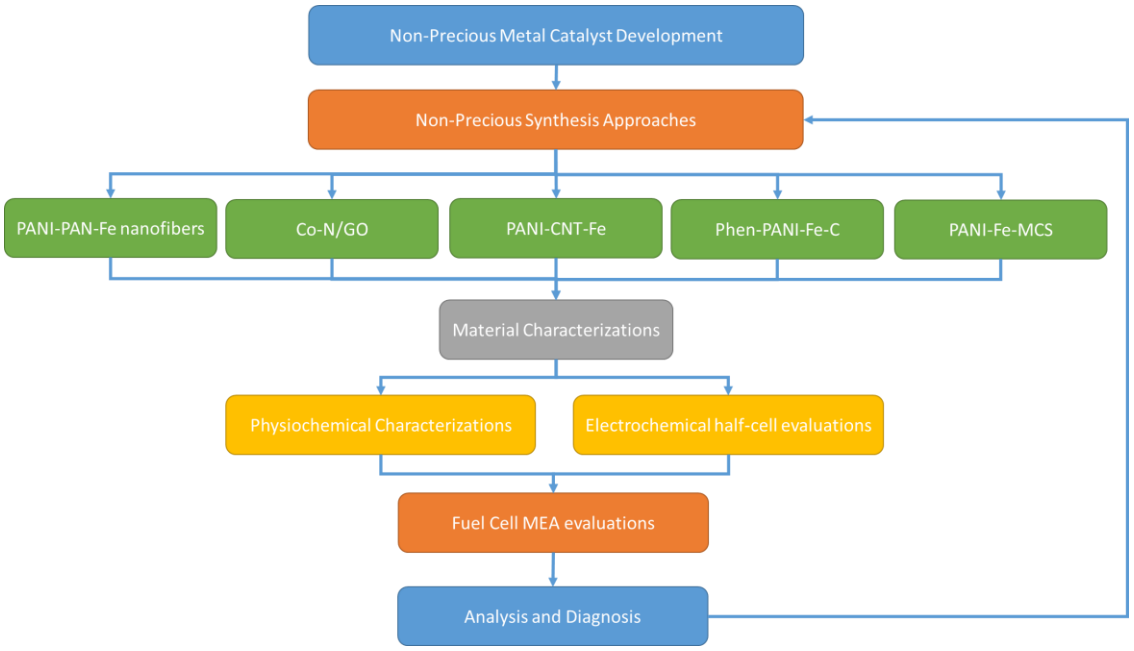

Figure 2-1 Schematic of the project workflow.

As already seen, Chapter 1 covered the background information relevant to the thesis work and Chapter 2 provides a description of the overall project objectives and task organization. Chapter 3 gives an introduction to the experimental procedures used throughout the project, with in-depth details and tasks completed within subsequent parts of the thesis. The subsequent chapters will provide details, results, and discussion about the specific work conducted throughout the entire project. Chapter 4 will introduce the reader to the development of one-dimensional nanofibers prepared by electrospinning a Fe–PANI/PAN metal-polymer blend, followed by subsequent heat treatment. The electrospinning procedure is rigorously investigated, and performance capabilities of the resulting nanofibers carefully elucidated. Chapter 5 describes the development of a hierarchically porous cobalt/nitrogen

functionalized graphene aerogel prepared via the hydrothermal method as an efficient catalyst for the ORR in an acid electrolyte. The structure and electrochemical activity of these materials are carefully evaluated and further challenges are outlined. In Chapter 6, we apply an ammonia treatment to tune the structure and activity of electrocatalysts derived from iron, polyaniline and carbon nanotubes. By controlling the reaction conditions, we are able to tune the chemistry of nitrogen incorporation, including concentration and dopant type. Chapter 8 focuses on the development of an efficient strategy of utilizing dual nitrogen sources for preparing highly active Fe-N-C electrocatalyst with *in-situ* formed graphene-like structures and tuned micro/meso/macro-porous morphology. Finally, Chapter 9 provides conclusions and summary of all the results reported in the thesis, along with recommendations for future work that can exploit the progress made throughout this thesis to improve PEMFC performance.

Chapter 3

Experimental Methods and Characterizations

3.1 Fabrication Techniques

3.1.1 Electrospinning

Electrospinning is a versatile, flexible technique that allows the continuous production of nanofibers with different constituent elements, compositions, and sizes [82,83]. Electrospinning involves the processing of a polymer/precursor solution that is loaded into a syringe and pumped at a constant rate, using the typical experimental setup illustrated in Figure 3-1. The thin syringe-capillary tip is connected to a power supply (Gamma High Voltage Research Inc. ES50P-10W) that can generate voltages in the kilovolt range (up to 50 kV). A grounded counter electrode (typically aluminum foil) is placed close to (usually 5-20cm) the syringe tip. During electrospinning, the conducting polymer solution is charged within the syringe while it is pumped at a constant rate using a syringe pump (Bio-Lynx Scientific Equipment Inc. NE-300-U). As a droplet forms on the tip of the needle, it experiences electrostatic repulsion from the build-up of surface charge and the coloumbic forces due to the applied electric potential. Due to these forces, the droplet will form into a conical shape known as a Taylor cone. Once the electrostatic forces overcome the surface tension forces in the solution, a liquid jet will be ejected towards the grounded electrode, undergoing stretching and whipping [82-84]. This phenomenon results in the formation of fibrous polymers. The electrospinning procedure

mainly depends on the solution prepared, where thicker or thinner diameter fibers can easily be produced by changing the concentration of the polymer within the solution.

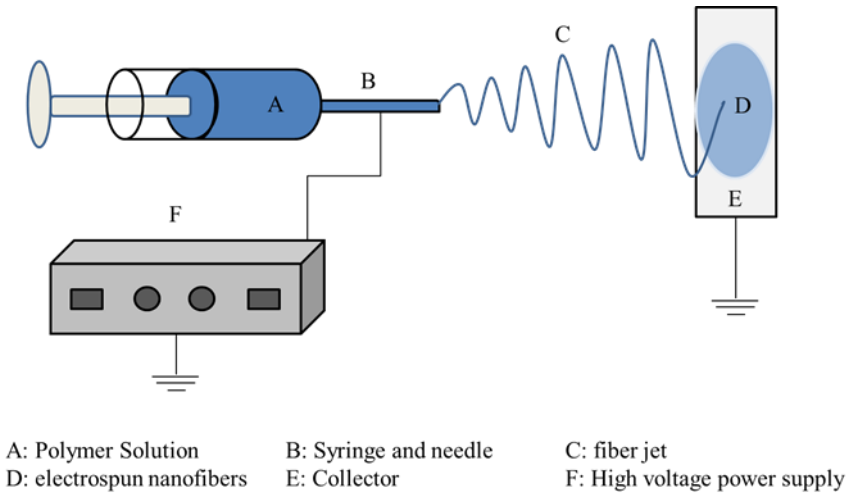

Figure 3-1 Schematic of a typical electrospinning setup

3.1.2 High-Temperature Pyrolysis

A key aspect of producing low cost highly active ORR catalysts is the use of high-temperature heating in an inert atmosphere. A typical synthesis procedure begins by loading separate nitrogen and transition metal precursors onto a carbon support. The precursors are then loaded into a quartz tube to be used in a tube furnace. The tube is saturated with N_2 or Ar gas before heated to a typical temperature range of 800 to 1000 $^{\circ}$C. There will be more detailed synthesis procedures within the following chapters.

3.2 Physiochemical Characterization Techniques

3.2.1 Scanning Electron Microscopy (SEM)

SEM is a technique allowing for high magnification imaging of samples by shooting electrons at a target and detecting the resulting deflected or generated electrons. A sample is prepared on carbon tape and stuck onto a metal stage. The stage is placed inside a vacuum chamber where an electron gun is positioned straight above. The electron gun emits electrons which are then bombarded onto the sample. An image is constructed by detecting the intensity of incoming secondary or backscattered electrons due to the bombardment from the electron gun [85]. In the proposed project, SEM (Leo FESEM 1530 located in WATLAB at University of Waterloo) will be utilized to investigate the distinct nanostructures of the fabricated electrocatalyst materials.

3.2.2 Transmission electron microscopy (TEM)

TEM allows high-resolution imaging of samples on the nanometer scale, whereby high-resolution TEM imaging can approach the atomic scale. Samples are illuminated by an electron beam with constant current density, generally produced by field emission techniques and passed through several condensers to focus it upon a slight site of interest. When the electrons come in contact with the sample, they will be scattered either elastically or inelastically and collected. Based on electron diffraction theory, the signals from the collected diffracted electrons can be processed to produce an image. With such high resolution, TEM is capable of determining nanostructures, atomic arrangements, exposed crystal facets and defects within

the structure. In this thesis, TEM (Jeol 2010F located in CCEM at Mcmaster University) will be used.

3.2.3 Energy Dispersive X-ray Spectroscopy (EDX)

Energy dispersive X-ray spectroscopy (EDX) can be carried out simultaneously with the common imaging techniques by adding an EDX detector along with SEM and TEM devices. When electrons bombard a material surface of interest, X-rays are also emitted and can be collected by the detector of EDX. The energy of the X-rays and their corresponding intensities are related to the appropriate elemental identity and quantity of a particular material. Moreover, elemental mapping can also be done by analyzing the X-rays emitted from localized positions on the sample. Atomic contents depend on the emitted X-rays intensities at various locations and can be used to map the concentration of different elements over the entirety of the sample being investigated.

3.2.4 Electron Energy Loss Spectroscopy (EELS)

In EELS, the sample is exposed to a beam of electrons with a known, narrow range of kinetic energies. Some of the electrons will undergo inelastic scattering, which means that they lose energy and have their pathways slightly turned. The quantity of energy loss can be estimated through an electron spectrometer and analyzed to determine what caused the energy loss. EELS technique is considered to be complementary to EDX, which is particularly sensitive to heavier elements. EELS system has historically been a more complicated technique

but is in principle capable of measuring atomic composition, chemical bonding, and surface properties.

3.2.5 Brunauer, Emmet, Teller Sorption Isotherm (BET)

BET adsorption/desorption isotherm analysis provides a measure of the surface area or porosity of the material. The surface area of the material is often highly significant in the development of catalysts, since a high surface area implies a high density of exposed catalytic active sites. A sample is prepared inside a glass tube, and its weight is measured. The sample is then evacuated (degassed) at roughly 200 $^{\circ}$C to remove water that may be adsorbed onto the sample surface. The sample tube is lowered to liquid nitrogen temperatures and exposed to nitrogen gas where its nitrogen adsorption/desorption isotherms are determined. From the obtained isotherms, it is possible to calculate the BET surface area and define the porosity of the material [86]. In this thesis, N_2 sorption (Micromeritics ASAP 2020 located in Advanced Carbon Nanotechnology Lab at University of Waterloo) was used.

3.2.6 X-Ray Photoelectron Spectroscopy (XPS)

XPS is the most common technique to determine the elemental composition of NPMCs. In particular, XPS is an excellent tool to ascertain the type and relative amount of nitrogen functionalities doped into carbon through deconvolution of high-resolution N1s spectra. Since ORR is strictly a surface reaction, the surface composition of the catalyst is often used to identify the catalytic active sites, which can be determined by the use of XPS. This technique

involves the use of X-rays to irradiate a sample, causing the sample to emit electrons due to the photoelectric effect. The emitted electrons exhibit specific binding energies associated with the atom where they originate. The resulting spectrum of intensity of binding energies can be used to determine the elements and the electronic state of the elements present at the surface of sample [58]. XPS spectra were collected using a Thermal Scientific K-Alpha spectrometer.

3.2.7 X-Ray Diffraction (XRD)

XRD (Rigaku MiniFlex 600 located in Applied Nanomaterials & Clean Energy Lab at University of Waterloo) is used in the research to identify the presence of metal particles or metal oxides that may be present after high-temperature treatment of the catalysts. XRD is capable of determining the crystal structure of a material by detecting diffracted X-rays and employing Bragg's Law (Equation 3-1).

Equation 3-1

$$\sin\theta = \frac{n\lambda}{2d}$$

Where n is a positive integer and λ is the wavelength of incident wave. The particular crystal structure obtained from the diffraction results can be used to link the sample to a specific material. The technique involves sweeping over a range of angles and detecting the intensity of diffracted X-rays. XRD depends on the crystallinity of substance and thus does not function when the material is amorphous [87].

3.2.8 Raman spectroscopy

Raman spectroscopy is a useful technique to obtain the information on rotational and vibrational modes in a system. The Raman effect is small but accessible by the use of lasers, and the monochromatic light of laser interacts with the molecular vibrations, photons or other excitation in the sample that results in the energy of the laser photons being shifted. Thus, the change in energy provides the information about vibrational modes in sample [58]. In this study, Raman spectroscopy is used as an important characterization tool for the investigation of defect sites in catalysts, as well as the study of the structure changes before and after heat treatments. However, the complexity of the carbon phase in such catalysts makes interpretation of Raman spectra very difficult. Raman spectra are affected by the ratio of sp^2/sp^3 bonds, crystallite size, bond-angle disorder, bond-length disorder, and heteroatoms [88] . Generally, the spectra around 1580 cm^{-1} (G band) and 1350 cm^{-1} (D band) are known to correspond to the planar motion of sp^2-hybridized carbon atoms in an ideal graphene layer and carbon atoms close to the edge of a graphene sheet, respectively [89]. The D band is inversely proportional to the crystallite size. The ratio of I_D/I_G (where "I" denotes the band intensity) is often used to measure the degree of disorder in the graphene layer. The relative concentration of amorphous carbon could be assessed from G and D bands in the Raman spectra. Raman spectroscopy was carried out on a Bruker Senterra Raman Microscope operating with a wavelength of 532 nm.

3.3 Electrochemical Characterizations

3.3.1 Half-cell rotating disc electrode testing (RDE)

Half-cell RDE testing is a well-established technique to screen the electrochemical activity of various catalyst materials. It is an ideal, simple, and fast way to investigate the catalyst materials [41]. Half-cell testing uses Pine electrochemical station (Model AFCBP-1), an electrochemical glass cell, filled with an electrolyte solution. For the present project, 0.1 M $HClO_4$ or 0.5 M H_2SO_4 will be employed as the electrolyte to simulate the acidic conditions encountered during PEMFC operation at the cathode. The electrolyte is saturated with oxygen during ORR activity testing to ensure a consistent supply of oxygen for diagnostic purposes. RDE testing utilizes three electrodes; the working electrode is a glassy carbon disc, upon which the catalyst materials are deposited. Working electrode preparation first consists of creating a catalyst ink, by ultrasonically dispersing the catalyst materials in ethanol or propanol solvent, and then drop-casting it using a pipette onto the electrode surface. After drying, the entire electrode surface area should be uniformly coated with the catalyst materials. The ionomer (Nafion) can either be incorporated directly into the catalyst ink or deposited afterward onto the prepared electrode to serve as a binder. During testing, this electrode will be immersed into the oxygen saturated electrolyte solution, and the potential will be swept while measuring current to evaluate the ORR kinetics occurring on these materials. The second electrode is a counter electrode, consisting of a platinum wire or graphite electrode immersed in the electrochemical cell to complete the circuit. The third electrode is a reference electrode used to measure the working electrode potentials. Generally, for acidic ORR evaluation, Ag/AgCl

or reversible hydrogen electrode (RHE) reference electrodes are utilized. In order to measure the ORR activity, the potential of the electrode will be swept from ca. 1.1 to 0.0 V *vs*. RHE at 10 mV s^{-1} while measuring current under saturated oxygen electrolyte conditions. Background currents obtained under saturated nitrogen conditions will be removed to account only for the Faradaic ORR. From this data, ORR electrokinetics occurring on the catalyst materials can be evaluated, whereby increased onset and half-wave potentials for the ORR and higher current densities indicate improved activity. Accelerated durability testing (ADT) was carried out by cycling the electrode in nitrogen saturated electrolyte between 0.6 and 1.0 V *vs.* RHE at 50 mV s^{-1} for several cycles. Pt/C electrode (TKK, 28.2% Pt) with a Pt loading of 20 μg cm^{-2} was measured in 0.1 M $HClO_4$ solution as benchmark.

3.3.2 Rotating Ring Disk Electrode (RRDE)

The RRDE technique is a technique often used in the electrochemical characterization of catalysts. A potential range is scanned, and the current produced is measured using a potentiostat while the electrode is rotated within an electrolyte filled cell. A catalyst ink is prepared and coated onto an electrode. A Pine RRDE containing a glassy carbon disk (5 mm diameter) and Pt ring (5.52 mm inner-diameter, 7.16 mm outer-diameter, collection efficiency N = 0.26) served as the working electrode. The electrode was designed to be able to provide two current readings; current from the disk and current from the platinum ring. The ring potential was set to 1.20 V *vs* RHE and the current is used as an indication that hydrogen peroxide was formed during the potential sweep. If oxygen is reduced within the center disk

electrode into hydrogen peroxide, the hydrogen peroxide will travel towards the outer platinum ring, and be further reduced and generate current [41].

3.3.3 Membrane electrode assembly (MEA)

MEA is a typical single cell of a PEMFC to obtain more realistic performance of catalyst and electrode. The catalyst ink is prepared by the following receipt: catalyst powder (40 mg), DDI water (0.5 mL), iso-propanol (0.5mL), and Nafion (5 wt%, 400 mg). During fabrication of MEA, catalyst materials are painted onto a 5 cm^2 Nafion 211 membrane until the obtained catalyst loading was approximately 4 mg cm^{-2}. The catalyst deposition can also be done via different techniques such as spraying, filtration or electrodeposition [90]. Commercial Pt deposited carbon cloth (0.2 mg cm−2 Pt, Fuel Cell Etc) as gas diffusion electrode (GDE) was used at the anode side. The anode GDE, Nafion membrane with brushed catalysts and gas diffusion layer (GDL, 29 BC, Ion Power) were then assembled using hot-press at 120 ^oC for 5 minutes using 600 lbs force to ensure consistent contact and adhesion without any destruction.

Fuel cell test is then done by a Model 850e fuel cell test system (Scribner Associates Inc.) at a cell temperature of 80 ^oC. Primarily, the performance evaluation is done by cycling the cell current from open circuit conditions (no current being drawn) to very high current densities. During this testing, the cell voltage is continuously monitored, resulting in an MEA polarization curve similar to the one provided previously in Figure 1-1. Several cycles are run before the performance is evaluated to ensure adequate hydration of the electrolytic membrane

and activation of the catalyst materials. H_2 and O_2 flow rates were both 300 sccm at 100% RH, and back pressure of 20 psi gauge was applied. H_2-air fuel cell durability test was conducted using an MEA fabricated with Nafion 115 ionomer membrane following the testing conditions that are suggested by the US Department of Engineering (DOE) [91]. The cell voltage was held at 0.4 V for 50 hours and the current was recorded. The cell temperature was set to 80 °C; all gases flow rates were 300 sccm and at 100 % RH; and the back pressure was 20 psi gauge on both sides. Before recording, H_2 and air were fed for 1h to condition the MEA.

EIS experiments were carried out using a potentiostat/galvanostat, Gamry Interface 5000. Measurements were conducted at a cell voltage of 0.6 V, with amplitude of 5 mV, and in the frequency range of 0.01 Hz to 100 kHz. The impedance data were obtained by calculation and simulation with Gamry software.

Chapter 4

Electrospun Fe-PANI-PAN Nanofibers

P. Zamani, D. Higgins, F. Hassan, G. Jiang, J. Wu, S. Abureden, Z. Chen, *Electrochimica Acta* 139 (2014), 111-116

Part of the work described in this chapter has been published as refrence [92], with permission from Elsevier.

4.1 Introduction

Replacing the high-cost Pt catalysts with alternative NPMCs for the ORR is highly desirable to reduce the cost of PEMFC systems [11,12]. Through extensive investigations, it is believed that the active site structure identities and concentrations are governed by precursor and synthesis technique selection [11,12,93]. However, the exact role and coordination chemistries of the individual atoms remain the subjects of debate. For different NPMCs, it is, therefore, necessary to optimize synthetic conditions to increase the ORR active site density and turnover frequency, while simultaneously providing high surface area and porosity for improved catalyst utilization [80,94].

Recently, one–dimensional nanostructured carbon materials have been used as electrocatalyst materials due to their excellent conductivity, tunable surface properties and the ability to be integrated into interconnected, highly porous electrode structures [95-97]. Nanofibers have been fabricated via several techniques such as template synthesis, self–assembly, phase

separation, and electrospinning [82]. Among these techniques, electrospinning is a highly attractive technique to reliably and cost-effectively fabricate continuous polymer nanofibers into porous web-like structures [82,98,99]. Furthermore, its simplicity renders electrospinning highly applicable to the development of NPMCs for fuel cell applications [94,100-102]. Previous studies have however been confined to metal-polyacrylonitrile (PAN) based nanofibers, that have been demonstrated in the presence of iron to provide ORR activity in both alkaline [94,103] and acidic electrolytes [102-106]. It is therefore highly desirable to investigate new synthetic strategies to prepare materials with improved ORR activity.

In this study, we investigate the incorporation of PANI precursors into Fe-PAN polymer blends (Fe-PANI-PAN) produced by electrospinning, followed by pyrolysis. This approach comprises for the first time a mixture of polymers with complementary properties has been used for electrospinning to prepare NPMCs, with improved ORR activity demonstrated in acidic electrolytes. PANI was selected as it has previously been demonstrated to produce some of the most active NPMCs to date, due to its aromatic ring structure with a high content and uniform distribution of nitrogen species that can readily form nitrogen-doped graphitic carbon structures during heat treatment [55,58-60,93,107]. PAN is also helpful as a low-cost polymer carrier to overcome the poor solubility of PANI in solution and as a secondary source of nitrogen. We demonstrate that the addition of 10 wt. % PANI to the Fe-PAN electrospinning solution significantly enhances the ORR activity of the resulting NPMCs based on the onset potential and half-wave potential, while demonstrating high selectivity towards the 4-electron reduction of oxygen. This unique synthetic approach, therefore, provides reasonable progress towards the development of one-dimensional NPMCs for fuel cell applications.

4.2 Experimental

4.2.1 Fe–PANI Polymerization

In a 500 ml beaker, 5 mL of aniline and 50 mg of iron chloride ($FeCl_3$) were sequentially added to 300 mL of 1.0 M hydrochloric acid (HCl) under gentle stirring while keeping it below 10 ^oC using an ice bath. In another beaker, 11.4 g of ammonium persulfate (APS) was dissolved in 200 mL of 1.0 M HCl. This oxidant solution was then slowly added to the aniline mixture and stirring maintained for 24 h to allow complete polymerization. The liquid was removed using a rotary evaporator and the Fe–PANI complex was collected.

4.2.2 Synthesis of Fe-PANI-PAN Electrospun Nanofiber Catalysts

In a 25 ml vial, 1.0 g PAN (Mw 150,000), 100 mg of Fe–PANI and 315 mg of $FeCl_3$ were dispersed in 23 mL of dimethylformamide (DMF) by sonication for two days. Electrospinning was carried out using a needle–collector distance of 15 cm, solution flow rate of 200 µL h^{-1} and applied a voltage of 23 kV. The electrospun polymer nanofibers were then subjected to calcination at 250 ^oC for two hours in air using a heating rate of 1 ^oC min^{-1}. The materials were then annealed in argon at 850 ^oC for two hours to obtain the final Fe-PANI-PAN catalyst. As benchmarks, Fe-PAN and PANI-PAN samples were also prepared by similar methods without the incorporation of PANI and Fe precursors, respectively.

4.3 Results and Discussion

The first step of the present study was to optimize the formation of electrospun nanofibers by modifying the Fe-PANI-PAN concentrations within the DMF precursor solution. As shown in SEM images (Figure 4-1a and Figure 4-1b), when relatively low Fe-PANI-PAN concentrations of 1 and 2 wt. %, respectively are used, only blood–cell shaped droplets were observed, indicating that the surface tension at this solution concentration was likely too high [108]. By increasing the Fe-PANI-PAN concentration to 5 wt. %, nanofiber formation was clearly observed (Figure 4-1c). Diameters varying from ca. 30 to 150 nm (average of 100 nm) were found along with some bead structure. The presence of more beads highlights the impact PANI incorporation has on the electrospinning process in comparison to the smoother and relatively uniform electrospun Fe-PAN nanofibers shown in Figure 4-1e. It should be noted that higher Fe-PANI-PAN concentrations were not appropriate due to the poor solubility of PANI that limited its dispersion in the DMF solution.

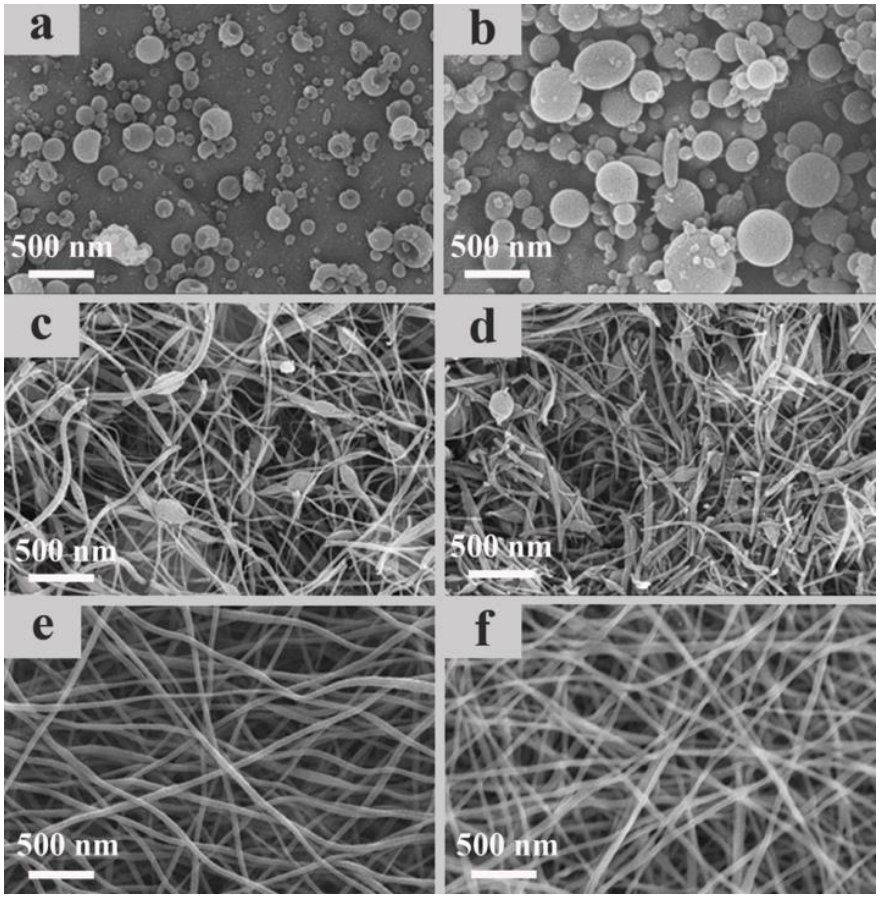

Figure 4-1 SEM images of Fe-PANI-PAN electrospun nanomaterials derived from **(a)** 1 wt. % **(b)** 2 wt. % and **(c)** Fe-PANI-PAN nanofiber derived from 5 wt. % polymer concentration in the DMF precursor solution and **(d)** Fe-PANI-PAN electrospun nanofibers derived from 5 wt.% after heat treatment. SEM images of Fe-PAN electrospun nanofibers **(e)** before and **(f)** after heat treatment.

The Fe-PANI-PAN nanofibers (Figure 4-1c) and Fe-PAN (Figure 4-1e) prepared from the 5 wt. % solution were then subjected to calcination in air at 250 ^{o}C and subsequent carbonization in argon at 850 ^{o}C (Figure 4-1d and Figure 4-1f, respectively). BET analysis

indicated a higher specific surface area of 355 $m^2 g^{-1}$ for Fe-PANI-PAN compared to 330 $m^2 g^{-1}$ for Fe-PAN. These values are significantly greater than those reported for non-porous carbon nanofibers [94,95] and similar to those of porous carbon nanofibers reported previously [94].

The effect of adding PANI was investigated by conducting XPS analysis of Fe-PAN-PANI and Fe-PAN nanofibers. The overall XPS spectra show the existence of carbon, oxygen, nitrogen, and iron in the catalysts. The high-resolution N 1s spectra provided in Figure 4-2 for Fe-PAN and Fe-PANI-PAN, respectively, revealed that the nitrogen content increased from 3.63 to 5.35 at. % with the addition of PANI (Figure 4-2). Based on peak deconvolution, it was found that pyridinic and graphitic/pyrrolic N were present in higher concentrations in Fe-PANI-PAN (pyridinic~2.50 and graphitic~2.45 at. %) compared to Fe-PAN (pyridinic~1.08 and graphitic~1.93 at. %). The increased content of these structures could likely arise during pyrolysis due to the unique aromatic structure of PANI which is linked via nitrogen sites in a vast chain (a rich source of nitrogen atoms) [93,107]. The increased nitrogen content of NPMCs has previously been associated with ORR activity both in alkaline and acidic environments [80,109-111], potentially underlying the beneficial impact of PANI incorporation towards the improved electrochemical performance highlighted later.

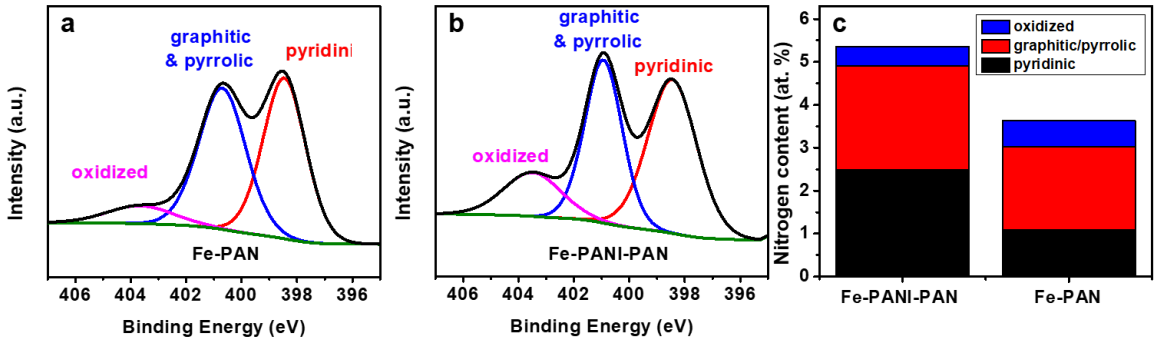

Figure 4-2 Nitrogen content and species of (a,c) Fe-PAN and (b,c) Fe-PANI-PAN.

Figure 4-3a shows CV plots of Fe-PANI-PAN in O_2 and N_2 saturated 0.1 M $HClO_4$. From this graph, ORR activity is observed due to the emergence of a distinct reduction peak that is not noted in the absence of oxygen [112]. Polarization curves of Fe-PANI-PAN are shown in Figure 4-3b along with the related Koutecky–Levich (K–L) plot (Figure 4-3c). The number of electrons transferred in RDE is calculated using the K–L equation (Equation 4-1) [113].

Equation 4-1

$$\frac{1}{i} = \frac{1}{i_k} + \frac{1}{m\sqrt{\omega}}$$

Equation 4-2

$$m = 0.201nFC_{O_2}D_{O_2}^{2/3}\nu^{-1/6}$$

Here, i_k is the kinetic current density, i is the experimental current density, m is the Levich slope (Equation 4-2) [113], and ω is the rotation speed. In Equation 4-3, n is the number

of electrons transferred, F is the Faraday constant, C is the dissolved oxygen concentration, D is the oxygen diffusion coefficient, and ν is the electrolyte kinematic viscosity [113]. The number of electrons transferred was calculated to be ca. 3.87 at all electrode potentials investigated, demonstrating high selectivity towards an overall 4-electron reduction mechanism occurring on the Fe-PANI-PAN catalysts. Ring currents from RRDE measurements were also used to determine the number of electrons transferred using Equation 4-3 [55]. At all potentials below ca. 0.65 V *vs*. RHE, the number of electrons transferred was calculated to be ca. 3.89 (Figure 4-3d), which is in good agreement with the results from K-L analysis. Accordingly, the peroxide yield (Equation 4-4) [59] for the Fe-PANI-PAN catalyst was also less than ca. 5.0 %, indicating high selectivity toward the 4-electron ORR to produce H_2O.

Equation 4-3

$$n = 4 \times \frac{I_D}{(I_R/N) + I_D}$$

Equation 4-4

$$H_2O_2\ (\%) = 200 \times \frac{I_R/N}{(I_R/N) + I_D}$$

Where N is the ring collection efficiency constant, and I_R and I_D are the ring and disk electrode current, respectively.

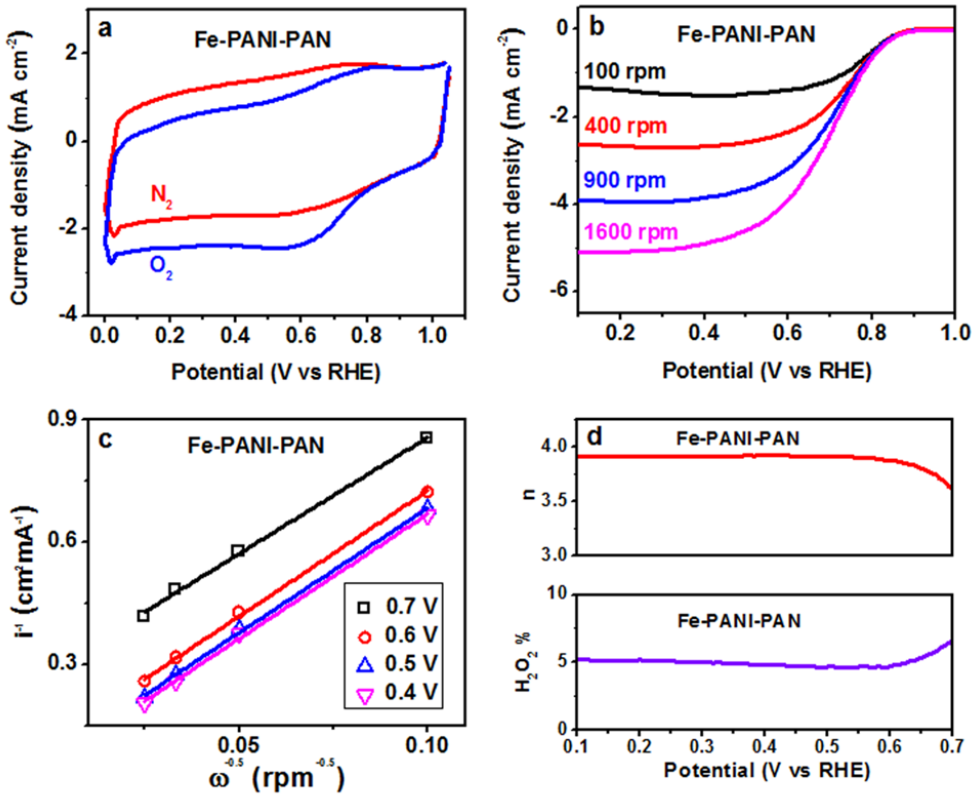

Figure 4-3 (a) CV curves of Fe-PANI-PAN in N_2 and O_2 saturated 0.1 M $HClO_4$, **(b)** Polarization curves performed in O_2 saturated 0.1 M $HClO_4$ of Fe-PANI-PAN at different rotational speed, and **(c)** the associated K–L plot. **(d)** The peroxide yield and n, the number of electrons transferred for Fe-PANI-PAN in O_2 saturated 0.1 M $HClO_4$. Catalyst loading of 0.6 mg cm^{-2}.

In Figure 4-4a, ORR polarization curves collected at 1600 rpm for catalysts derived from PAN-PANI, Fe-PAN, and Fe-PANI-PAN are demonstrated, with a comparison of the collected electrokinetic data summarized in Figure 4-4b. From these plots, it is seen that the addition of 10 wt. % PANI to Fe-PAN significantly improves the onset potential from 0.80 to

0.90 and the half–wave potential from 0.63 to 0.70 V *vs.* RHE. These results show greater than ca. 40 mV improvements in the onset and half–wave potentials in acidic media compared to the best results previously reported for NPMCs prepared by electrospinning and subsequent high-temperature heat treatment [104-106]. Coupled with the high selectivity towards the 4-electron reduction mechanism, Fe-PANI-PAN comprises the most active NPMCs prepared by electrospinning that has been reported to date. Although the exact origin of ORR activity in NPMCs is still unclear, the enhancements could potentially be linked to the relatively higher pyridinic and graphitic/pyrrolic nitrogen contents (Figure 4-2f) of Fe-PANI-PAN in comparison to Fe-PAN [59,60,110,112], along with the slightly higher surface area determined by BET analysis.

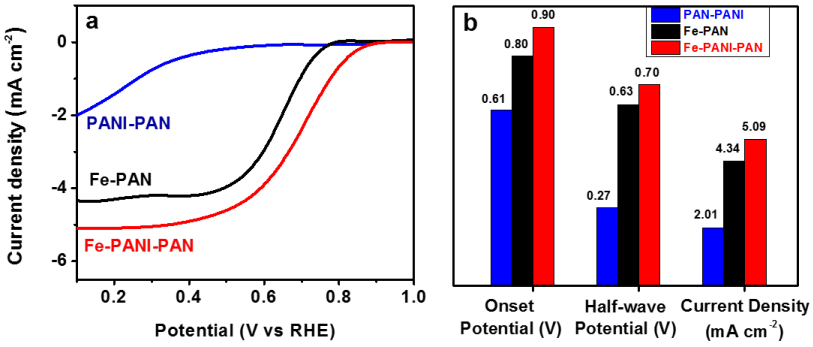

Figure 4-4 (a) Linear sweep voltammetry curves performed in O_2 saturated 0.1 M $HClO_4$ for Fe-PAN, Fe-PANI-PAN, and PANI-PAN at 1600 rpm, and **(b)** Corresponding comparison of onset potential, half–wave potential and limiting current density.

4.4 Conclusions

Fe–PANI-PAN nanofibers prepared via electrospinning and subsequent heat treatments were prepared as NPMCs. Electrochemical RDE and RRDE characterization revealed that the addition of 10 wt% PANI to PAN significantly improved the ORR activity of Fe-PANI-PAN in comparison to Fe-PAN. Based on XPS analysis, these enhancements can likely be attributed to the increased surface concentration of pyridinic and graphitic nitrogen species, probably arising due to the nitrogen, aromatic structure of PANI precursor. The preparation of Fe-PANI-PAN, therefore, provides a unique synthetic approach to preparing the most active one-dimensional NPMCs by electrospinning reported to date for the ORR.

Chapter 5

Co-N Decorated Hierarchically Porous Graphene Aerogel (Co-N-GA)

X. Fu, J-Y. Choi, **P. Zamani**, G. Jiang, Md. A. Hoque, F. M. Hassan, and Z. Chen, *ACS Applied Materials & Interfaces*, 8 (2016) 6488-6495

Part of the work described in this chapter has been published as reference [114] with permission from American Chemical Society.

5.1 Introduction

Owing to their high fuel efficiency and zero emissions at the point of operation, PEMFCs currently represent one of the most promising classes of energy conversion technologies [28]. For widespread commercialization of PEMFCs, one crucial factor is to reduce the high cost caused by the use of expensive platinum-based catalysts at the cathode due to the slow kinetics of the ORR [115-117]. Therefore, the search for efficient and less costly NPMCs for ORR is extremely important to commercialize clean operating, efficient electrochemical devices [39,57,118-120].

Recent research efforts towards replacing platinum-based catalysts have shown that nitrogen-doped carbon nanomaterials could act as effective ORR catalysts due to their low cost, excellent electrocatalytic activity, long durability and environmental friendliness [96,121-

[124]. Among them, graphene-based carbon materials have attracted significant interest as alternative ORR catalyst due to their exceptional chemical and physical properties such as ultra-high surface area, superior conductivity, and excellent mechanical/chemical stability [125-129]. However, most of the nitrogen-doped graphene materials which show promising ORR performance in alkaline electrolyte suffer from relatively low activity in acid medium, making them less competitive with commercial Pt/C catalyst. The introduction of transition metals (e.g. Fe, Co) to the above-mentioned graphene matrix results in M-N-C-based NPMCs which further enhances their ORR activity in acid media [36,130]. Although the nature of the catalytically active sites in these NPMCs remains elusive, quantum mechanical calculations and experimental investigations both indicate that M-N moieties, in which metal cations coordinated by pyridinic nitrogen atoms, play a vital role in catalyzing the ORR [56,131,132]. Also, according to a previous report, the limitations to enhancing the catalytic activity of these catalysts include the low density and utilization of M-N active sites and poor mass transport properties [133]. Thus, turning to large surface area and highly porous graphene structures to afford both abundant, accessible M-N catalytic sites and proper channels for mass transport is a potential solution to advanced ORR catalysts [12].

It is well known that graphene sheets tend to a drastic loss of steak together and lead specific surface area, which makes electro- active sites unacceptable for catalysis and inferior mass transfer. In order to improve the utilization of active sites and facilitate mass transfer through the entire volum of graphene-based catalysts, various strategies have been explored to prevent the stacking of individual graphene sheets. Spacer blocks such as carbon nanotubes, [134] metal nanoparticles, and templates have been inserted between graphene sheets to prevent

their stacking [135,136]. Different physical and chemical treatments have also been employed to yield porous frameworks that suppress their agglomeration [137-139]. However, the use of hazardous reagents or the tedious synthesis procedures results in low production yields and high costs. Besides, the electrochemical performances still need to be improved. Based on the above considerations, high ORR performance materials are expected for example by designing and constructing interesting graphene frameworks with large surface area and suitable porosity as well as more active M-N moieties. It will certainly be a great development if such a novel graphene structure could be fabricated through a simple but efficient way.

Here, we report a Co-N decorated graphene aerogel (Co-N-GA), which has unique hierarchical pores, large surface area and an abundance of potential Co-N active sites. A combined hydrothermal self-assembly, freeze-drying, and pyrolysis process was employed to efficiently prepare this porous graphene framework. Specifically, PANI is carefully selected as a pore-forming agent to aid in the self-assembly of graphene oxide (GO) species into a highly porous hydrogel structure, while also being an effective nitrogen precursor due to its unique chemical structure [58,59,140]. The as-fabricated graphene aerogel was used as a catalyst to achieve the following: 1) maximum Co-N active sites density; 2) optimum utilization of active sites; 3) facilitating of the proper transfer of reactant and product. Benefiting from these excellent structural properties, the Co-N-GA developed herein exhibits impressive electrochemical performance in acid medium.

5.2 Experimental Section

5.2.1 Synthesis of Co-N-GA

In a typical experiment, a 30 ml of an as prepared GO (2 mg ml^{-1}) aqueous solution containing $Co(NO_3)_2 \cdot 6H_2O$ (15 mg) and PANI (80 mg) was sonicated for 1 h to form a stable suspension. Subsequently, this suspension was sealed in a Teflon-lined autoclave and hydrothermally treated at 180 °C for 12 h. Afterward, a hydrogel was lyophilized to prevent the agglomeration of graphene sheets during the drying process. The uniform unified structure was then heated at 900 °C for 1 h under Ar. The heat-treated sample was then pre-leached in 2 M H_2SO_4 at 80 °C for 24 h to extract unstable and inactive metallic species from the materials and carefully washed with DI water. Finally, the catalyst was pyrolyzed over in Ar at 900 °C for 3 h referred to form what we denote as the "Co-N-GA" catalyst. For comparison, the Co-N modified graphene sheet catalyst (Co-N-GS) was prepared with a slightly modified approach. In the case of Co-N-GS, a 120 mL aqueous dispersion of diluted GO (0.5 mg ml^{-1}) with cobalt salt (15 mg) and PANI (80 mg) was prepared and then processed following the same synthetic procedure as above. Due to the relatively low concentration of GO solution, an amorphous precipitate instead of a hydrogel formed during the hydrothermal treatment. N-GA was also prepared with the same procedure as Co-N-GA but without the cobalt salt.

5.2.2 Electrochemical Measurements

RRDE testing was conducted to evaluate the ORR activity. 10 mg of catalyst and 3 mg of Nafion was dispersed in 1 mL of a 1-propanol ink then 12 μL of the ink was deposited on a

0.19635 cm^2 electrode. Electrochemical testing was conducted in 0.5 M sulfuric acid at ambient conditions by sweeping the electrode potential from 1.0 to 0.0 V (RHE) under oxygen saturation. Accelerated durability testing (ADT) was conducted by cycling the electrode potential 5000 times between 0.6 and 1.0 V vs. RHE under nitrogen saturation.

5.3 Results and Discussion

The fabrication process for Co-N-GA is illustrated in Figure 5-1. In the first step, a stable aqueous suspension containing GO, $Co(NO_3)_2 \cdot 6H_2O$ and PANI (Figure 5-2a) was hydrothermally treated to synthesize a graphene-based hybrid hydrogel (Figure 5-2b). Subsequently, a freeze drying and pyrolysis process were applied to obtain the aerogel with a unifrom architecture (Figure 5-2c). Finally, the as-prepared aerogel was pre-leached in 2 M H_2SO_4 to remove unstable and inactive species from the catalyst and then pyrolyzed again to yield the Co-N-GA. Here, PANI serves two essential functions in preparing the Co-N-GA catalyst. First of all, it helps with the assembly of graphene to form a hydrogel during the hydrothermal treatment, due to the hydrogen bonding and π-π interactions within GO which can prevent the restacking of GO and thereby form a hierarchical porous structure. Otherwise, a monolithic hydrogel could not be obtained in the absence of PANI. Second, it acts as an efficient nitrogen doping agent, due to its high N/C atomic ratio (0.17) and unique aromatic structure which can facilitate the incorporation of nitrogen-containing active sites into the graphene matrix [55]. Meanwhile, along with the decomposition of PANI during the pyrolysis

process, a significant amount of nitrogen-containing gas is released, which can further expand the graphene sheets to have fewer layers and increased porosity.

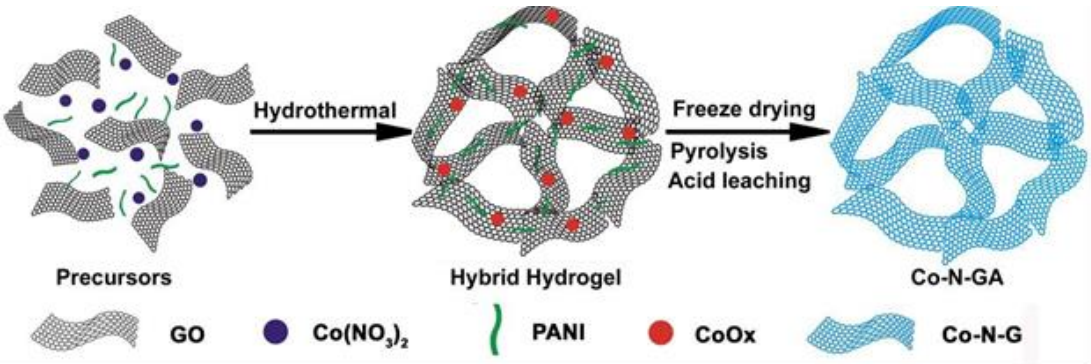

Figure 5-1 Schematic of the synthetic route for the Co-N-GA catalyst.

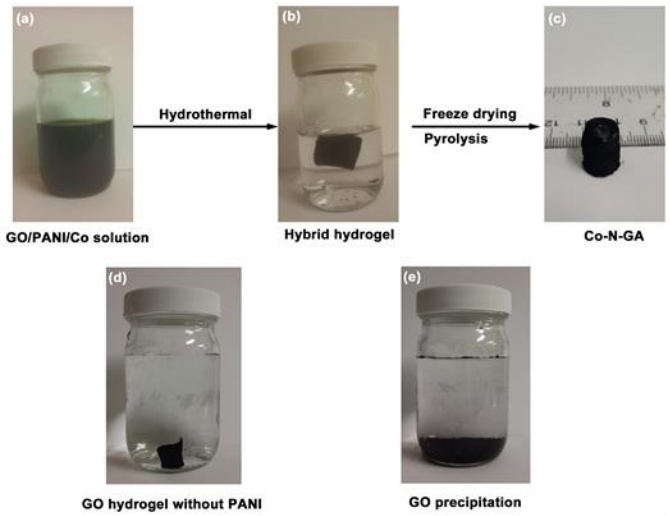

Figure 5-2 (a), (b) and **(c)** Fabrication process for the porous Co-N-GA catalyst; **(d)** GO hydrogel prepared in the absence of PANI and cobalt salt; **(e)** GO-based precipitation.

The morphology and microstructures of Co-N-GA were first investigated by SEM and TEM. SEM imaging reveals a significant amount of open-pore structures that continue through the graphene framework (Figure 5-3a). Meanwhile, the magnified SEM image indicates the existence of numerous smaller pores contiguous with large pores (Figure 5-3b). These SEM results confirm that Co-N-GA with an interconnected porous network that is beneficial for a catalsyt was successfully prepared. Such a porous graphene skeleton could maximize the exposure of active sites to participate in the ORR process. Meanwhile, during the ORR process, these robust interconnected pores could function as arteries that shorten the diffusion length of reactant and product [141]. In order to investigate the utilization of the pore structures, graphene-sheet-based Co-N-GS catalyst was also prepared. In contrast to Co-N-GA with loose porous networks, Co-N-GS exhibits a relatively agglomerated structure, which is disadvantageous for the contact of oxygen, electrolyte and active sites. TEM characterization of Co-N-GA reveals an almost transparent wrinkled surface characteristic of graphene, while some carbon composite structures which result from the carbonization of PANI and cobalt are also observed (Figure 5-3c). The high-resolution TEM (HRTEM) image of Co-N-GA further indicates the presence of graphitic carbon shells which are commonly observed in acid leached M-N-C catalysts (Figure 5-3d) [142,143]. The graphitic carbon shell structure is likely to improve the ORR performance due to the increased exposure of sites responsible for oxygen adsorption and fast electron transport as well as exhibiting more corrosion resistance [135].

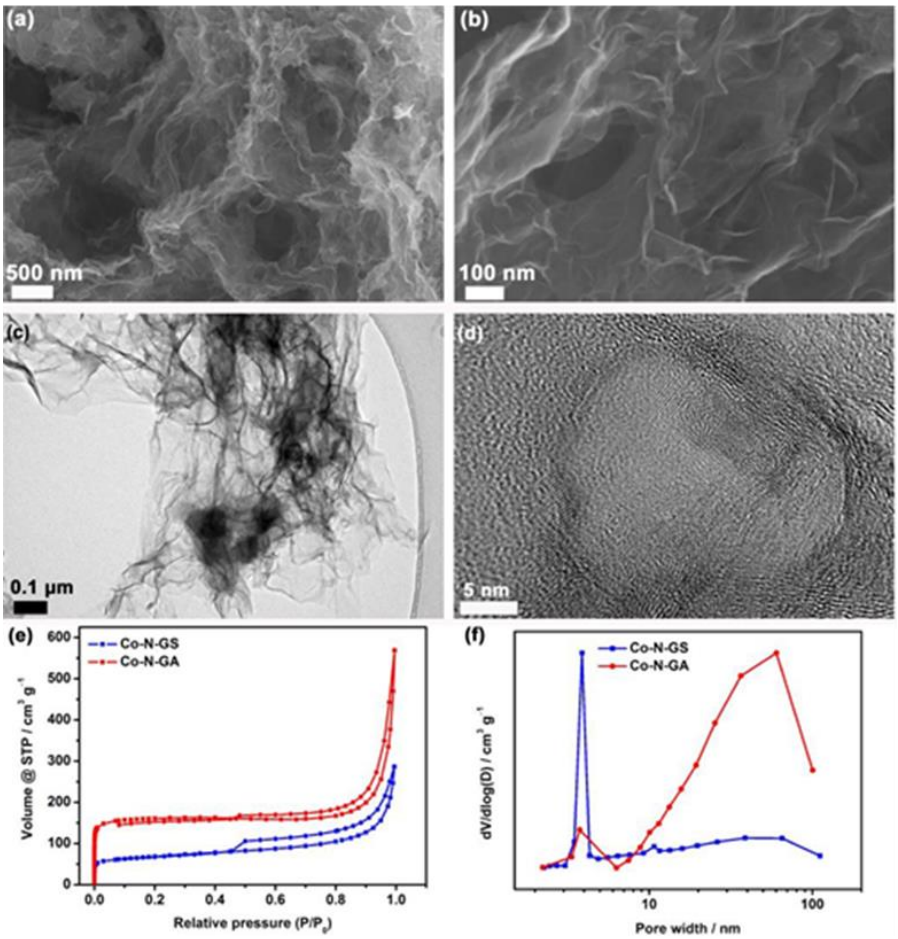

Figure 5-3 (a), (b) SEM and **(c), (d)** TEM images of as-obtained Co-N-GA. **(e)** N_2 sorption isotherms of Co-N-GS and Co-N-GA catalysts, and **(f)** the pore size distribution from the BJH method of corresponding samples.

The BET analysis of nitrogen adsorption−desorption isotherms (Figure 5-3e) reveals the absence of a plateau at high pressures indicating the presence of macropore. This conclusion is also supported by the rapid rise at low-pressure region. Meanwhile, the hysteresis in the middle-pressure range suggests the existence of a mesoporous structure that is likely formed by aggregates of lamellar graphene sheets. Remarkably, the specific surface area of

Co-N-GA is approximately 485 $m^2 g^{-1}$, which is about two times higher than that of Co-N-GS (222 $m^2 g^{-1}$). Such a high surface area graphene structure could have a high volumetric surface area and therefore, maximize the active site density to improve ORR performance. The pore size distribution (calculated by the B–J–H method) shows the presence of multiple porosities ranging from a few nanometers to the near micrometer scale (Figure 5-3f). It is worth noting that the Co-N-GA shows predominantly macro-pores compared to Co-N-GS which could shorten the diffusion length of reactive molecules and thus improve the ORR performance [144]. It is therefore expected that the presence of numerous large pores could provide superior electrochemical performance for Co-N-GA.

Raman spectroscopy and XRD were employed to characterize the physical structures of the graphene-based samples. As can be seen in Figure 5-4a, two peaks at ~1350 and 1580 cm^{-1} representing the well-defined D band and G band, respectively, were obtained. In comparison to GO, the increased I_D/I_G intensity ratio of N-GA, Co-N-GS, and Co-N-GA illustrates their greater disordered feature presumably caused by the nitrogen-doping. The XRD pattern in Figure 5-4b only shows a broadened peak at ~23°, corresponding to the (002) planes of carbon materials. No clear diffraction peak of only Co phases or its oxides is observed which shows that the majority of large inorganic cobalt particles were likely removed by the acid leaching step and any particles that may remain are too small or too low in concentration to be detected.

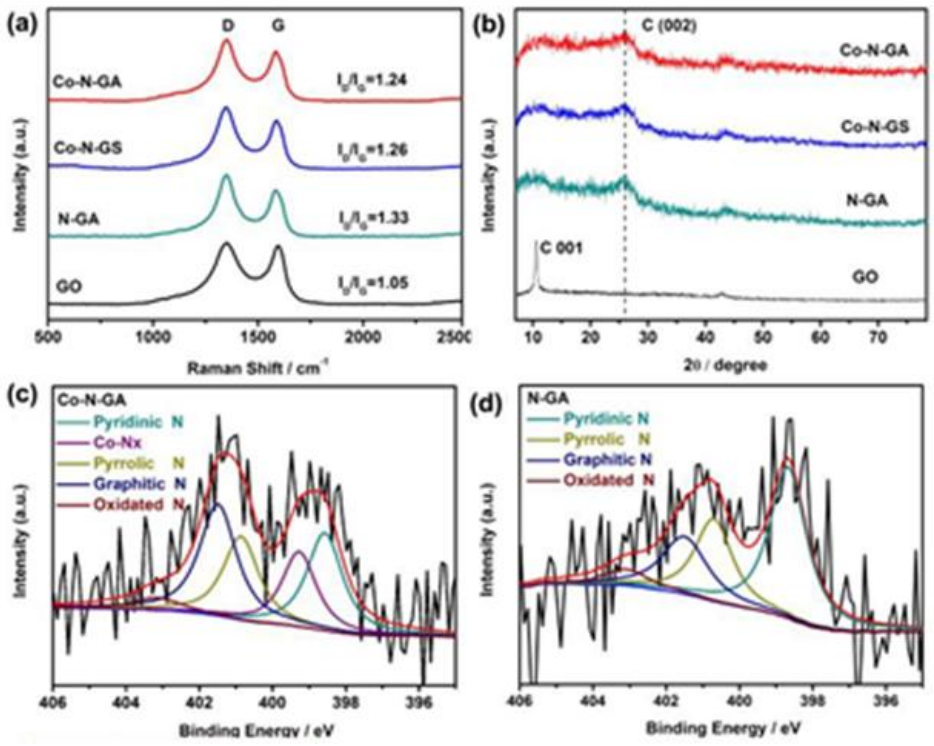

Figure 5-4 Raman spectra **(a)** and XRD patterns **(b)** of GO, N-GA, Co-N-GS, and Co-N-GA; **(c)** and **(d)** High-resolution N 1s peak of the resulting Co-N-GA and N-GA

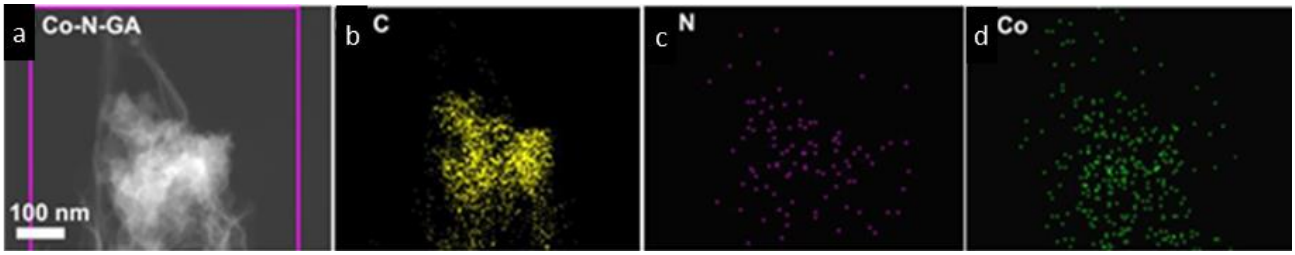

Figure 5-5 (a) STEM image of Co-N-GA and corresponding EDX elemental mapping images of **(b)** C, **(c)** N and **(d)** Co.

XPS measurements were further carried out to probe the chemical compositions and contents of the materials. The measured survey spectra of Co-N-GA and Co-N-GS reveal the

presence of C, O, N and Co peaks. Table 5-1 outlines the atomic surface concentrations with only small differences observed between the two catalysts. The high-resolution N 1s spectra of the two Co-N modified catalysts were deconvoluted into five different peaks with binding energies of 398.6, 399.3, 400.9 401.5 and 403.2 eV, corresponding to pyridinic N, Co-N, pyrrolic N, graphitic N and oxidized N, respectively [44,145]. The detailed peak-fitting results of the N 1s are listed in Table 5-2, and show different N-bonding configuration that likely exert a significant influence on their catalytic performances. In particular, the Co-N functionalities, which are proposed as the most likely active sites play an important role for the ORR activity in acidic medium.

Table 5-1 Elemental composition of the samples obtained from XPS results.

Samples	**C (at.%)**	**N (at.%)**	**O (at.%)**	**Co (at.%)**
N-GA	93.80	2.86	3.34	---
Co-N-GS	94.63	2.57	2.52	0.29
Co-N-GA	94.54	2.10	3.12	0.24

Table 5-2 Atomic concentrations (at.%) of heterocyclic N components of samples in the N 1s binding energy region (398 ~ 405 eV).

	Pyridinic N	**Co-N**	**Pyrrolic N**	**Graphitic N**	**Oxidized N**
	~398 eV	~399 eV	~400 eV	~401 eV	~402−404 eV
N-GA	43.75%	---	25.2%	24.5%	6.5%
Co-N-GS	26.3%	17.9%	18.9%	28.6%	8.2%
Co-N-GA	25.8%	18.7%	21.4%	29.8%	4.2%

EDX analysis was also employed to probe the elements and their locations in Co-N-GA further. First, the EDX maps in Figure 5-5 confirm the presence of elemental C, N, O, and Co in Co-N-GA, in agreement with the XPS results. EDX elemental mapping was performed to further identify the distribution of elements in this catalyst. Unexpectedly, Co species were detected along with C, N and O elements to be uniformly distributed throughout the graphene structure (Figure 5-5a-d). Such finely dispersed Co species could coordinate with the N atoms to form Co-N moieties which are believed to be highly active for ORR. All in all, the well distributed Co-N sites and the porous structure are highly beneficial for the ORR performance.

The catalytic performance of the prepared materials towards the ORR was evaluated in 0.5 M oxygen saturated H_2SO_4 solutions by the RRDE method. For comparison, pure N-GA, Co-N-GS and commercial Pt/C (TKK, 28.2 wt.% Pt) were also investigated. As shown in Figure 5-6a, Co-N modified graphene materials (Co-N-GA and Co-N-GS) exhibit more

positive onset potential (E_o) and half-wave potential ($E_{1/2}$) than that of N-GA. This higher half-cell activity indicates the ability of Co-N moiety modified graphene materials to catalyze the ORR in acid medium efficiently. This result agrees with that of a previous report that a transition metal is necessary for nitrogen-doped carbons to be highly active catalysts, due to the formation of Co-N coordination structures [12]. Moreover, the E_o and $E_{1/2}$ of Co-N-GA (E_o = 0.88 V, $E_{1/2}$ = 0.73 V) are more positive than that of Co-N-GS (E_o = 0.84 V, $E_{1/2}$ = 0.68 V), which is approaching the commercial Pt/C catalyst (E_o= 1.0 V, $E_{1/2}$ = 0.86 V). Additionally, Co-N-GA also shows a slightly higher diffusion limiting current density than that of Co-N-GS at 0.3 V (Figure 5-6a).

The peroxide yield and electron transfer number (n) of the prepared catalysts and Pt/C were further studied using the RRDE analysis. The measured H_2O_2 yield on the Co-N-GA electrodes is 7%−13% from 0.2 V−0.7V, which is slightly superior to that of Co-N-GS (10%−15%, Figure 5-6b). On the basis of the ring and disk currents, the n values for Co-N-GA were 3.75−3.85 over the potential range from 0.20−0.70 V, similar to that of Co-N-GS (3.71−3.80, Figure 5-6b), approaching that of Pt/C catalysts, indicating that both of the two Co-N modified samples proceed mainly via a 4-electron mechanism. Given the above analysis, the enhanced ORR activity of Co-N-GA could mainly originate from its unique hierarchically porous structure and more active Co-N moieties. On the one hand, the abundant hierarchical pores could sharply enhance the surface area of the catalyst, which could provide sufficient active sites to participate in the ORR process. Meanwhile, the hierarchical pores are favorable for mass transport and electrolyte accessibility. On the other hand, the potential Co-N moieties

could function as more active sites for the catalyst, which could further improve the ORR performance. All of these merits could contribute to the final excellent ORR performance.

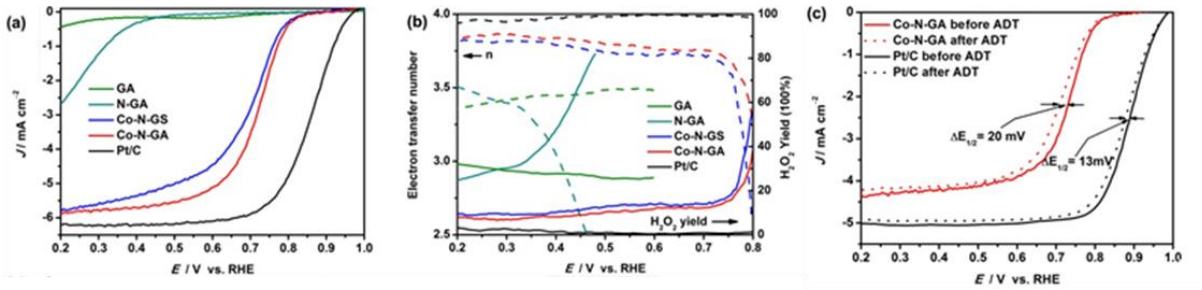

Figure 5-6 (a) RRDE polarization curves of the GA, N-GA, Co-N-GS, Co-N-GA and Pt/C in 0.5 M H_2SO_4 at a scan rate of 10 mV s^{-1} and 1600 rpm; **(b)** electron-transfer number and H_2O_2 yield of the catalysts; **(c)** ORR polarization plots of Co-N-GA and Pt/C before and after 5000 potential cycles in N_2 saturated 0.5 M H_2SO_4 at a scan rate of 10 mV s^{-1} and 1600 rpm. The potential was cycled between 0.6 and 1.0 V at a rate of 50 mV s^{-1}.

Apart from the ORR activity, stability is another important aspect of fuel cell catalysts to be considered. The durability of the Co-N-GA catalyst was assessed using an ADT by potential cycling between 0.6−1.0 V at 50 mV s^{-1} under N_2 saturated solution. After 5000 continuous cycles, a small negative shift of $E_{1/2}$ (ca. 21 mV) was exhibited by Co-N-GA, which is similar to the ca. 15 mV negative shift observed in Pt/C (Figure 5-6c). This relatively good stability, suggests comparable durability of Co-N-GA in an acidic electrolyte, a feature rarely seen for NPMCs. The high electrochemical stability of this Co-N-GA catalyst could be ascribed to the high degree of graphitization of the carbon support and the lower H_2O_2 production [60,63].

5.4 Conclusion

In summary, a Co-N decorated graphene aerogel has been successfully fabricated via a simple approach. The introduction of PANI, which acts as a hydrogel-forming agent and a nitrogen precursor, can efficiently prevent the re-stacking of the graphene sheets and promote nitrogen doping. The resulting Co-N-GA framework possesses a high BET surface area and hierarchically porous skeleton as well as the homogeneous distribution of potential Co-N active sites, which can not only expose the more active sites to the electrochemical interface but also facilitate mass transport to improve the ORR performance. Based on these characteristics, the resultant Co-N-GA exhibits high ORR activity ($E_{1/2}$ = 0.73 V), high electron transfer selectivity (n >3.75), and excellent electrochemical durability in acidic solution. The outstanding electrochemical performance makes the Co-N-GA a promising NPMC for PEMFC.

Chapter 6

Highly active and porous graphene encapsulating carbon nanotubes (Fe-PANI-CNT)

P. Zamani, D. C. Higgins, F. M. Hassan, X. Fu, J-Y. Choi, Md A. Hoque, G. Jiang, Z. Chen, *Nano Energy* 26 (2016) 267-275

Part of the work described in this chapter has been published as reference [146], with permission from Elsevier.

6.1 Introduction

PEMFCs are highly promising clean energy devices and considered as ideal alternatives to the conventional fossil fuel based technologies used in the automotive industry, telecommunications backup and materials handling [98,147,148]. Although target markets exist, technical challenges relating to cost and durability must be addressed [4]. The major bottle-necks arise at the cathode where the ORR occurs [1,9-12,93]. Currently, the only technologically viable ORR catalysts are platinum-based. The high price of Pt-based catalysts is the reason why developing new catalyst materials with high performance, at lower costs is of keen interest.

NPMCs are attractive classes of materials to replace the platinum in conventional ORR catalysts. They are actively under development [2,11,12] and prepared via several synthetic approaches such as MOF application [70,149-151], sacrificial support method [71-74], hydrothermal or

solvothermal synthesis [114,152], pyrolyzing carbon supported complexes [58,153-156], and polymerization of nitrogen containing monomers [55,57,58,76,157]. These approaches, using high-temperature pyrolysis in the presence of iron and/or cobalt precursors, have yielded M-N-C complexes which are so far the most promising class of NPMCs.

In the present study, we apply and optimize an ammonia treatment to tune the chemistry of a catalyst derived from iron, PANI, and CNT. This approach results in improved performance, under both half-cell and fuel cell conditions. NH_3 contributes by enriching the N-dopant concentration. By controlling the temperature, we can tailor the particular identity of the nitrogen dopants to maximize catalytic activity. The overall synthesis process ultimately leads to in-situ graphitization of carbon and a catalyst structure that consists of multilayer highly porous graphene morphologies encapsulating CNTs with an abundance of nitrogen and iron defects. This surface chemistry renders the catalyst highly active towards the ORR, coupled with the robustness of the graphene-like morphology.

6.2 Materials and Methods

6.2.1 Functionalized Multiwalled Carbon Nanotubes

Commercial carbon nanotubes with 30-50 nm diameters and 10-20 μm lengths were functionalized first by immersing 10.0 g in 400 ml of 70% nitric acid. The mixture was then refluxed at 85 ^{o}C for 8 hours while being vigorously stirred. Functionalized CNTs were then filtered and washed with DDI water and dried in an oven overnight.

6.2.2 $FeCl_3$-PANI-FCNT polymerization

3 ml aniline and 10 g $FeCl_3$ were added into 300 ml HCl at room temperature and continuously stirring throughout the entire process. Slowly, 5.0 g of $(NH_4)_2 S_2O_8$ (ammonium peroxidisulfate, APS) was added as an oxidant to polymerize the aniline in the above solution. The mixture was vigorously stirred at room temperature for 3 hours to allow full polymerization of the aniline fully. After 3 hours, a suspension of 400 mg CNTs in DDI water was slowly pipetted into the PANI mixture. The solution was then vigorously stirred for 48 hours. After this, the liquid was evaporated and the solid polymer ($FeCl_3$-PANI-CNT) was collected.

6.2.3 Catalyst synthesis

The catalyst precursors were first heat treated at 200 ^oC for 1 hour under 70 ml min^{-1} of argon (Ar) and a 30 ^oC min^{-1} heating rate. The subsequent heat treatment for the resulting powder was done at 900 ^oC for 1 hour using the same heating rate and Ar flow rate. The solid samples were then leached in 0.5 M sulfuric acid at 80-90 ^oC for 8 hours to remove the inactive iron complexes as well as to introduce a porous morphology. As can be seen from the nomenclature outlined in Table 6-1, after this leaching process, some catalysts were heat-treated in one step in ammonia at temperatures ranging from 900-1000°C. Others were pyrolyzed at 900 ^oC in Ar for 3 hours (Fe-P-C_Ar) to improve the ORR activity further and to remove surface functional groups. This step is referred to as the conventional second heat

treatment. After this step, ammonia treatment was done at temperature ranges from 800-1050 ^{o}C for 15 minutes and under a 300 mL min^{-1} ammonia flow rate. These samples are designated Fe-P-C_Ar-NHxxx in which the "xxx" is replaced with the NH_3 temperature (Table 6-1). A schematic of the catalyst synthesis is displayed in Figure 6-1.

Table 6-1 Sample nomenclature

Name	**Sample preparation (after acid leaching and filtration)**
Fe-P-C_Ar	Heat treatment in Ar for 3 hours at 900 ^{o}C (i.e., conventional second heat treatment)
Fe-P-C_Ar-NH800	Conventional second heat treatment and then NH_3 treatment at 800 ^{o}C for 15 minutes
Fe-P-C_Ar-NH900	Conventional second heat treatment and then NH_3 treatment at 900 ^{o}C for 15 minutes
Fe-P-C_Ar-NH950	Conventional second heat treatment and then NH_3 treatment at 950 ^{o}C for 15 minutes
Fe-P-C_Ar-NH1000	Conventional second heat treatment and then NH_3 treatment at 1000 ^{o}C for 15 minutes
Fe-P-C_Ar-NH1050	Conventional second heat treatment and then NH_3 treatment at 1050 ^{o}C for 15 minutes
Fe-P-C_NH900	NH_3 treatment at 900 ^{o}C for 15 minutes
Fe-P-C_ NH1000	NH_3 treatment at 1000 ^{o}C for 15 minutes

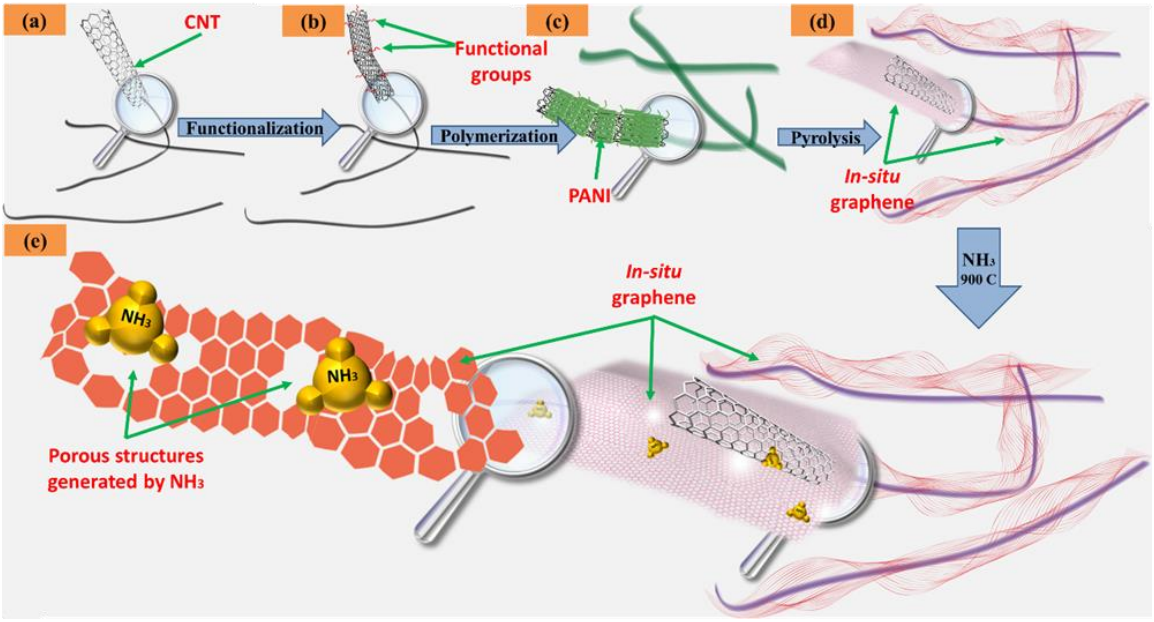

Figure 6-1 Schematic of the catalyst synthesis procedure, **(a)** starting with CNT **(b)** after functionalization, **(c)** polymerized $FeCl_3$-PANI-CNT composite, **(d)** pyrolyzed Fe-P-C_Ar, and **(e)** NH_3-treated Fe-P-C_Ar-NH900.

6.2.4 Electrochemical characterizations

Half-cell RDE testing, a well-established method to evaluate the electrochemical performance of catalyst materials, was used to analyze the ORR taking place on the catalyst materials. More positive onset and half-wave potentials and increased current densities reflect higher activity toward the ORR. In order to simulate the acidic circumstances encountered during PEMFC operation at the cathode, a 0.5 M H_2SO_4 solution was used as the electrolyte and saturated with oxygen during ORR testing. The working electrode was a Pine glassy carbon disc (0.19635 cm^2) coated uniformly by the catalyst ink to achieve a loading of 0.6 mg

cm^{-2}. A graphite and Ag/AgCl electrode were utilized as the counter and reference electrodes, respectively. All potentials are converted to the RHE scale for the ease of analysis. In order to activate the catalyst, a CV was obtained in an oxygen saturated electrolyte at a scan rate of 50 mV s^{-1}. During ORR testing, the potential of the working electrode in an oxygen-saturated electrolyte was scanned from ca. 1.0 to 0.0 V *vs*. RHE using linear staircase voltammetry (LSCV) with a 30 mV amplitude and 30 s periods. For the half-cell durability test, the potential of the working electrode was cycled between 1.0 and 0.2 V *vs*. RHE at 50 mV s^{-1} in the N_2 saturated electrolyte. After different cycle numbers, ORR evaluation was performed with the conditions mentioned above. RRDE testing was also used to analyze the behavior of the catalysts with respect to the 4-electron reduction of oxygen to H_2O. The ring potential was held at 1.2 V *vs*. RHE to reduce any peroxide species reaching the ring electrode surface.

For performance under PEMFC operating conditions, the catalyst was applied to the fuel cell cathode and a commercial Pt-cloth gas diffusion layer (0.5 mg cm^{-2} Pt) served the anode. Cathode ink was prepared using a mixture of 40 mg catalyst, 480 mg isopropanol, 480 mg DDI water, and 440 mg commercial Nafion solution (5 wt.%). In this way, the overall Nafion content in the dry catalyst ink was held at 35 wt%. A dry Nafion 211 membrane (previously immersed in 0.5 M boiling sulfuric acid for 1 hour and then in boiling DDI water for 1 hour) was placed on the vacuum table. After sonication for 1 hour, the ink was painted on the center of the membrane (5.0 cm^2 area) to reach a cathode catalyst loading of 4.0 mg cm^{-2}. The MEA was prepared as follows: the catalyst-coated membrane (CCM) was placed on top of the anode, and a commercial GDL (SGL BC 25) on top of the painted catalyst. The entire assembly was then hot-pressed together at 120 ^oC for 4 minutes using a force of 600 pounds.

Fuel cell testing was carried out by flowing hydrogen to the anode at 200 standard cubic centimeters per minutes (sccm) and by flowing air or oxygen to the cathode at 200 sccm. The cell temperature was held at 80 ^{o}C and the back pressure was set at 20 psig for both the anode and cathode side. Once the appropriate potential was reached, it was changed in increment of 0.03 V point^{-1} and held for 20 sec at each point.

6.3 Results and Discussion

The initial objective of the current research was to study the effects of the ammonia treatment temperature and heat treatment protocol. In order to optimize the heat treatment conditions after acid leaching, some catalysts were first pyrolyzed in Ar at 900 ^{o}C for 3 hours and then heat treated in ammonia at different temperatures. As benchmarks, some samples were heat treated in only ammonia at varying temperatures after acid leaching. Sample nomenclature in Table 6-1 indicates sample heating environment and temperature. SEM images (Figure 6-2a-c) show the morphology of the CNTs used as carbon supports and the resulting catalysts (before and after ammonia treatment at 900 ^{o}C for 15 min). As it can be seen from the SEM images (Figure 6-2b,c), after NH3 treatment a significant amount of porous structures are formed. A comparison of the TEM image of Fe-P-C_Ar (Figure 6-2d) with that of Fe-P-C_Ar-NH900 (Figure 6-2e) also supports the conclusion that the ammonia treatment increases the porosity. Both of the Fe-P-C_Ar-NH900 and Fe-P-C_Ar catalysts exhibit very high specific surface areas (higher for Fe-P-C_Ar-NH900) of ca. 1100 m^2 g^{-1} and 1050 m^2 g^{-1}, respectively (Figure 6-2g). Such large surface areas are attractive from a mass transport

perspective and can facilitate reactant access to catalytically active ORR sites and thereby improve electrode utilization and performance [144]. The TEM images (Figure 6-2d-f) also shows the formation of graphene-like structures (red arrows) after pyrolysis. The *in-situ* formation of graphene structures by using PANI is likely due to the similarity between graphene and the aromatic structures of PANI [55,57]. The HRTEM image of Fe-P-C_Ar-NH900 indicates that the graphitic structures remained after ammonia treatment (Figure 6-2f).

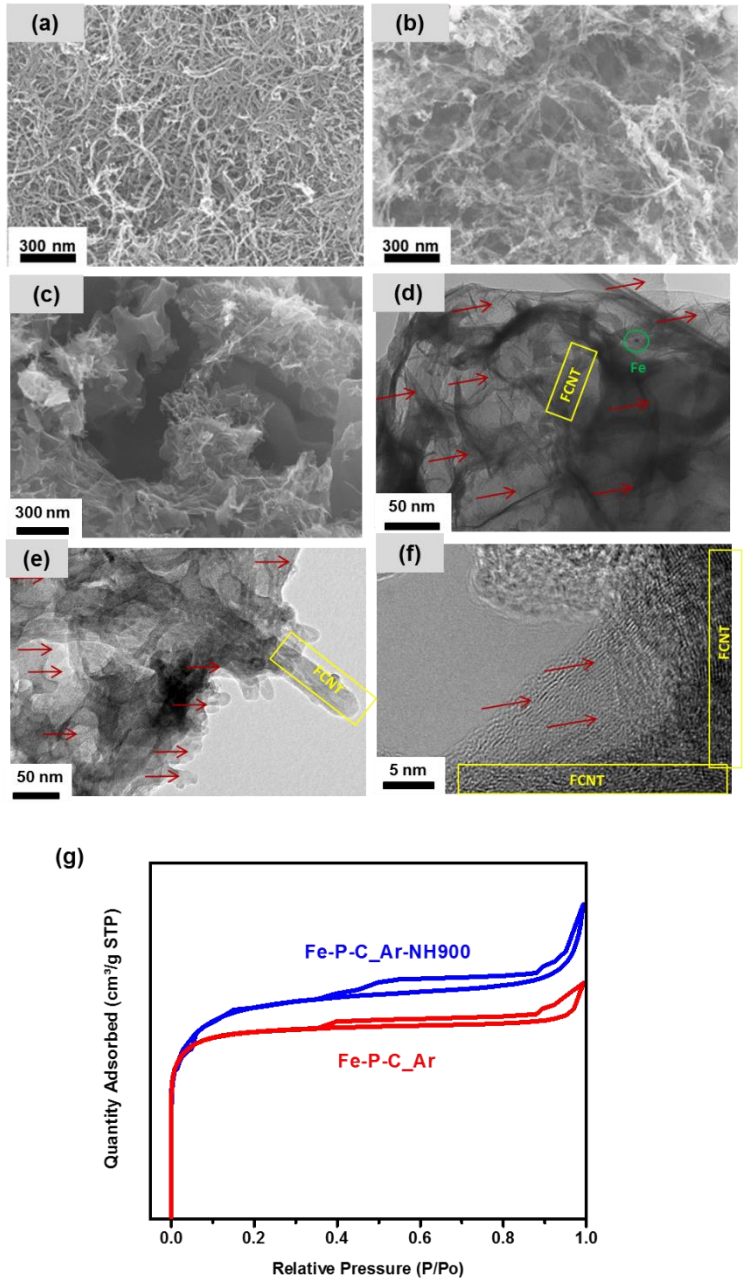

Figure 6-2 SEM images of **(a)** CNT **(b)** Fe-P-C_Ar and **(c)** Fe-P-C_Ar-NH900. **(d)** TEM image of Fe-P-C_Ar. **(e)** and **(f)** HRTEM images of Fe-P-C_Ar-NH900 at different magnifications. **(g)** N_2 sorption analysis of Fe-P-C_Ar and Fe-P-C_Ar-NH900.

XPS C1s spectra of the catalysts (Figure 6-3a) shows higher amounts of sp2 bonded carbon (284.85 eV) [158] and a lower amount of oxidized carbon species (286.35 eV) [159,160] for the NH_3-treated samples in comparison to Fe-P-C_Ar. For instance, the Fe-P-C_Ar-NH900 has 56.20 at% sp^2 carbon and 11.69 at% oxidized carbon, compared to 52.02 at% sp^2 carbon and 12.35 at% oxidized carbon for Fe-P-C_Ar which indicates a higher degree of graphitization and reduced amount of defect structures for the NH_3-treated sample. The larger amount of graphitic carbon could be due to an additional high-temperature pyrolysis step (under NH_3 atmosphere) in the presence of iron species. However, the amount of sp^2 C=C decreases with increasing the NH_3 temperature from 58.36 At% for Fe-P-C_Ar-NH800 down to 53.53 At% of sp^2 carbon for Fe-P-C_Ar-NH1000. This finding suggests that the reaction between NH_3 and graphitic carbon is facilitated at higher ammonia treatment temperatures, most likely due to the abundance of thermal energy to surpass the activation energy of the reaction. XPS N1s spectra of the catalysts derived from different NH_3 heat treatment are also provided, in addition to the corresponding nitrogen content column plots in Figure 6-3b and d, respectively. It can be seen that while the ammonia temperature has no significant effect on the pyrrolic N species quantity (400.2 eV), it does affect the amount of pyridinic (398.6 eV) and graphitic/quaternary nitrogen contents (401.5 eV) [161].

From the XPS results, an increase of the NH_3 temperature from 800-1000 ^oC results in a higher graphitic/quaternary nitrogen atomic percentage (Figure 6-3c). The pyridinic N quantity, however, increases with temperature up to maximum at 900 ^oC (0.96 At%) and then decreases at higher temperatures. From the XPS data comaprison with the sample not treated with ammonia, it appears that the NH_3 treatment results in an increase in nitrogen content,

accompanied by an increase in the relative concentration of pyridinic and graphitic nitrogen. While for Fe-P-C_Ar the amount of pyridinic and graphitic N were respectively 0.55 and 0.67 At%, they are correspondingly as high as 0.6-0.96 and 1.08-1.71 after ammonia treatment and doping. This trend is consistent with previous reports [68,72]. However, as these M-N-C systems are highly heterogeneous in nature, active site elucidation is very difficult and only recently have sophisticated *in-situ* synchrotron and Mossbauer techniques started to shed light on this important topic [68,162,163]. With regards to the active site density on these catalysts, the NH_3 treatment etches some of the disordered carbon that can allow for exposure of buried ORR active sites. Additionally, the increased surface area and mesopore content could mean that the number of active sites accessible to oxygen is significantly increased.

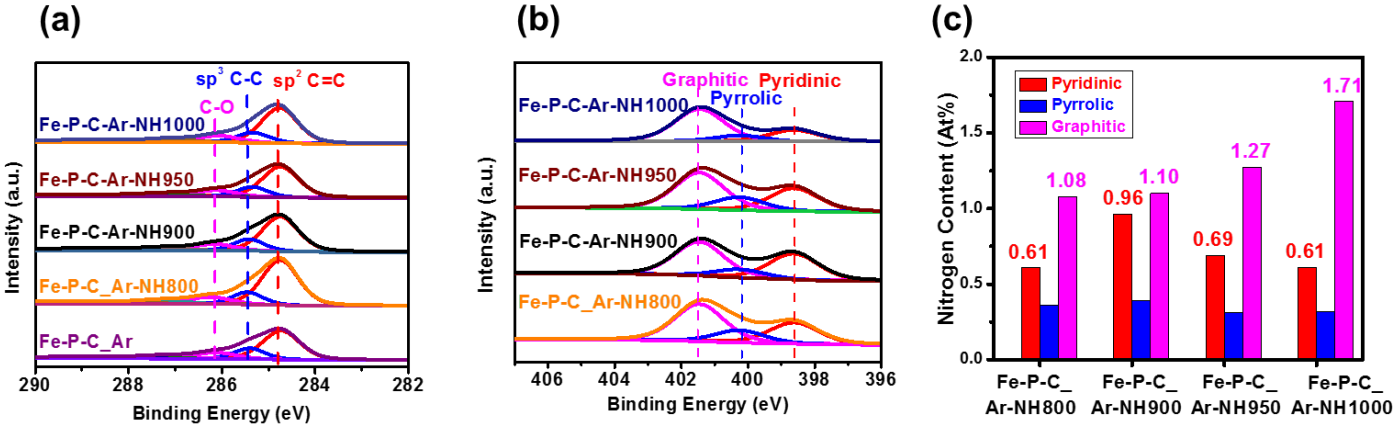

Figure 6-3 (a) C 1s, **(b)** N 1s spectra and **(c)** the corresponding nitrogen content and species distribution of Fe-P-C_Ar-NHxxx catalysts derived at different NH_3 temperatures from 800 to 1000 ^oC.

The STEM image shown in Figure 6-4a and the corresponding EELS images presented in Figure 6-4b-d outline the elemental distribution in the selected area of the catalyst. Considering that each pixel of the picture represents an area of 4.0 nm × 4.0 nm, these images confirm that the iron, nitrogen, and carbon species are very well dispersed throughout the CNT and *in-situ* formed graphene structures. The uniform distribution can mainly be seen when looking at the superimposed images of Fe-N-C (Figure 6-4e) and Fe-N elements (Figure 6-4f). Such well-dispersed Fe species suggest that they can potentially coordinate with the nitrogen atoms to form Fe-N and Fe-N-C moieties, which are believed to be highly active for ORR [93,164]. However, sophisticated methods, including *in-situ* XAS or Mossbauer spectroscopy are needed to confirm these structures. The highly mesoporous morphology formed after NH_3 treatment, as well as extremely high surface area and the well dispersed Fe-N-C distribution, are believed to be highly beneficial for the ORR performance [93].

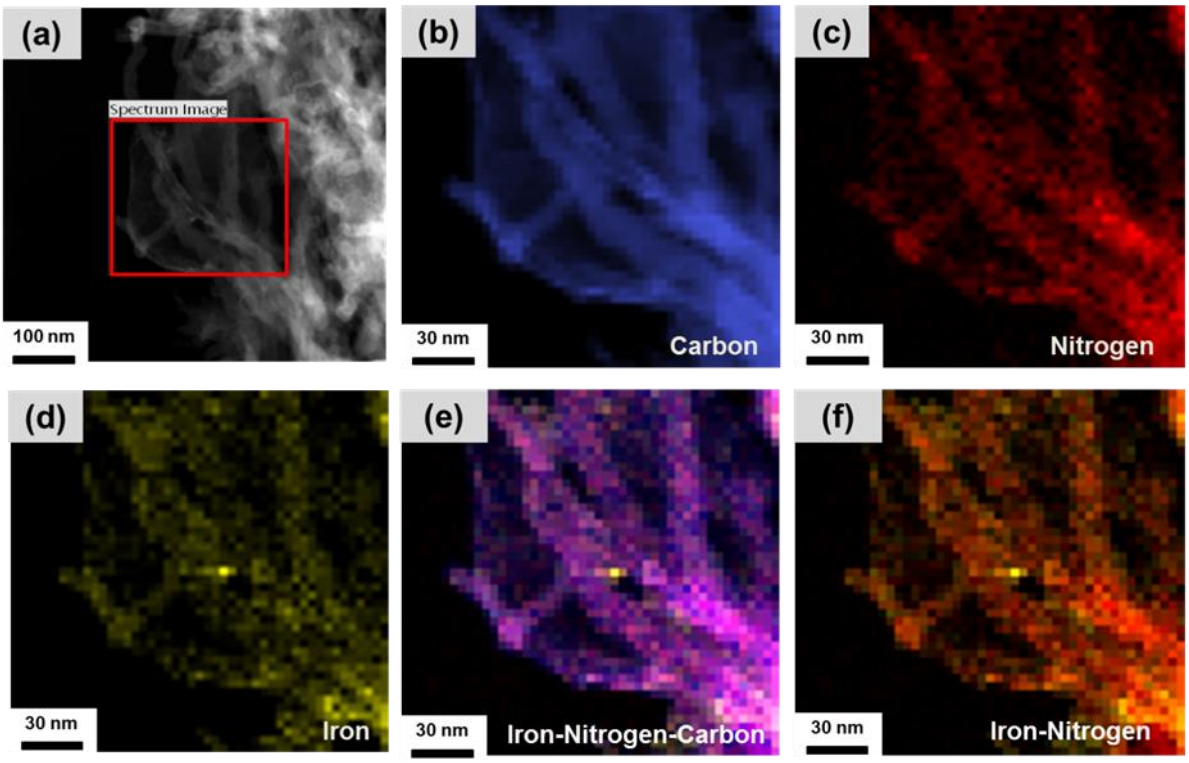

Figure 6-4 (a) STEM image of Fe-P-C_Ar-NH900 and the corresponding EELS elemental mapping images for the selected spectrum area of **(b)** C, **(c)** N, **(d)** Fe, **(e)** superimposed Fe-N-C (light green, red, blue), and **(f)** superimposed Fe-N (light green, red) with each pixel represents an area of 4.0 nm × 4.0 nm.

From the ORR polarization curves collected at 900 rpm (Figure 6-5a,b), NH_3 treatment improves the current densities, onset and half-wave ($E_{1/2}$) potentials significantly. NH_3 treatment induces the formation of some type of heteroatom doping that is beneficial for ORR, by tuning the active sites via generating local heterogeneity in electron density. Moreover, the higher porosity of the NH_3-treated catalyst could facilitate mass transport of oxygen into the catalyst layer and the removal of water molecules to the electrolyte. The effect of heat treatment

on ORR performance is shown in Figure 6-5a. Samples which undergo a pyrolysis in Ar before NH_3 treatment show better performance compared to those that are directly heat-treated in ammonia. The key to the activity gains following this second pyrolysis arises mainly due to the acid leaching step. Any inactive inorganic metal species are removed through this procedure and so increase the porosity and surface exposure of the catalyst. This second heat treatment likely removes any residues remaining following the acid leaching process and enhances the degree of graphitization. In Figure 6-5b it can be seen that the catalyst generated by using an NH_3 temperature of 900 ^oC shows the best ORR performance ($E_{1/2}$ of 0.80 V vs. RHE) compared to those synthesized at higher ammonia temperatures. The obtained half-wave potential places this catalyst on par with some of the most active NPMCs reported to date [70,72]. With respect to the XPS results in Figure 6-3c,d, the activity trends show that the pyridinic N content potentially makes an important contribution to the ORR activity since the sample with the highest pyridinic N content (Fe-P-C_Ar-NH900 with pyridinic N content of 0.96 At%) and relatively high amount of graphitic nitrogen exhibits the best ORR activity.

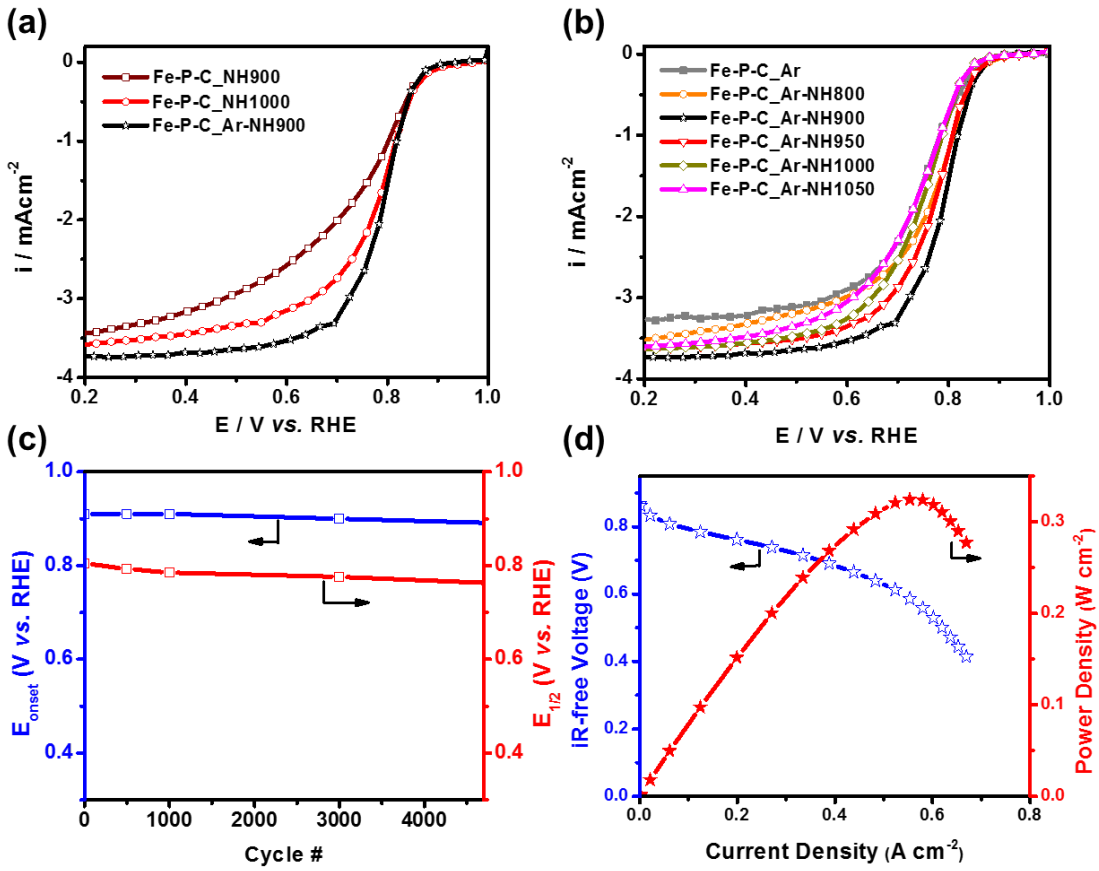

Figure 6-5 ORR activity results for **(a)** catalysts derived from different synthesis protocols and **(b)** Fe-P-C_Ar-NHxxx catalysts derived at different ammonia treatment temperatures. **(c)** Durability results for Fe-P-C_Ar-NH900. All the polarization curves are performed in O_2 saturated 0.5 M sulfuric acid at 900 rpm rotational speed. **(d)** Fuel cell testing for Fe-P-C_Ar-NH900 under H_2-air anode-cathode feeds. Fuel cell tests used 0.5 mg cm^{-2} Pt at the anode.

The reaction between NH_3 and carbon-based materials includes the exchange of O_2-containing groups with nitrogen-based species, as well as etching of carbon by radicals formed during ammonia decomposition at high temperatures and therefore it is related to the NH_3

treatment temperature [165]. When the ammonia temperature is above 900 ˚C, the breakdown of the porous structures that were generated during overall previous pyrolysis steps could happen. A similar phenomenon was observed previously by another group, in which they showed that by increasing the NH_3 temperature, the average mesoporous size decreased, pointing out the breaking down of the porous morphology [166]. Moreover, from the C 1s XPS results in Figure 6-3b, it was observed that with increasing the NH_3 temperature, higher amounts of sp^2 graphitic carbon species undergo breakdown. The collapse of graphitic carbon structures and the likeliness of porous morphologies decomposition could likely be the reasons for the lower ORR activity at ammonia treatment temperatures above 900 ˚C.

RRDE measurements were also performed to investigate the 4-electron selectivity of catalysts based on Equation 4-3 and Equation 4-4. From RRDE results for Fe-P-C_Ar-NH900 and Fe-P-C_Ar (Figure 6-6a,b), the number of electrons transferred per reduced oxygen molecule is measured to be 3.90 ± 0.05 at relatively high potentials (0.4-0.8 V *vs*. RHE), thereby showing a very good selectivity towards the 4-electron reaction. On the other hand, while the peroxide yields for Fe-P-C_Ar in that high potential range can be as high as 10 ± 5 %, it was much lower for Fe-P-C_Ar-NH900 (almost 5 %) which indicates that after ammonia treatment, the selectivity to produce H_2O during ORR increased meaningfully. The Fe-P-C_Ar-NH900 catalyst also shows relatively good durability behavior (Figure 6-5c). After 5000 cycles in N_2, 20 mV and 45 mV potential losses toward ORR were observed in onset and half-wave potentials, respectively.

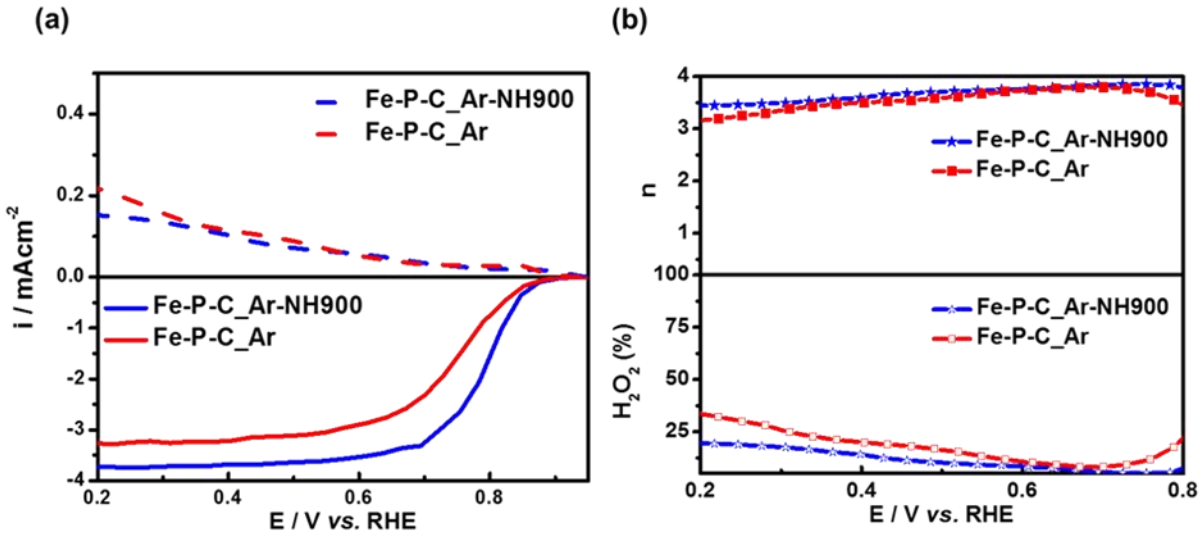

Figure 6-6 (a) RRDE results of Fe-P-C_Ar-NH900 and Fe-P-C_Ar in O_2 saturated 0.5 M sulfuric acid at 900 rpm rotational speed. The ring electrode was held at 1.2 V *vs*. RHE throughout the experiment. **(b)** The number of electrons transferred and H_2O_2 yield for Fe-P-C_Ar-NH900 and Fe-P-C_Ar measured from RRDE results.

In order to evaluate the Fe-P-C_Ar-NH900 catalyst particles under PEMFC operating conditions, they were integrated into the cathode of a single cell MEA. Although H_2-O_2 performance provides a gauge of the intrinsic catalyst layer activity, testing under H_2-air conditions enables its evaluation under working operating conditions. When applying air as the cathode reactant (Figure 6-5d), the MEA showed current densities of 77 mA cm^{-2} at 0.8 V and 537 mA cm^{-2} at 0.6 V, in addition to a maximum power density of 335 mW cm^{-2} To the best of our knowledge, the power densities and iR-free current densities in an H_2-air fuel cell achieved by Fe-P-C_Ar-NH900 are the best results reported to date in the literature for an NPMC electrode. The electrocatalyst morphology, with its high surface area of ca. 1100 m^2 g^{-}

[1] and variety of pores ranging in sizes from 2 to 200 nm, are the likely causes of the high H_2-air performance. This catalyst structure is conducive to mass transport through the catalyst layer, a factor that is increasingly important when using air as the reactant feed. The tuned chemical modification and porous catalyst morphology render Fe-P-C_Ar-NH900 an attractive non-precious ORR catalyst for PEMFCs, based on half-cell and fuel cell performance evaluations.

6.4 Conclusion

An NH_3 treatment was applied and optimized to tune the activity and improve the PEMFC performance of ORR catalysts derived from iron, PANI, and CNT. NH_3 contributed by enriching the N-dopant concentration, while the careful choice of the temperature had an impact on nitrogen dopant identity and ORR activity. The final catalyst (F-P-C_Ar-NH900) consisted of *in-situ* formed graphene-like structures that had well-distributed nitrogen and iron defects. F-P-C_Ar-NH900 exhibited high catalyst activity, including an $E_{1/2}$ of 0.81 V *vs*. RHE obtained from RDE testing. The MEA performance under H_2-air conditions that are application friendly yields current densities of 77 mA cm^{-2} at 0.8 V and 537 mA cm^{-2} at 0.6 V. Furthermore, a maximum power density of 335 mW cm^{-2} at 0.6 V was observed. This catalyst also showed a very good selectivity towards the 4-electron reaction with the number of electrons transferred per reduced oxygen molecule calculated to be 3.90 ± 0.05 by RRDE. These electrochemical evaluations indicate that the chemical modification of Fe-PANI-CNT catalyst by NH_3 results in a highly promising Pt-free PEMFC ORR electrocatalyst.

Chapter 7

Engineered Architectures with Nano-Channel Reactors (PANI-Fe-MCS)

This Chapter is adapted from a manuscript that is under revision in *Nano Energy*.

7.1 Introduction

PEMFCs are considered to be one of the most promising energy conversion technologies due to their technical benefits and environmental-friendliness.[167,168] In order to attain a solid performance which can compete with traditional ICE technologies, the inherently sluggish ORR at cathode must be overcome using electrocatalysts.[169] The main ORR catalysts are Pt-based but are expensive and their supply is monopolized.[116,117,170,171] Therefore, development of economically viable NPMCs with high activity toward the ORR and durability is an important path to commercialization of PEMFCs.[93]

M-N-C complexes currently represent the most promising candidates to substitute Pt-based ORR catalysts in PEMFCs.[161,172,173] By the careful selection of suitable metal and nitrogen precursors and catalyst supports as well as optimization of the synthesis conditions, a suite of highly attractive materials has been developed for PEMFCs.[72,146,151,162,174-177] Exploration of innovative synthesis strategies to tune the catalyst structures and morphologies that offer improved ORR activity and durability for hydrogen-powered PEMFCs, has become the key roadmap.[178] For desirable M-N-C catalysts, abundant micro-pores are required to host

active sites for high catalytic activity,[179] whereas sufficient meso- or macro-pores are also needed to ensure the effective mass transfer of reactant (air/O_2) and product (H_2O) through the entire thick cathode catalyst layer.[180,181] In addition, a highly conductive graphitic carbon phase is also viewed as an essential factor to facilitate charge transfer of the electrons, reduce the cell impedance and improve fuel cell performance.[182] These multifaceted requirements for catalyst morphologies and structures are crucial for designing and synthesizing the next-generation NPMCs that perform comparably to commercial Pt/C catalysts.

In this work, we present a 2D/3D hybrid carbon composite catalyst with improved fuel cell performance. This is achieved by in-situ polymerization of PANI on graphitic meso-porous carbon spheres (MCSs), followed by post-treatment leading to a nitrogenous intertexture of 2D graphene-like sheets/3D porous carbon spheres. The 2D/3D architecture should facilitate mass transfer through its meso-pores in carbon spheres and graphene-like layers. Moreover, the composite is predominantly micro-porous, hosting uniformly and densely dispersed ORR active sites throughout the graphene sheets and also within the carbon spheres. In addition, the graphitic character of this framework could contribute to fast electron transfer and confer high carbon corrosion resistance to the catalyst. Furthermore, these pores act as nano-channel reactors which provide smooth access to dense active sites by reactants and electrons and so impart excellent electrocatalytic performance.

7.2 Experimental

7.2.1 Preparation of MCS

MCSs were prepared by an aerosol-assisted spray drying technique.[183,184] Sucrose (6 g), nitrate hexahydrate (5 g), HCl (3 g, 0.5 M) and silicate template (14 g, AS-40, LUDOX) were sequentially added to deionized water (30 mL) while rigorously stirring. The aqueous solution so obtained was then purged with nitrogen gas, passed through an atomizer to form aerosol droplets and later sent to the drying zone (400 °C). After that, spherical particles containing silica/sucrose/nickel were collected on a membrane filter paper and then peeled off and carbonized at 900 °C in argon for 5 hours. Finally, HCl (2 M) and HF (10 wt%) solution was used in sequence to remove the nickel and silica, respectively.

7.2.2 Synthesis of PANI-Fe-MCS

Aniline (3 mL), $FeCl_3$ (5 g), APS, (2.5 g), and MCS (400 mg) were consecutively added to HCl solution (250 mL, 0.5 M). After constant mixing for 24 hours, the suspension was heated at 80 °C to dry. The collected solid materials were then calcined at 900 °C in argon for 1 hour. The pyrolyzed materials were then washed with H_2SO_4 (0.5 M) at 80 °C for 10 hours and were calcined again in argon and finally in ammonia gas.

7.2.3 Electrochemical Measurements

ORR testing was conducted using a Pine electrochemical station (Model AFCBP-1) with a conventional three-electrode method to evaluate the ORR activity. Ag/AgCl (filled with 3.0 M KCl) and graphite were used as the reference and counter electrodes, respectively. All

potentials in this study were then converted to RHE scale for better comparison. An RRDE containing a glassy carbon disk (5 mm diameter) and Pt ring (5.52 mm inner-diameter, 7.16 mm outer-diameter, collection efficiency N = 0.26) served as the working electrode. The ring potential was set to 1.20 V *vs.* RHE to detect H_2O_2 formed at the disc electrode. The catalyst ink was prepared by dispersion of catalyst powder (10 mg) with 1-propanol (1 mL) in an ultrasonic bath for 2h. Then 15 μL of the catalyst ink was pipetted onto the glass carbon surface and dried thoroughly in the air. Afterward, 3 μL of 0.05 wt% Nafion solution was dropped onto the catalyst layer, leading to a catalyst loading of approximately 0.6 mg cm^{-2}. The ORR activities were measured in an oxygen-saturated H_2SO_4 electrolyte (0.5 M) at room temperature by the stair-case method (potential step of 30 mV and wait-period of 30 s, 900 rpm). Accelerated durability testing (ADT) was carried out by cycling the electrode in nitrogen-saturated electrolyte between 0.6 and 1.0 V *vs.* RHE at 50 mV s^{-1} for 30,000 cycles. The performance of a Pt/C electrode (TKK, 28.2% Pt) with a Pt loading of 20 μg cm^{-2} was measured in 0.1 M $HClO_4$ solution as a benchmark.

The PANI-Fe-MCS catalyst was tested on the fuel cell cathode side to evaluate its activity and durability under PEMFC operating conditions. The dispersed ink containing PANI-Fe-MCS (40 mg), deionized water (0.5 mL), iso-propanol (0.5 mL), and Nafion (5 wt%, 400 mg), was directly painted onto a 5 cm^2 Nafion 211 membrane, to yield a loading of approximately 4 mg cm^{-2}. Commercial Pt-deposited carbon cloth (0.2 mg cm^{-2} Pt, Fuel Cell Etc) as gas diffusion electrode (GDE) was used on the anode side. The anode GDE, Nafion membrane with brushed catalysts and GDL (Sigracet 29 BC, Ion Power) were then assembled by hot-press at 120 °C for 5 mins using 600 lbs loading to fabricate MEAs. Fuel cell

performance was tested at 80 °C on a Model 850e fuel cell test system (Scribner Associates Inc.). The H_2 and O_2 flow rates were both set to be 300 sccm at 100% RH and a back-pressure of 20 psi gauge was applied. An H_2-air fuel cell durability test was conducted using an MEA fabricated with Nafion 115 ionomer membrane. The cell voltage was held at 0.4 V for 50 hours, and the current was recorded. The cell temperature was set to 80 °C; each gas was introduced at a rate of 300 sccm and 100 % RH and a back-pressure of 20 psi gauge was applied on both sides. Before recording, H_2 and air were fed for 1 h to condition the MEA.

Electrochemical impedance spectroscopy (EIS) experiments were carried out using a Gamry Interface 5000 potentiostat/galvanostat. Measurements were conducted at a cell voltage of 0.6 V, respectively, with an amplitude of 5 mV and frequency ranging from 0.01Hz to 100 k Hz. The impedance data were analyzed using Gamry software.

7.3 Results and Discussion

The overall process for the catalyst synthesis is illustrated in Figure 7-1. Aerosol assistant spray technique was used to prepare MCSs at first.[184] A silica sphere template with an average diameter of ca. 20 nm and nickel source were employed here to induce the porosity and enhance the graphitization degree of the carbon sphere, respectively.[185] After that, PANI which acts as the graphene and nitrogen precursor was polymerized in the presence of $FeCl_3$ followed by a thermal process at an elevated temperature of 900 ^oC to form *in-situ* graphene-like sheets on the MCS composite surfaces. This structure is denoted as PANI-Fe-MCS. For the purpose of comparison, support-free catalyst (PANI-Fe) and non-porous carbon sphere

based catalyst (PANI-Fe-NCS) were also prepared to highlight the clever combination of graphene-like sheets and porous carbon to boost fuel cell performance.

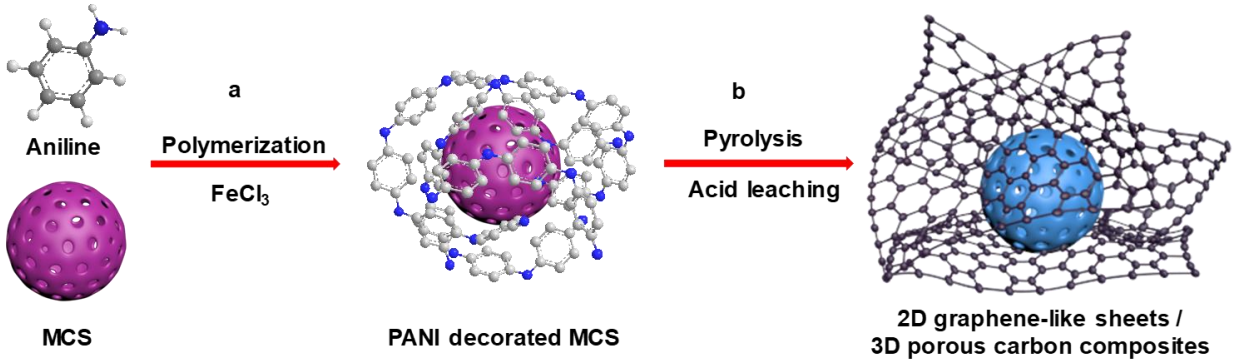

Figure 7-1 Synthesis schematic of PANI-Fe-MCS catalyst. **(a)** Polymerization of aniline onto the surface of the MCS in the presence of $FeCl_3$. **(b)** Subsequent calcination and acid leaching post-treatments.

The spherical morphology of the obtained carbon support is observed through SEM and TEM which show the sphere size to range from 200 nm to greater than 1 μm (Figure 7-2a,b). Magnified TEM image reveals the highly mesoporous sponge-like sub-structure with an average pore size of 20 nm in the carbon spheres (Figure 7-2c). Further HR-TEM images indicate the existence of large amounts of graphitized carbon within the whole carbon sphere, implying that it is partially graphitized, which could improve the electron conductivity and corrosion resistance of the NPMCs.[180] Upon polymerization and post-treatment, a significant amount of graphene-like sheet structure has grown (green arrows) and surrounds the carbon spheres (yellow arrows), as shown in the SEM and STEM images (Figure 7-2e,f). The carbon sphere morphology is likely to be preserved after the post thermal treatment and act as a spacer

to prevent the graphene-like layers from self-stacking. Moreover, the carbon spheres could provide potential channels to transfer ORR reactants and products. In addition, the close contact between the *in-situ* graphene and the graphitic carbon spheres should enable smooth electron transfer between them. Meanwhile, the large and extended multi-layer sheets could serve as large electroactive surface areas of catalysis. Notably, some nano-sized holes are readily observed on the *in-situ* formed graphene framework (Figure 7-2g), which probably are formed by the removal of Fe species during the sulfuric acid leaching step. These *in-plane* holes are favorable for mass transfer.

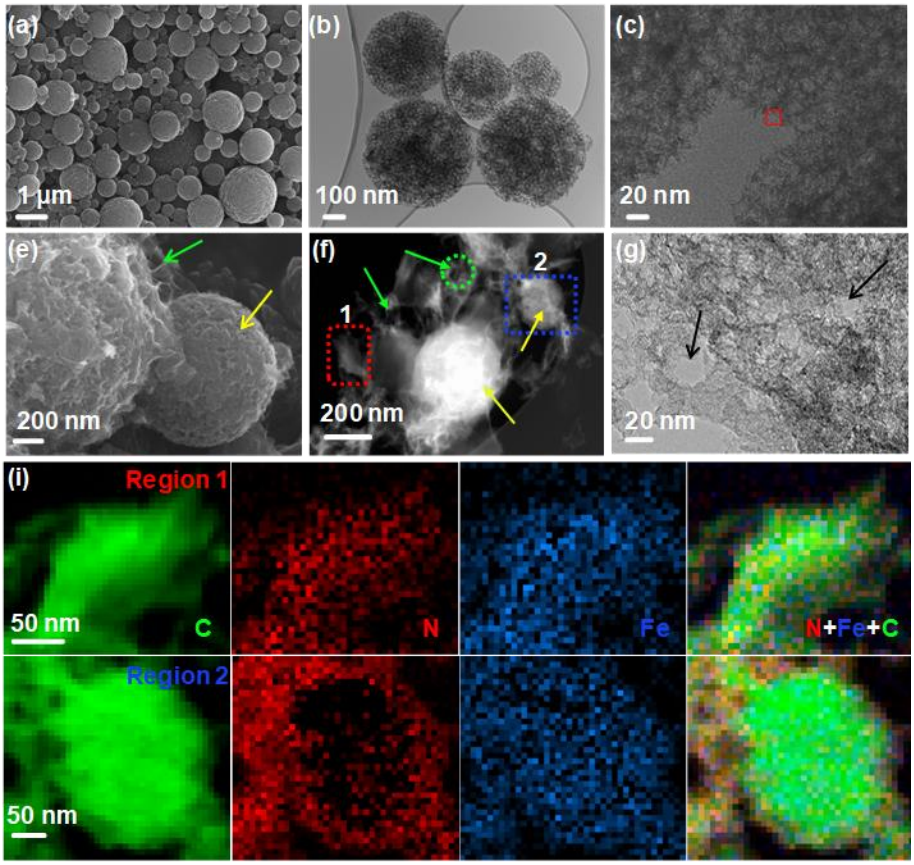

Figure 7-2 SEM **(a)**, and TEM **(b)**, **(c)** images of MCS. The red square designates the selected HR-TEM region. SEM **(e)**, STEM **(f)**, and HR-TEM **(g)** images of PANI-Fe-MCS. The green arrows designate the layered graphene-like sheets; the yellow arrows designate the porous carbon spheres, the green circle designates the selected HR-TEM region. Selected region 1 and 2 from **(f)** and corresponding **(i)** EELS mapping of carbon, nitrogen, iron, and overlaid iron, nitrogen, and carbon map.

EELS analysis was carried out to determine the elemental composition and its local distribution of C, N, and Fe across the catalyst composite. Two representive areas, (graphene sheets -region 1- and porous carbon -region 2) in Figure 7-2f, were selected for EELS imaging. The images in the upper row of Figure 7-2i confirm that the nitrogen, iron and carbon species

are well dispersed throughout the graphene-like structure while the lower ones suggest the nitrogen and iron elements may mainly reside in the outer layer of the carbon sphere. Moreover, the overlay of the carbon, nitrogen, and iron signals suggests that iron atoms are likely adjacent to nitrogen atoms at the atomic level, suggesting they could potentially coordinate with each other to form potential Fe-N moieties which are believed to be highly active for ORR.[186] Such advanced 2D/3D architecture, possessing a graphitic framework with multiple pores and dense highly active centers would be beneficial to boost the ORR activity and fuel cell performance.

Nitrogen adsorption-desorption measurements were conducted to analyze the BET surface areas and the porous nature of the prepared catalysts (Figure 7-3a). The MCS exhibits an isotherm with adsorption hysteresis, indicative of the presence of meso-pores. The BJH model shows that the pore size is centered at ca.20 nm, which is very consistent with the diameter of the silica templates. Such abundant meso-pores contribute a high BET surface area up to 1240 m^2g^{-1} for MCS (Figure 7-3b). PANI-Fe (Figure 7-3a) exhibits a micro-porosity feature which is in line with the narrowly distributed pore sizes centered at approximately 2 nm. This structure is further revealed by t-plot analysis that the microporous surface area (263 $m^2\ g^{-1}$) is predominant and occupies 86% of the total BET surface area (307 $m^2\ g^{-1}$). With both the isotherm and pore size distribution plots of PANI-Fe-MCS are similar to PANI-Fe with a little variation (Figure 7-3a). However, its BET surface area (1295 $m^2\ g^{-1}$), microporous surface area (1091 $m^2\ g^{-1}$) and external surface area (204 $m^2\ g^{-1}$) are dramatically increased in comparison with PANI-Fe (Figure 7-3b). Moreover, although the total BET surface area of PANI-Fe-MCS is close to MCS, the micro-pore and external surface areas are very different.

Specifically, the external surface area drops from 1189 $m^2 g^{-1}$ in MCS to 204 $m^2 g^{-1}$ in PANI-Fe-MCS, whereas the micro-pore surface area climbs to 1091 $m^2 g^{-1}$ in PANI-Fe-MCS from 51 $m^2 g^{-1}$ in MCS. Several can be provided for this dramatic variation in pore structures. First of all, the MCSs may act as spacers to prevent 2D graphene-like sheets from self-stacking as they are in PANI-Fe. As a result, the BET surface area of PANI-Fe-GMCS remains high. Hence, the fully exposed graphene-like sheets with dominant micro-pores could provide a large electrocatalytic surface area for the ORR. Second, after thermal activation, the MCSs may not collapse and probably still maintain their original meso-porous architecture in PANI-Fe-MCS, which could account for the enhanced external surface area. Such a high external surface area and large pore size of the PANI-Fe-MCS can promote the transfer of reactant and product efficiently toward and away from the catalytic sites within the bulk of the catalyst. Third, the drop of the external surface area of PANI-Fe-MCS (204 $m^2 g^{-1}$) in comparison with MCS (1189 $m^2 g^{-1}$) suspects that the newly formed graphene sheets partially block the meso-pores in MCS. In a word, such unique 2D/3D framework with dominant micro-pose and abundant meso-pores are favorable to improve the fuel cell performance.

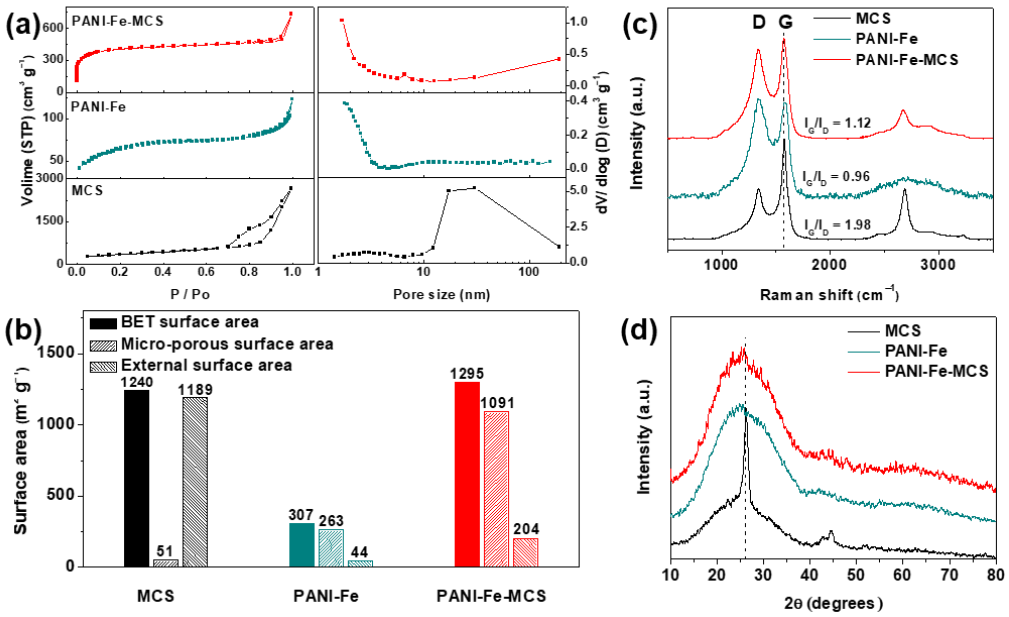

Figure 7-3 (a) Nitrogen adsorption–desorption isotherms and the corresponding BJH model pore size distribution, **(b)** surface areas, **(c)** Raman spectra and **(d)** XRD spectra of MCS, PANI-Fe, PANI-Fe-MCS.

Raman spectroscopy measurements were then employed to characterize the physical properties of the prepared materials. As can be seen in Figure 7-3c, D (1350 cm^{-1}) and G (1580 cm^{-1}) peaks are observed and respectively correspondent to the distorted carbon frames and the hexagonally bonded carbon atoms inside the carbon networks.[187] The I_G/I_D band ratio of MCS is about 1.98, which indicates its highly graphitic character. A band ratio of 0.96 is observed for PANI-Fe and a ratio of 1.12 is measured for PANI-Fe-MCS, implying a higher graphitic content than in PANI-Fe. XRD patterns of the samples were also collected to characterize their graphitic native further, as shown in Figure 7-3d. Remarkably, MCS gives a sharp peak at ca. 26.1° and the corresponding *d* space (002) is 0.341 nm, which is the strongest

evidence for the high-graphitic character of MCS. Meanwhile, PANI-Fe shows a relatively broad curve centered at ca. 24.8° with *d* space (002) of 0.358 nm, which is consistent with the formation of heteroatom-doped-graphene. As to PANI-Fe-MCS, a peak centered at ca. 25.4° with *d* space (002) of 0.348 nm was observed, due to the addition of graphitic MCS. The Raman, XRD and TEM results illustrate the highly graphitic character of PANI-Fe-MCS, which could contribute positively to the durability of the catalyst.[188]

The steady-state ORR polarization curves for all of the catalysts in oxygen-saturated 0.5 M H_2SO_4 electrolyte at a rotation speed of 900 rpm are provided in Figure 7-4a. All the carbon-supported (PANI-Fe-MCS and PANI-Fe-NCS) and unsupported (PANI-Fe) materials display similar ORR onset potentials, implying that the nature of the active sites is similar. The half-wave potential ($E_{1/2}$) for PANI-Fe-MCS is 0.80 V, ~ 19 and 26 mV improvement over that of PANI-Fe-NCS and PANI-Fe, respectively. Additionally, an RRDE study further indicated the fairly good ORR selectivity of PANI-Fe-MCS (Figure 7-4b). Remarkably, a low average H_2O_2 yield (< 1.0 %) is achieved by PANI-Fe-MCS over the potential range from 0.80 V to 0.20 V, when compared to that of PANI-Fe-NCS (1.0 % − 2.0 %) and PANI-Fe (1.5 % − 2.3 %). The electron transfer number of the PANI-Fe-MCS catalyst is calculated to exceed 3.98, which highlights the excellent selectivity toward the 4-electron reaction.

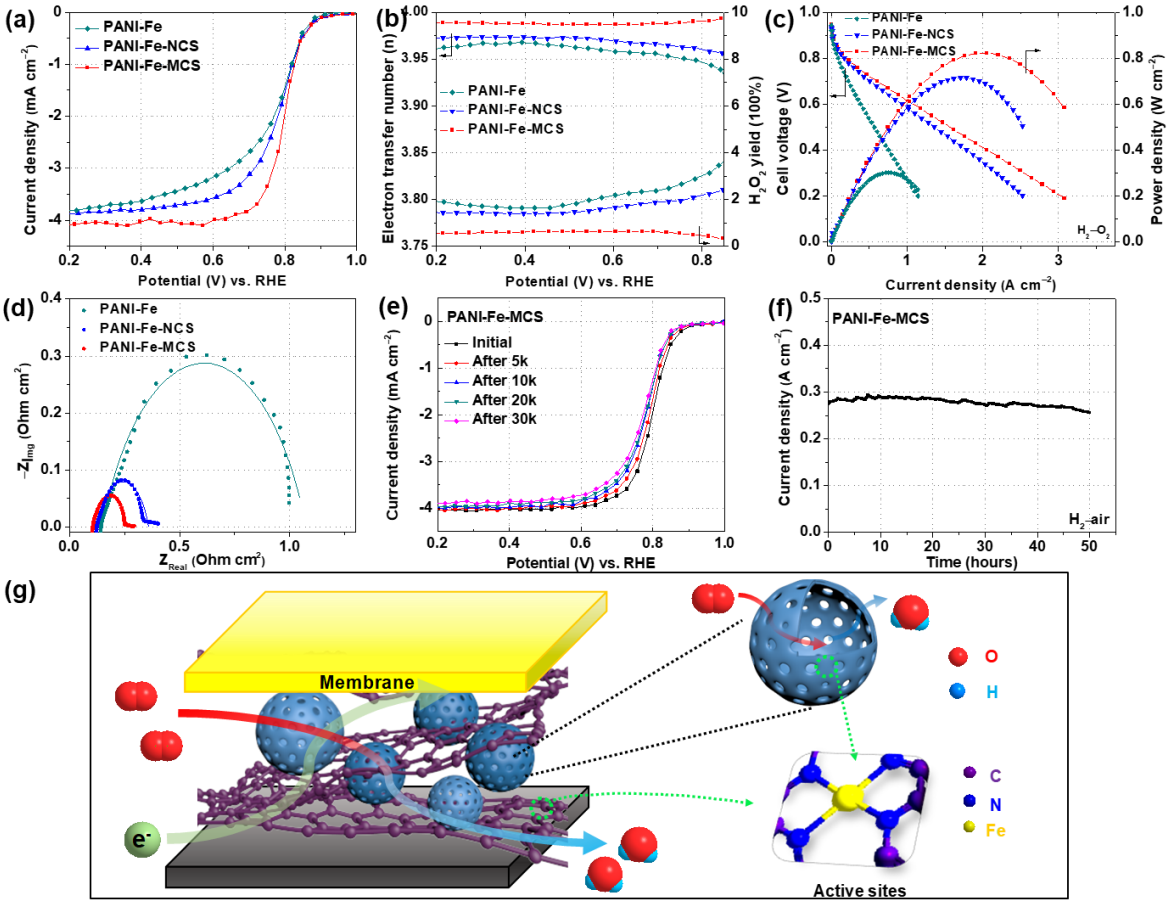

Figure 7-4 (a) RDE plots of prepared catalysts. **(b)** Electron transfer number and H_2O_2 yield of prepared catalysts. **(c)** Polarization and power density as functions of the current density for H_2–O_2 PEMFCs with the prepared composites as the cathode catalysts. Membrane: Nafion 211; cathode catalyst loading: ~4 mg cm^{-2}. **(d)** Nyquist plots for PEMFCs with prepared catalysts at cell voltage of 0.6 V. **(e)** ORR polarization plots assessed after multiple voltage cycling. **(f)** Short-term stability test of a PANI-Fe-MCS catalyst at a constant fuel cell voltage of 0.40 V. Membrane: Nafion 115; cathode catalyst loading: ~4 mg cm^{-2}. All the RDE/RRDE test conditions: 0.5 M H_2SO_4 saturated with O_2, 900 RPM, and catalyst loading of 0.6 mg cm^{-2}. **(g)** A schematic illustration correlating the physicochemical structures of PANI-Fe-MCS to its electrochemistry performance.

The high ORR activity of PANI-Fe-MCS is further confirmed by PEMFC measurements. Figure 7-4c presents the polarization and power density curves of fuel cells using either PANI-Fe-MCS, PANI-Fe-NCS or PANI-Fe as the cathode catalyst. All the three catalysts exhibit similar current densities in the high voltage region (kinetic limitation region), whereas PANI-Fe-MCS delivers the highest performance in the lower voltage region (transport limitation region). Meanwhile, the maximum power densities (P_{max}) of the cell with PANI-Fe-MCS reaches 0.83 W cm^{-2} at 0.40 V, significantly superior to that of 0.72 W cm^{-2} at 0.43 V and 0.29 W cm^{-2} at 0.41 V for PANI-Fe-NCS and PANI-Fe, respectively. Such a high output power density can reach approximately 60 % of the P_{max} (1.4 W cm^{-2}) of Pt cathode (0.2 mg_{pt} cm^{-2}) tested under the same conditions, representing one of the highest values in the NPMC field.

Further, the EIS was carried to evaluate the effect of catalyst properties on fuel cell performance. The Nyquist plots at a cell voltage of 0.6 V are shown in Figure 7-4d, from which one arc can be observed for both types of cells. The high-frequency intercept on the real axis yields the total ohmic resistance of the single cell (R_{ohm}) according to the equivalent model presented in Figure 7-5 . The diameter of the arc is a measure of the charge transfer resistance (R_{ct}) of the ORR.[189,190] It is evident that R_{ohm} does not differ significantly in the MEAs with PANI-Fe (0.14 Ω cm^2), PANI-Fe-NCS (0.12 Ω cm^2) and PANI-Fe-MCS (0.10 Ω cm^2) because these MEAs were fabricated with the same technique and the same membrane. From the figure, it is clear that the R_{ct} of ~0.14 Ω cm^2 for the MEA with PANI-Fe-MCS is much smaller than the values of 0.21 and 0.92 Ω cm^2 for PANI-Fe-NCS and PANI-Fe at 0.6 V, respectively. The lower R_{ct} value suggests that PANI-Fe-MCS is a more efficient electrochemical active

catalyst layer, which presumably can be attributed to the easily accessible dense active sites in both the extended graphene-like sheets and porous carbon support, as this is the main difference between these catalysts. These trends are consistent with their fuel cell behavior exhibited in Figure 7-4c: the lower the charge transfer resistance, the higher the single cell performance.

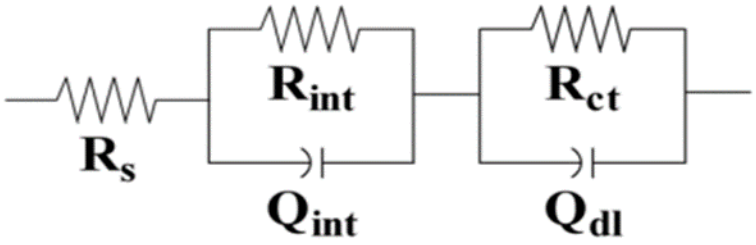

Figure 7-5 Equivalent circuit model used to fit the impedance spectra for PEMFC using Gamry software

To investigate catalyst durability, accelerated degradation testing (ADT) protocols based on the potentiodynamic method were performed to simulate the conditions of a practical cathode in a PEMFC system. The ADT involved potential cycling over a range of 0.6 to 1.0 V in a nitrogen-saturated 0.5 M sulfuric acid at a scan rate of 50 mv s^{-1} (DOE recommended conditions for non-Pt cathode catalysts).[191] Figure 7-4e shows a minor variation in the ORR polarization curves of PANI-Fe-MCS after different numbers of potential cycles. Only a 29 mV decrease in the half-wave potential is observed after 30,000 potential cycles, ranking it as one of the most durable NPMC catalysts reported in an acid electrolyte. To assess the durability of the MEA cathode made with PANI-Fe-MCS, a short-term durability test was

conducted at a constant cell voltage of 0.4 V (Figure 7-4f). The cell performance appears to remain very stable, showing only ca. 5 % loss of the initial current over 50 hours of operation. The excellent electrochemical durability of PANI-Fe-MCS for the ORR could be ascribed to the several features. Above all, the high degree of graphitization of the catalyst, including its *in-situ* formed graphene layer and graphitic carbon support, can enhance the resistance to carbon corrosion and avoid significant loss of active sites.[121,182] The good durability of PANI-Fe-MCS may also be related to the open porous structures that enhances oxygen transfer and water removal from the catalyst surface. This feature is very necessary for NPMC cathode layers that approach 100 mm in thickness.[192] Moreover, the small yield of H_2O_2 may mitigate its severe attack on active sites and thus slow down the degradation of ORR activity.[60,188]

In addition to focusing on the outstanding ORR performance of this catalyst, the major aim of this work is to probe and dig into the reason why the nano-scale architecture benefits fuel cell performance. Taking these extensive physicochemical characterizations into account, it is concluded that the 2D/3D framework plays a vital role in enhancing fuel cell performance, as shown schematically in Figure 7-4g**.** The figure depicts the overall structure of the catalyst as a coherent network of microspheres with nanopores on their surfaces that are wrapped with graphene nano-sheets. The pores on both structures act as nano-channels hosting the ORR. In addition, the ORR proceeds on improved active sites that are distributed with large populations on both catalyst textures. The improved performance can be explained in several ways. First, the 2D/3D intertexture can resist re-stacking of graphene and the aggregation of carbon spheres and produce a separated but connected layer/sphere framework with plenty of voids, favorable for mass transfer. Moreover, the carbon spheres further offer effective mass transfer through

their highly porous channels. Second, the graphene layers and carbon spheres provide an enormous electrocatalytic surface area which is populated with Fe-N ORR active sites. Third, the graphitic carbon layers and spheres provide a highly interconnected architecture that conducts the electrons throughout the entire catalyst. These features can well explain the enhanced activity and stability for the PANI-Fe-MCS catalyst. Last, the overall micro-sized structure provides an easy way for the catalyst layer deposition in the MEA. The possible synergistic strategy of building 2D/3D structures could provide a new approach in the design of ORR catalysts.

7.4 Conclusion

In summary, a framework containing 2D graphene-like sheets and 3D graphitic meso-porous carbon spheres with nano-channel reactors was synthesized as an ORR catalyst for PEMFC. It has a unique composite structure and morphology that benefits active sites, oxygen mass transfer, water removal from catalyst surfaces, carbon corrosion resistance, and electronic conductivity. These factors lead to impressive ORR activity and durability in fuel cell: a peak power density of 0.82 W cm^{-2} in a H_2–O_2 fuel cell and maintenance of 95 % of its initial current density after 50 hours of operation in air at constant 0.4 V. This paper provides a fresh approach to explore promising NPMCs that consists of effective mass and charge transfer channels with high population of active sites and develop a practical synthesis strategy for preparing highly active and durable PEMFC catalysts.

Chapter 8

In-Situ Polymer Graphenization Ingrained with Nanoporosity in Nitrogenous Electrocatalyst (Fe-N-C-Phen-PANI)

P. Zamani, X. Fu, J-Y. Choi, F. M. Hassan, G. Jiang, D. C. Higgins, Y. Zhang, Md A. Hoque, and Z. Chen, *Advanced Materials* 29 (2017) 1604456

Part of the work described in this chapter has been published as reference [193], with permission from John Wiley and Sons.

8.1 Introduction

Over the past decades, traditional ICE technologies have been progressively replaced with more sustainable alternatives, especially in the automotive transportation [93]. PEMFC is a highly efficient and environment-friendly energy conversion device that uses hydrogen and oxygen/air to generate electricity and has been considered one of the most attractive power sources for various applications including cars and backup powers [19]. However, numerous challenges still need to be addressed in order for them to become commercialized [194]. Currently, expensive Pt-based catalysts are the only viable catalysts. Yet, their high price, low stability, and limited reserves remain as the biggest challenges that hinder the commercialization [98,115-117]. In this regard, development of cost-effective and readily available

alternatives, NPMC materials for ORR is the long term solution for commercial application of PEMFCs [1,2,195,196].

Among these NPMCs, M-N-C complexes which have undergone high-temperature pyrolysis represent the most promising alternatives to replace Pt-based catalysts in PEMFCs [11,39,92,114,146,197-201]. As pioneers of this research area, Dodelet et al. have utilized filler materials and ball-milling to improve the ORR performance of Fe-N-C catalysts [56,65]. Two research groups have used the sacrificial template method to elevate the catalyst fuel cell performance [72,145]. Recently, Zelenay's research team in Los Alamos National Lab developed a new class of heteroatom polymer-derived catalysts with improved activity and durability in half cell and fuel cell tests [55,58,200]. Despite these signs of progress, the current state-of-the-art M-N-C catalysts still suffer from moderate activity and mass-transport properties, and therefore have not yet reached the fuel cell performance achieved by Pt/C-based catalysts [118]. In order to address these remaining challenges, it is necessary to maximize the electrochemical surface area of the catalyst, which is capable of hosting a large number of active sites towards ORR and hence boost the activity of M-N-C catalysts [12]. Meanwhile, by tuning the morphology, it is possible to control the meso/macro-pore sizes distribution to promote mass-transport of ORR-involved species (H^+, O_2, and H_2O) on the surface and within the bulk of the catalyst [180].

In this study, we develop an efficient strategy to synthesize Fe-N-C catalyst with *in-situ* formed 3D porous graphene-like structures by simultaneously using dual nitrogen sources, e.g., phenanthroline (Phen) and PANI. The dual nitrogen catalyst was achieved by introducing Phen into the pores of a carbon support by ball-milling, covering it with a PANI shell by polymerization of aniline, followed by several subsequent pyrolyses and acid leaching steps

leading to *in-situ* 3D porous graphene-like morphologies with a variety of types of pores. Phen appears to act as a pore-forming agent that is capable of expanding the external PANI shell during the decomposition. Simultaneously, the PANI shell is converted to a graphene-like structure in the presence of iron species during pyrolysis processes [61,202]. In this way, the resulting graphene-like morphology can provide a high surface area carbon matrix that hosts active sites to catalyze ORR [55]. Moreover, the abundant meso-/macro-pores generated inside the graphene framework can facilitate mass transfer. Electrochemical evaluation has shown that the dual nitrogen-derived catalyst exhibits a high half-wave potential ($E_{1/2}$ = 0.8 V) and small H_2O_2 yield (< 2.5 %) towards the ORR. Fuel cell experiments using this composite cathode catalyst in H_2–O_2 and H_2–air delivers maximum power densities (P_{max}) of 1.06 W cm^{-2} and 0.38 W cm^{-2}, respectively, ranking it among the best NPMC cathodes for fuel cell application. Also, the catalyst exhibits high electrochemical stability through ADT, displaying only an 18 mV decrease in the ORR half-wave potential after 10,000 potential cycles and maintaining 90% of its initial fuel cell current density at 0.6 V (non-iR-corrected) after 5000 voltage cycles. Herein, we have successfully developed a new catalyst using dual nitrogen precursors resulting in a porous graphene-like framework with enhanced density and accessibility of active sites as well as facilitated mass-transport through the porous voids. This approach enables the production of a high-performance Fe-N-C catalyst, which is in the best interest of the practical applications of PEMFCs.

8.2 Experimental section

For the synthesis of Fe-N-C-Phen-PANI, Phen (1,10-phenanthroline, 500 mg), $Fe(Ac)_2$ (30 mg) and commercial carbon KJ600 (Ketjenblack EC 600J, 500 mg) were first dispersed in ethanol (100 ml) and stirred at 80 °C until the liquid was completely evaporated and the remaining solids were ball-milled for 3 hours. The ball-milled powder mixture (400 mg) was then dispersed in 0.5 M HCl before adding aniline (1.5 ml), $FeCl_3$ (5.0 g) and ammonium peroxidisulfate (2.5 g) consecutively. After 48 hours of vigorous stirring, the liquid from the suspension was allowed to evaporate overnight. The collected solid materials were then pyrolyzed at 900 °C in Ar for 1 hour. The resulting powders were subsequently leached in 0.5 M H_2SO_4 for 8 hours followed by thorough washing with deionized water. Finally, the catalyst was heat-treated again in Ar for 3 hours and then in NH_3 for 15 mins at the same temperature as the first heat treatment. For the synthesis of Fe-N-C-PANI, pristine KJ600 (400 mg) was mixed with aniline (3.0 mL), $FeCl_3$ (10.0 g), and ammonium peroxidisulfate (5.0 g). After the polymerization, the mixture was heat-treated and acid leached in the same way as done to produce Fe-C-N-Phen-PANI. In order to synthesize Fe-N-C-Phen, the ball-milled mixture containing KJ600, Phen and $Fe(Ac)_2$ was subjected directly to the same heat treatment and acid leaching steps as used for Fe-C-N-Phen-PANI without the addition of aniline.

8.3 Results and Discussion

A schematic diagram illustrating Fe-N-C-Phen-PANI catalyst synthesis is shown in Figure 8-1. In a quick look, the pristine KJ600 was first mixed with Phen and $Fe(Ac)_2$ by ball

milling method. In ball-milled composites (labeled as KJ600/Fe/Phen) as opposed to pristine KJ600, a much lower BET surface area (12 m^2 g^{-1} versus 1321 m^2 g^{-1}), and discernable changes in SEM and TEM images were observed. The significant loss in BET surface area suggests that Phen fills the pores of the carbon support via ball-milling and occupy the majority of the mesoporous surface area and also block access to the internal porous surface area. Subsequently, PANI is coated onto these solid composites by polymerization of aniline in the presence of ammonium persulfate and $FeCl_3$. Then, these catalyst precursors are pyrolyzed at 900 $^{\circ}C$ under Ar atmosphere. Then, the heat-treated products are acid leached and subjected to remaining pyrolysis steps to obtain the final catalyst labeled as Fe-N-C-Phen-PANI. Here, Phen and PANI are employed not only as nitrogen-doping agents to promote catalytic activity towards ORR but also for their specific functions. In particular, Phen is primarily selected as a sacrificial pore-forming agent due to its lower thermal decomposition temperature compared to PANI. Hence, it tends to release a significant amount of gas when it decomposes during pyrolysis. The trapped gas increases the internal stresses and then expands the external PANI shell as it escapes, leaving abundant pores as accessible channels for gas and water to move within the catalyst layers. PANI is converted to a graphene-like structure during the graphitization process in the presence of Fe species [57]. In this way, it can further enhance the surface area of the catalyst and expose more active sites to catalyze ORR. The co-use of Phen and PANI as nitrogen sources provides an advantageous morphology for Fe-N-C-Phen-PANI, benefiting its ORR activity and fuel cell performance. For the sake of comparison, a single nitrogen source (PANI or Phen) is used to prepare Fe-N-C-PANI and Fe-N-C-Phen,

respectively, according to the previously reported procedures with slight modifications to match the synthesis conditions of the Fe-N-C-Phen-PANI catalyst [55,56].

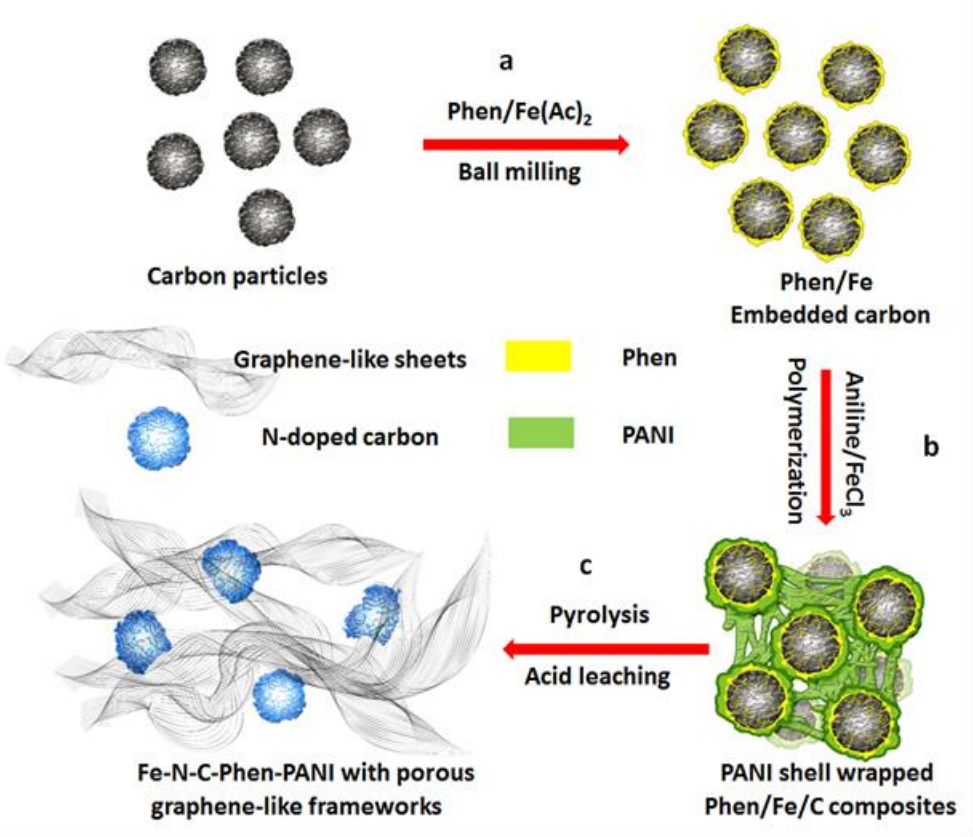

Figure 8-1 Synthesis schematic of Fe-N-C-Phen-PANI catalyst. **(a)** Ball milling of KJ600 carbon with Phen and $Fe(Ac)_2$. **(b)** Polymerization of aniline onto the surface of the Phen/Fe/C composites. **(c)** Subsequent heat-treatment and acid leaching process.

The surface morphology of these Fe-N-C catalysts was first analyzed by SEM and TEM. The co-use of dual nitrogen sources produce different carbon morphologies then that

observed in Fe-N-C-PANI and Fe-N-C-Phen. In comparison with KJ600, the pristine carbon black structures disappear in Fe-N-C-Phen and disordered carbon structures are formed (Figure 8-2b). Further HR-TEM image shows many amorphous carbon species (yellow arrows) within the Fe-N-C-Phen catalyst (Figure 8-2c). Similarly, the surface topologies of the PANI-based catalysts (Fe-N-C-PANI and Fe-N-C-Phen-PANI) also show bulk dense particles with average size of approximate 2 μm (Figure 8-2d,g). However, unlike the Fe-N-C-Phen catalyst, a significant amount of graphene-sheet-like structures are observed in the PANI-based catalysts (Figure 8-2e,h,). It is also evident from the HR-TEM images that the in-situ formed graphene-like sheets are multi-layered (green arrows) and surrounded by amorphous carbon (yellow arrows) (Figure 8-2f,i). Moreover, some differences between Fe-N-C-PANI and Fe-N-C-Phen-PANI catalysts are observed. For example, the SEM image shows outstretched graphene-like sheets apparently interspersed in and decorated on the Fe-N-C-Phen-PANI catalyst (Figure 8-2g), suggesting more graphene surfaces are exposed compared with Fe-N-C-PANI (Figure 8-2d). We propose that the decomposition of Phen molecules during pyrolysis likely expands the PANI shell during the formation of in-situ graphene-like sheets and inhibits their aggregation. TEM observation indicates a more porous graphene-like framework in Fe-N-C-Phen-PANI catalyst (Figure 8-2h) than Fe-N-C-PANI (Figure 8-2e). This porous graphene-like structure likely originates from the holes generated by expansion of PANI shell when Phen decomposes. Such porous graphene-like structures are beneficial to catalyst performance in several ways. First, the highly porous graphene-like framework could maximize the exposure and accessibility of active sites. Second, these robust porous structures could function as channels that facilitate the diffusion of ORR-related species. Also, the

formation of graphene-like sheets likely enhances the electronic conductivity and corrosion resistance of the catalyst [60,121]. Thus, such an advanced carbon structure could potentially play a crucial role in enhancing the ORR activity and fuel cell performance.

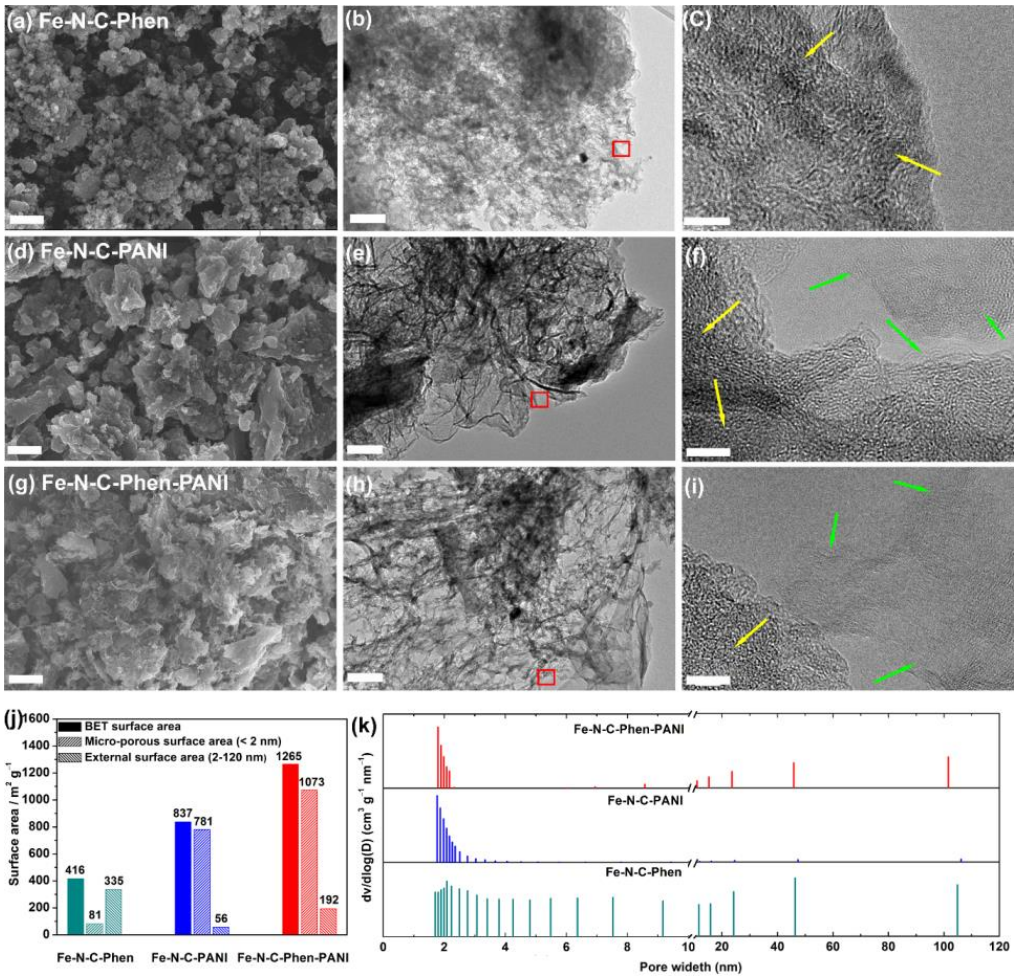

Figure 8-2 (a) SEM, **(b)** TEM and **(c)** HR-TEM images of Fe-N-C-Phen; **(d)** SEM, **(e)** TEM and **(f)** HR-TEM images of Fe-N-C-PANI; **(g)** SEM, **(h)** TEM and **(i)** HR-TEM images of Fe-N-C-Phen-PANI. **(j)** Surface areas of the prepared catalysts. **(k)** BJH model pores size distribution for the prepared catalysts.

SEM images scale bar, 2 μm. TEM images scale bar, 100 nm. HR-TEM images scale bar, 5 nm. Red squares designate the selected HR-TEM regions, green arrows designate the layered graphene-like sheets and yellow arrows designate amorphous carbon.

Nitrogen adsorption-desorption measurements were further conducted to analyze the porous nature of these Fe-N-C catalysts. As shown in Figure 8-2j, total surface areas of 1265 $m^2 g^{-1}$, 837 $m^2 g^{-1}$ and 416 $m^2 g^{-1}$ for Fe-N-C-Phen-PANI, Fe-N-C-PANI and Fe-N-C-Phen respectively are obtained. It is evident that the BET surface areas of Fe-N-C-Phen-PANI and Fe-N-C-PANI are higher than that of Fe-N-C-Phen, most likely due to the formation of graphene-like morphologies. On the other hands, the enhanced BET surface area in the dual nitrogen source-derived catalyst compare with Fe-N-C-PANI can be attributed to the addition of Phen as a pore-forming agent. Furthermore, vast differences in the surface area and pore size distribution (Figure 8-2j and Figure 8-2k) are observed among these three samples. The micro-porous surface area and external surface area are respectively 81 $m^2 g^{-1}$ and 335 $m^2 g^{-1}$ for Fe-N-C-Phen, corresponding to widely-distributed pore sizes ranging from 1.7 nm to 110 nm. On the other hand, the micro-porous surface area (781 $m^2 g^{-1}$) of Fe-N-C-PANI is predominant and occupies 93% of the total BET surface area (Figure 8-2j), which is in line with the narrowly distributed pore sizes centered at ca. 2 nm. In the case of Fe-N-C-Phen-PANI, both the microporous surface area (1073 $m^2 g^{-1}$) and external surface area (192 $m^2 g^{-1}$) are increased in comparison with Fe-N-C-PANI. Such growth mainly comes from the highly porous structures which are formed by the decomposition of Phen inside the PANI shell during the formation of the *in-situ* graphene-like morphology, which is in good agreement with the

TEM image in Figure 8-2h. Apparently, Fe-N-C-Phen-PANI contains many micropores (< 2 nm) as well as a significant amount of meso- and macro-sized pores in the range of 2 to 120 nm (Figure 8-2k). According to previous reports, it is believed that micro-pores with the ability to host active sites contribute mostly to the catalytic ORR activity [44,203] while the meso/macropores are required to transport the reactants and products efficiently to and from the catalytic sites in the micro-pores [180,181].

Raman spectroscopy and XPS analysis have also been conducted to investigate the physiochemical properties of these Fe-N-C catalysts. The Raman spectra in Figure 8-3a clearly show that the Fe-N-C-Phen-PANI and Fe-N-C-PANI have higher I_G/I_D ratios of 1.08 and 1.11, respectively, compared with 0.81 for Fe-N-C-Phen. The enhanced I_G/I_D ratio indicates the existence of more graphitic carbon in the Fe-N-C-Phen-PANI and Fe-N-C-PANI catalysts, in good agreement with the SEM and TEM images (Figure 8-2). From XPS surveys, it is found that Fe-N-C-Phen-PANI and Fe-N-C-PANI have similar overall N contents, which are higher than that of Fe-N-C-Phen. The high-resolution N 1s spectra of the three Fe-N-C catalysts have been further investigated. According to previous reports, the N 1s can be deconvoluted into five different peaks with binding energies of 398.2, 399.1, 400.2, 401.1, and 402.6 eV, corresponding to pyridinic N, Fe−N, pyrrolic N, graphitic N, and oxidized N, respectively (Figure 8-3b) [44,123]. No significant difference exists in the atomic concentrations of N species in Fe-N-C-PANI and Fe-N-C-Phen-PANI. Moreover, the overall Fe content of these catalysts is also very close to each other. Therefore, the XPS results suggest a similar nature and concentration of potential active site species for Fe-N-C-PANI and Fe-N-C-Phen-PANI. This

implies that the differences in electrochemical properties are only weakly correlated to the active site type and content.

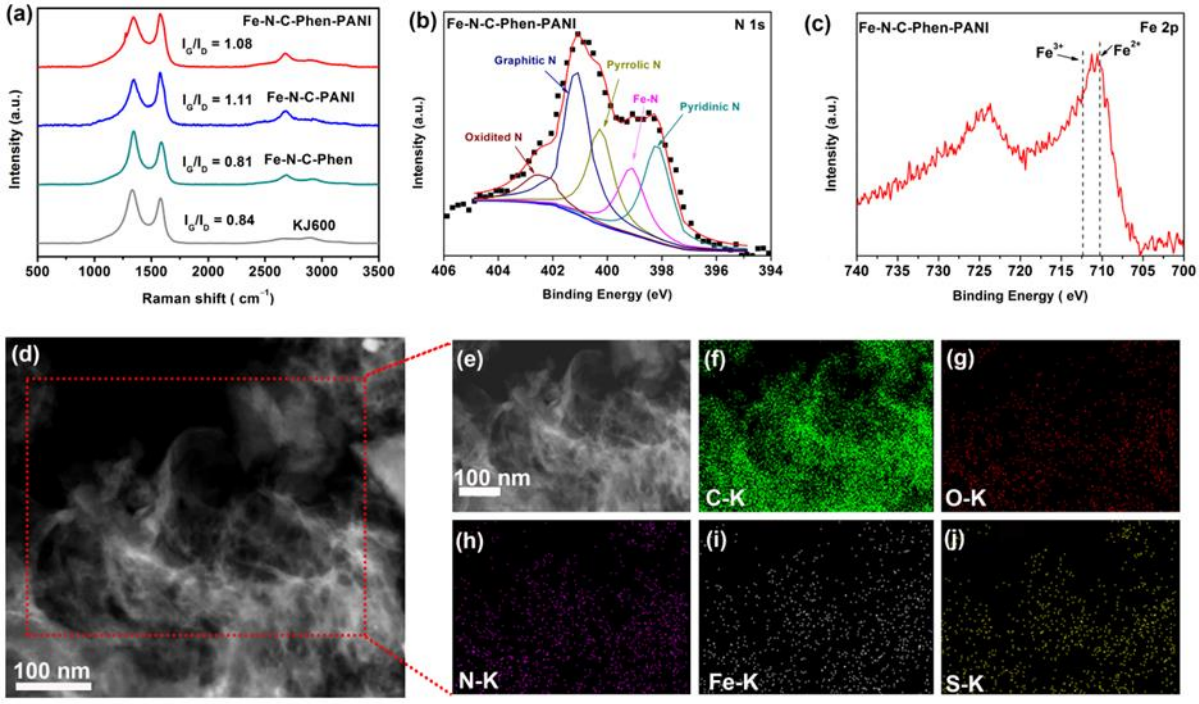

Figure 8-3 (a) Raman spectra of pristine KJ600, Fe-N-C-Phen, Fe-N-C-PANI, Fe-N-C-Phen-PANI; High resolution **(b)** N 1s and **(c)** Fe 2p peak of Fe-N-C-Phen-PANI. **(d)** STEM image of Fe-N-C-Phen-PANI **(e)** selected region from **(d)** and corresponding elemental mapping images of **(f)** C, **(g)** O, **(h)** N, **(i)** Fe and **(j)** S.

The STEM image shown in Figure 8-3d,e and the corresponding EDX elemental maps in Figure 8-3f-j have been obtained to further probe the elements and their distribution in the Fe-N-C-Phen-PANI catalyst. N and Fe species, which likely make up active sites [68,162,163,204],

are finely and uniformly dispersed throughout the graphene-like formwork along with C, O, and S, suggesting that the active sites are homogenously distributed throughout the sample. Thus, it can be concluded that the highly porous graphene-like framework is an excellent material to host potential active sites in Fe-N-C-Phen-PANI and thus enhance its active site density.

The steady-state ORR polarization curves indicated the dual nitrogen sources derived Fe-N-C-Phen-PANI catalyst exhibits slightly superior activity regarding the half-wave potential ($E_{1/2}$ = 0.80V) compared with Fe-N-C-PANI ($E_{1/2}$ = 0.79V) and much better performance than Fe-N-C-Phen ($E_{1/2}$ = 0.67V) (Figure 8-4a, Table 8-1). Moreover, the ORR activity of Fe-N-C-Phen-PANI shows a small difference with a state-of-the-art Pt/C (TKK, 28.2 wt%) catalyst, as the half-wave potential gap is ca. 70 mV. An RRDE study was further performed to investigate the selectivity of these Fe-N-C catalysts towards the 4-electron reduction of oxygen. The H_2O_2 yield of Fe-N-C-Phen-PANI catalyst remains below 2.5 % in the potential range from 0.80 V to 0.20 V, which is lower than 3.0 %−5.0 % and 3.0 %−10.0 % for Fe-N-C-PANI and Fe-N-C-Phen catalysts, respectively (Figure 8-4b). The electron transfer number of Fe-N-C-Phen-PANI catalyst is above 3.95 (Figure 8-4b), superior to that of 3.91 and 3.82 for the Fe-N-C-PANI and Fe-N-C-Phen catalysts, respectively, indicating a very high selectivity towards the 4-electron reaction.

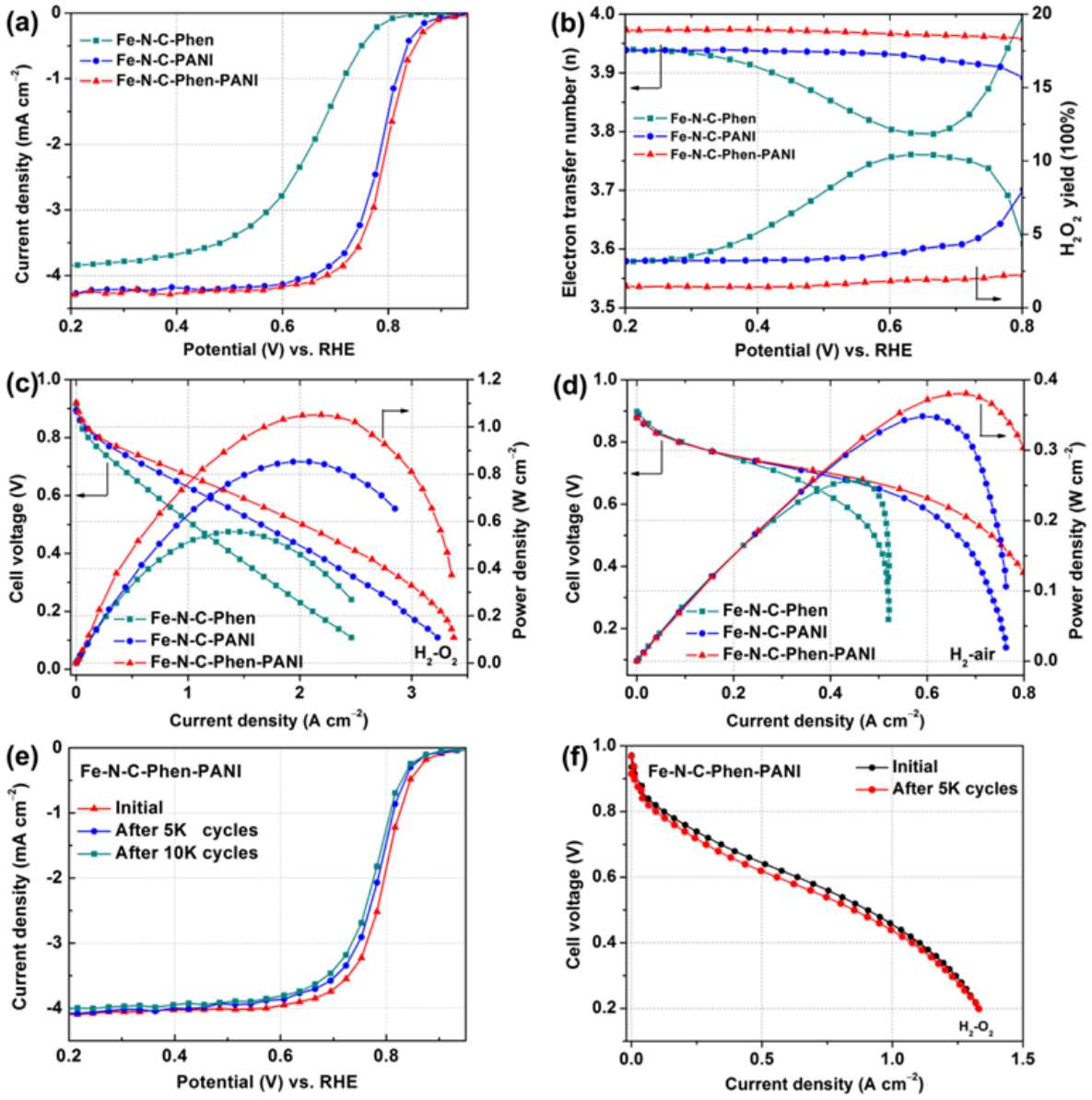

Figure 8-4 (a) Steady-state ORR polarization plots of prepared catalysts; **(b)** Electron transfer number and H_2O_2 yield of prepared catalysts; Polarization and power density as the functions of the current density plots for **(c)** H_2−O_2 and **(d)** H_2−air PEMFC with the prepared materials as the cathode catalysts. **(e)** ORR polarization plots assessed after multiple voltage cycling **(f).**

H_2–O_2 fuel cell polarization curves of the Fe-N-C-Phen-PANI catalyst cathode measured initially and after 5K cycles.

Membrane: Nafion 211; cathode catalyst loading: 4 mg cm^{-2}. All the RDE/RRDE test conditions: 0.5 M H_2SO_4 saturated with O_2, 900 RPM, 10 mV s^{-1}, catalyst loading of 0.6 mg cm^{-2}. All the durability tests were done in nitrogen saturated electrolyte by cycling from 1.0 to 0.6 V.

Table 8-1 Physical and chemical properties and electrochemical performance of the catalysts

Catalyst	**N content (at.%)**	$E_{1/2}$ **(V)**	P_{max} **(H_2–O_2) (W cm^{-2})**	P_{max} **(H_2–air) (W cm^{-2})**	**BET surface area (m^2 g^{-1})**	**Microporous surface area (m^2 g^{-1})**	**External surface area (m^2 g^{-1})**
Fe-N-C-Phen	1.89	0.67	0.56	0.26	416	81	335
Fe-N-C-PANI	4.18	0.79	0.87	0.34	837	781	56
Fe-N-C-Phen-PANI	3.96	0.80	1.06	0.38	1265	1073	192

The improved ORR activity of Fe-N-C-Phen-PANI is further confirmed by the PEMFC tests. Polarization and power density curves have been obtained for MEAs consisting of the Fe-N-C catalysts as cathodes for ORR and Pt/C catalyst as the anode for hydrogen oxidation reaction. In H_2–O_2 fuel cells, the Fe-N-C-Phen-PANI MEA shows a kinetic current density of 0.39 A cm^{-2} at 0.8 V (iR-corrected), which is higher than that of 0.33 A cm^{-2} and 0.16 A cm^{-2} for Fe-N-C-PANI and Fe-N-C-Phen, respectively, ranking it among the most active NPMC-

based cathodes reported to date. Figure 8-4c shows non-iR-corrected polarization and power density curves of the three catalysts and indicates that the fuel cell performance of Fe-N-C-Phen-PANI outperforms that of Fe-N-C-PANI and Fe-N-C-Phen over the entire test range. At a working voltage of 0.6 V, the power density of the MEA made with Fe-N-C-Phen-PANI reaches 0.86 W cm^{-2}, 125% and 205% higher than that of the MEA made with Fe-N-C-PANI (0.69 W cm^{-2}) and Fe-N-C-Phen (0.42 W cm^{-2}), respectively. Further, the P_{max} of the cell with Fe-N-C-Phen-PANI achieves a high value of 1.06 W cm^{-2} at 0.46 V, significantly superior to that of 0.87 W cm^{-2} at 0.43 V and 0.56 W cm^{-2} at 0.41 V for Fe-N-C-PANI and Fe-N-C-Phen, respectively (Figure 8-4c). To the best of our knowledge, this is the highest reported H_2–O_2 fuel cell power density to date by an NPMC cathode (Table 8-2).

In order to acquire sufficient performance, NPMC-based membrane cathodes usually require higher catalyst loading compared with that of Pt-based cathodes, resulting in a thicker catalyst layer that inevitably limits mass transfer. However, the Fe-N-C-Phen-PANI based cathode with the catalyst loading of ca. 4.0 mg cm^{-2} and measured thickness of ca. 90μm (Figure 8-5), can attain approximately 75% of the P_{max} (1.4 W cm^{-2}) of a Pt cathode (0.2 mg_{pt} cm^{-2}) operated with H_2–O_2 under the same conditions (Figure 8-4c, Figure 8-6a), which is considerably higher than that of Fe-N-C-PANI (62%) and Fe-N-C-Phen (30%). Moreover, the polarization curve of Fe-N-C-Phen-PANI matches well with that of Pt/C at small current densities (< 0.5 A cm^{-2}) and relatively close to Pt/C at high current densities (> 0.5 A cm^{-2}) (Figure 8-4c, Figure 8-6a). This approach enabled us to synthesize catalysts with reproducible performances (Figure 8-7).

The top fuel cell performance of Fe-N-C-Phen-PANI and Fe-N-C-PANI in comparison with Fe-N-C-Phen is attributed to their relatively higher overall nitrogen content and the elevated surface area (Table 8-1). However, considering the similar elemental compositions of the Fe-N-C-Phen-PANI and Fe-N-C-PANI based on the XPS results, we suggested that the enhanced performance of Fe-N-C-Phen-PANI is not likely associated with N and Fe species and instead is linked to its increased surface area (Table 8-1). According to this table, the superior surface area originates from two factors, the micro-pores, and meso-/macro-pores. To the extent of our knowledge, among the NPMCs with high H_2–O_2 power densities referenced in Table 8-2 and other high-performance NPMCs reported up to date, Fe-N-C-Phen-PANI exhibits the highest micro-porous surface area which comprises the active sites and supplies sufficient ORR activity to achieve the high level of fuel cell performance. Also, although high microporosity is required as a prerequisite for good activity in NPMCs, meso-/macro-porosity are essential for effective mass transport. Thus, we believe that the large boost in meso-/macro-porosity, about 3.4 times higher than that of Fe-N-C-PANI, imparts superior mass-transport especially at high current densities. Such surface area properties and other characteristics of Fe-N-C-Phen-PANI can repeatedly be achieved in different synthesis batches using the dual-nitrogen method, so that the catalyst performance is easily reproducible with no major current density variations at 0.6 V (non-iR-corrected) (Figure 8-7).

To simulate the actual operating conditions of PEMFCs, we tested the catalyst using air flow to the cathode as the oxidant. As shown in Figure 8-4d, the polarization curves of these Fe-N-C catalysts in H_2–air conditions follow similar trends to that observed in the H_2-O_2 fuel cells. The current density values at 0.8 V (iR-corrected) are 0.12, 0.11 and 0.09 A cm^{-2} for Fe-

N-C-Phen-PANI, Fe-N-C–PANI and Fe-N-C-Phen, respectively. The Fe-N-C-Phen-PANI yields a P_{max} value of 0.38 W cm^{-2} at 0.56 V, which exceeds the values measured with Fe-N-C–PANI (0.34 W cm^{-2} at 0.58 V) and Fe-N-C-Phen (0.26 W cm^{-2} at 0.55 V) and reaches approximately 63% of the P_{max} (0.6 W cm^{-2}) attained by the Pt cathode under the identical operating conditions (Figure 8-6b).

Table 8-2 Comparison of fuel cell performance of Fe-N-C-Phen-PANI materials with published state-of-the-art M-N-C catalysts

Catalyst	**T_{cell} (°C)**	**H_2/O_2 flow rate (sccm)**	**Back pressure (gauge) (psig)**	**MEA area (cm^{-2})**	**P_{max} in H_2-O_2 fuel cell (mW cm^{-2})**	**Reference**
Fe-N-C-Phen-PANI	80	300/400	20	5	1060	This work [193]
F/N/C-SCN	80	300/300	29	1	1030	[199]
Fe/Phen/Z8	80	300/300	15	5	910	[65]
FeCBDZ	80	100/100	25	5	700	[72]
PANI-FeCo-C	80	200/600	26	5	550	[55]

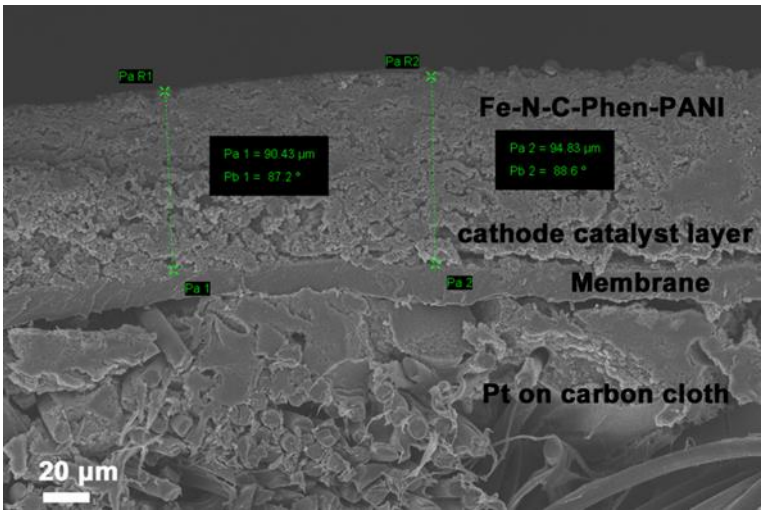

Figure 8-5 Direct measurements of the cathode catalyst layer thickness on an MEA with Fe-N-C-Phen-PANI loading of ca. 4 mg·cm^{-2}.

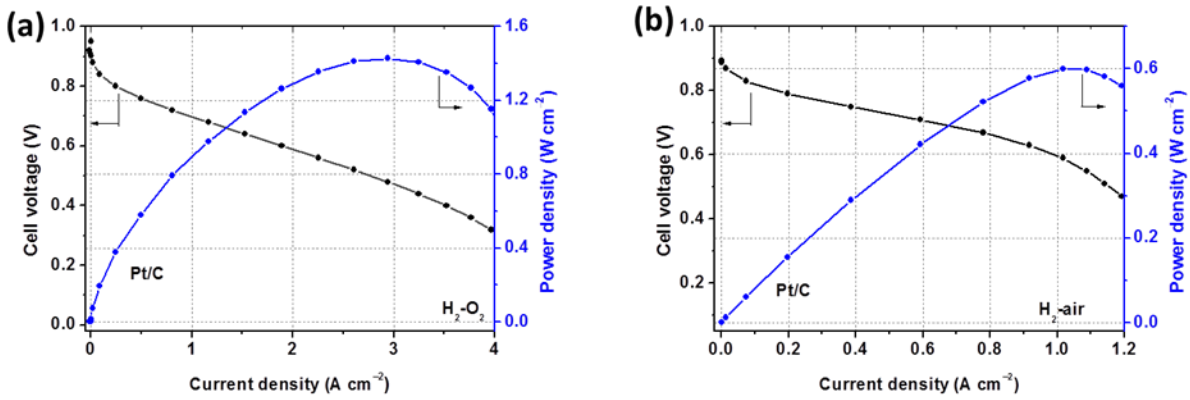

Figure 8-6 Polarization and power density as functions of current density for **(a)** H_2−O_2 and **(b)** H_2−air PEMFC with Pt/C as both the cathode and anode catalysts.

Nafion 211 was used as the membrane. The gas humidifier and cell temperature were maintained at 80 ˚C. The partial pressures of H_2 and O_2 (air) were both kept at 20 psig, and the gas flow rate for H_2 and O_2 (air) is 300 and 400 sccm, respectively.

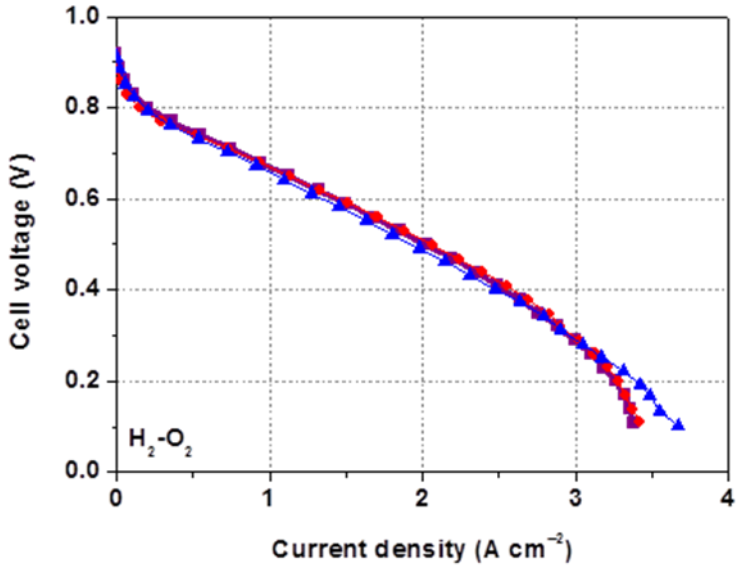

Figure 8-7 Reproducibility of the composite performance. Polarization plots for the H_2–O_2 fuel cell with Fe-N-C-Phen-PANI composites obtained in three different batches.

Catalyst loading: ca. 4 mg cm^{-2}; cell temperature: 80; Nafion 211 membrane; the back pressure of 20 psig for H_2 and O_2; gas flow rate of 300 and 400 sccm for H_2 and O_2.

Fe-N-C-Phen-PANI furthermore showed good stability based on ADT. The cycling was performed within a potential (RDE) and voltage (fuel cell) range of 0.6 to 1.0 V in nitrogen gas at a scan rate of 50 mV S^{-1}. Figure 8-4e shows the variation of ORR polarization curves

of Fe-N-C-Phen-PANI catalyst after different numbers of potential cycles; the half-wave potential loss is only 18 mV after 10,000 potential cycles. It can also be seen in the polarization curve obtained after 5000 cycles that the MEA performance is well-maintained compared to the initial one and the current density loss at 0.6 V (non-iR corrected) is only 70 mA cm^{-2}, retaining 90% of its initial fuel cell performance (Figure 8-4f). The excellent stability of Fe-N-C-Phen-PANI for ORR is likely due to the presence of abundant graphene-like structures (Figure 8-2h) that are highly resistant to carbon corrosion compared with conventional carbon black materials [188]. The improved stability can also be due to the low yield of H_2O_2 during ORR (Figure 8-4b), which is one of the primary sources for active site degradation and destruction of Nafion membrane [8,60]. To put it in a nutshell, the dual nitrogen-based Fe-N-C-Phen-PANI catalyst with unique 3D porous graphene-like framework shows exceptional fuel cell performance and remarkable durability and could serve as promising cathode material for PEMFCs.

8.4 Conclusion

In summary, two nitrogen precursors Phen and PANI have been used together to fabricate a new Fe-N-C catalyst for PEMFC. The catalyst possesses an abundance of 3D porous graphene-like structures, which can host a high population of reactant-accessible active sites for ORR and also facilitate mass-transport. A membrane electrode assembly using this catalyst at the cathode has delivered unprecedented P_{max} values of 1.06 W cm^{-2} and 0.38 W cm^{-2} in H_2–O_2 and H_2–air fuel cell, respectively, and also exhibit good stability. This study demonstrated the

in-situ formation of highly porous graphene structures that yield unprecedented performance of Fe-N-C-Phen-PANI catalyst, and paves the way for further development of active and durable Fe-N-C catalysts for PEMFC applications.

Chapter 9

Conclusions and Future Work

9.1 Summary and Conclusions

Although the fuel cell performance of heat-treated NPMCs has been dramatically improved over the past two decades, further improvements are still required to compete with state-of-the-art Pt catalysts. Since pyrolysis of different combinations of nitrogen precursors, metal precursors, and carbon supports produce catalysts with varying degrees of ORR activity, researchers have adopted a variety of precursors and synthetic approaches to advance NPMCs. Though indispensable, heat treatment destroys the initial structure of the precursors, producing a highly heterogeneous, complicated structure that makes it very difficult to elucidate and understand the active site(s) of the resulting NPMCs. For this reason, the development of NPMCs depends more on a trial-and-error type approach, rather than on a scientific basis that is rationally guided by fundamental knowledge concerning the active site structure(s) and formation. It is, therefore, becoming increasingly clear that a better understanding of active sites is required to propel NPMC development to new levels. According to published papers on NPMCs, nitrogen precursor selection plays one of the most important roles in the ORR activity when comparing a variety of NPMCs. Therefore, a better understanding of the influence of how the structure and properties of the different nitrogen precursors the nanostructure, surface properties and activity of the resultant catalysts after heat treatment is an important starting point.

Another important issue related to this type of NPMCs is durability. Until now, no NPMC has been shown to be durable under practical PEMFC operating conditions. From a practical application viewpoint, durability is as important as activity. Therefore, the understanding of the cause of performance loss of NPMCs and development of durable alternatives are also urgent research fields. The application of a host of diverse physicochemical analysis tools in conjunction with electrochemical and fuel cell tests is crucial to this endeavor and has been the focus of a large number of investigations. Considering the complex structure of NPMCs, thorough investigations must be carried out to provide fundamental insight, and build on previous studies. Sophisticated techniques, including a host of microscopy and spectroscopy methods, are required in tandem, with the ability to investigate catalysts *in situ* (either in "half-cell" or MEA) and provide breakthroughs in elucidating the active site structure(s) of the most active NPMCs prepared to date.

In order to develop NPMCs with high ORR activity that exhibit adequate MEA performance and durability in the PEMFCs, several procedures were followed to synthesize different NPMCs. The first effort was to develop one-dimensional nanofibers prepared by electrospinning and subsequent heat treatment. Chapter 5 focused on the successful fabrication of a Co-N decorated porous graphene aerogel catalyst and an in-depth analysis of the nitrogen groups. In Chapter 6, ammonia treatment was applied to tune the structure and activity of electrocatalysts derived from Fe, PANI and a carbon support. Following this study, Chapter 8 was concerned with utilizing dual nitrogen sources to prepare a highly active Fe-N-C electrocatalyst with in-situ graphene-like structures and tuned micro/meso/macro-porous morphology. A summary of all chapters is provided in the following paragraphs.

In Chapter 4, one-dimensional nanofibers were prepared by electrospinning an iron–polyaniline/polyacrylonitrile metal-polymer blend, followed by heat treatment. PANI was selected as it had previously been demonstrated to be an ideal nitrogen precursor to produce some of the most active NPMCs to date, due to its aromatic ring structure with a high content and uniform distribution of nitrogen species that could readily form nitrogen-doped graphitic carbon structures during heat treatment. PAN was also helpful as a low-cost polymer carrier to overcome the poor solubility of PANI in solution and as a secondary source of nitrogen. When 10 wt. % PANI was used to the electrospinning mixture, the resulting catalyst exhibited 100 and 70 mV improvements to the ORR onset potential and half-wave potential, respectively, rendering the most active non-precious ORR nanofiber catalysts prepared by electrospinning as of the date of publication. The high activity is attributed to the porous structure of the nanofibers, combined with the increased nitrogen content provided by PANI incorporation. With this unique synthetic approach, practical progress has been made toward the development of one-dimensional non-precious metal-based catalysts for fuel cell applications.

A procedure to synthesize a Co-N decorated graphene aerogel-based catalyst was explained in Chapter 5 to exploit several attractive features of graphene such as large corrosion resistance, and enhance ORR performance. PANI, which serves as a hydrogel-forming agent and nitrogen precursor, can block graphene sheets from re-stacking and raise the nitrogen dopant content. The final Co-N-GA framework has a high BET surface area and hierarchically porous skeleton as well as a uniform distribution of Co-N active sites, which can expose the more active sites to electrochemical interface and further facilitate the mass transport to

enhance the ORR activity and stability. The last Co-N-GA exhibited high ORR activity ($E_{1/2}$ = 0.73 V), superior electrochemical durability and high electron transfer selectivity (n >3.75) in an acidic environment. This prominent electrochemical performance makes the Co-N-GA a promising NPMC for PEMFCs.

In the next research (Chapter 6), NH_3 treatment was utilized to tune the morphology and performance of electrocatalysts fabricated from $FeCl_3$, PANI, and CNTs. By controlling the NH_3 reaction conditions, we were able to tune the chemistry of nitrogen incorporation, including concentration and dopant type. The final catalyst has a robust morphology consisting of highly porous 2-D *in-situ* formed graphene-like structures that, along with the intermixed 1-D CNTs, were decorated with an abundance of nitrogen and iron species. The catalyst derived under the optimized condition (F-P-C_Ar-NH900) exhibited high catalyst activity, including an $E_{1/2}$ of 0.80 V *vs* RHE based on RDE testing. When incorporated into an MEA under H_2-air conditions, current densities of 77 mA cm^{-2} at 0.8 V and 537 mA cm^{-2} at 0.6 V were achieved. Furthermore, a maximum power density of 335 mW cm^{-2} at 0.6 V was observed. To the best of our knowledge, this is one of the best H_2-air performances shown to date of publication for a Pt-free cathode. This catalyst also showed a very good selectivity towards the 4-electron reaction with the number of electrons transferred per reduced oxygen molecule was calculated to be 3.90 on the basis of RRDE measurments. These electrochemical evaluations indicate that the chemical modification of Fe-PANI-CNT catalyst by NH_3 results in a highly promising Pt-free PEMFC ORR electrocatalyst.

In Chapter 7, a 2D graphene-like sheet and 3D graphitic meso-porous carbon sphere framework with nano-channel reactors was synthesized as an ORR catalyst for PEMFC. It has

unique composite structures and morphologies that benefit active site residence, oxygen mass transfer, water removal from catalyst surfaces, carbon corrosion resistance, and electronic conductivity. These modifications lead to impressive ORR activity and durability in fuel cell: a peak power density of 0.82 W cm^{-2} in a H_2–O_2 fuel cell and a maintenance of 95 % of its initial current density after 50 hours of operation in air at constant 0.4 V. This research, therefore, provides a fresh approach to developing promising NPMCs with effective mass and charge transfer channels containing a high population of active sites and developing a practical synthesis strategy to prepare highly active and durable PEMFC catalysts.

Following the previous studies, an efficient strategy of utilizing dual nitrogen sources for highly active Fe-N-C electrocatalyst with *in-situ* formed graphene-like structures and tuned micro/meso/macro-porous morphology was reported in Chapter 8. This approach was achieved by simultaneously using PANI as the graphene precursor and Phen as the pore-forming agent, followed by several post–treatments. This research was accomplished by introducing Phen into the pores of carbon support by ball-milling, covering it with a PANI shell through polymerization of aniline, and then carrying out subsequent pyrolysis and acid leaching steps leading to the formation of *in-situ* 3D porous graphene-like morphologies with multiple types of pores. Here, Phen was capable of expanding the external PANI shell during its decomposition. Simultaneously, the PANI shell was converted to a graphene-like structure through graphenization in the presence of iron species during pyrolysis. Extensive physical characterization indicated that the final catalyst provided a rich, porous graphene framework decorated with uniformly dispersed active sites. The catalyst exhibited high maximum power densities of 1.06 W cm^{-2} and 0.38 W cm^{-2} in H_2–O_2 and H_2–air fuel cell tests, respectively,

representing one of the highest reported values to date for NPMCs in PEMFCs. Moreover, ADT showed it to have good fuel cell durability. The unprecedented performance of this electrocatalyst in fuel cell is linked to the highly porous graphene framework with a broad distribution of pore sizes, which can maximize the number of active sites with enhanced accessibility, facilitate the mass transport, and improve the carbon corrosion resistance.

9.2 Proposed Future Works

Based on the findings of these studies, some future directions for the catalyst research can be suggested:

9.2.1 High-performance NPMC development

Synthesis of NPMCs with different nitrogen precursors based on the high surface area carbon support such as graphene is encouraged. Since few studies have been done on NPMCs with a graphene aerogel as support, various combinations of the currently available heteroatom or metal precursors will likely improve ORR activity further. However, since the activity and especially stability measured in RDE experiments may not reflect actual PEMFC performance, it should be tested in an MEA as well.

Other approaches that can be used to synthesize highly porous and high surface area NPMCs include using spray dryering or aerosol-assisted surfactant self-assembly process.

High surface area catalysts should provide more exposed active sites for excellent mass transport of oxygen and water that will further improve ORR activity and stability.

9.2.2 Catalyst layer development

More study on various MEA compositions (e.g. different catalyst-to-Nafion ratios) can be done. Investigation into the hydrophilicity of the catalyst layers of micro/mesoporous, mesoporous, and macroporous dominating materials will provide more information regarding the wetting and its connection to stability. Catalysts with more or less hydrophobic support would likely perform uniquely, and together with amorphous or crystalline catalyst support (more or less prone to carbon oxidation), the search could supply more data on the relationship among the stability failure and the carbon oxidation.

9.2.3 Pt and NPMC hybrid catalysts

Although it is challenging to identify one unique degradation mechanism for all NPMCs owing to the diversity of synthetic designs and approaches, one mechanism that is broadly accepted involves the oxidative attack by H_2O_2 and its radicals. In spite of previous efforts, little success has been accomplished in understanding the loss, and no strong strategies have yet been investigated to address this challenge through a synthesis method. Interestingly, platinum is well known as being effective at enabling peroxide decomposition with negligible formation of hydroxyl radicals and so may possibly contribute to minimize the degradation of the NPMCs when used with Pt as a hybrid ORR catalyst. Therefore, by merging Pt and NPMCs

while attaining the optimum proportion and structural formation, a novel hybrid catalyst could be synthesized with an ORR activity supported by both NPMC active sites and low-loading platinum nanostructure and with enhanced NPMC support durability by promoting peroxide decomposition.

Bibliography

(1) Higgins, D.; Zamani, P.; Yu, A.; Chen, Z. The application of graphene and its composites in oxygen reduction electrocatalysis: a perspective and review of recent progress. *Energy Environ. Sci.* **2016**, *9*, 357-390.

(2) Chung, H.; Wu, G.; Higgins, D.; Zamani, P.; Chen, Z.; Zelenay, P. Heat-Treated Non-precious Metal Catalysts for Oxygen Reduction. **2016**, 41-68.

(3) Bi, E.; Chen, H.; Yang, X.; Peng, W.; Grätzel, M.; Han, L. A quasi core–shell nitrogen-doped graphene/cobalt sulfide conductive catalyst for highly efficient dye-sensitized solar cells. *Energy & Environmental Science* **2014**, *7*, 2637-2641.

(4) Fuel Cell Technical Team Roadmap. http://energy.gov/sites/prod/files/2014/02/f8/fctt_roadmap_june2013.pdf.

(5) Higgins, D. C. Nanostructured oxygen reduction catalyst designs to reduce the platinum dependency of polymer electrolyte fuel cells. *University of Waterloo* **2015**.

(6) Zarrin, H. Novel Polymer Electrolyte Nano-Composite Membranes for Fuel Cell Applications. *University of Waterloo* **2014**.

(7) Hoque, M. A. Advanced Heteroatom Doped Nanocarbon Materials as Platinum catalyst Supports for Fuel Cells. *University of Waterloo* **2016**.

(8) Banham, D.; Ye, S.; Pei, K.; Ozaki, J.-i.; Kishimoto, T.; Imashiro, Y. A review of the stability and durability of non-precious metal catalysts for the oxygen reduction reaction in proton exchange membrane fuel cells. *J. Power Sources* **2015**, *285*, 334-348.

(9) Cheng, F.; Chen, J. Metal-air batteries: from oxygen reduction electrochemistry to cathode catalysts. *Chemical Society Reviews* **2012**, *41*, 2172-2192.

(10) Wu, J.; Yang, H. Platinum-Based Oxygen Reduction Electrocatalysts. *Acc. Chem. Res.* **2013**, *46*, 1848-1857.

(11) Higgins, D. C.; Chen, Z. Recent progress in non-precious metal catalysts for PEM fuel cell applications. *The Canadian Journal of Chemical Engineering* **2013**, *91*, 1881-1895.

(12) Chen, Z.; Higgins, D.; Yu, A.; Zhang, L.; Zhang, J. A review on non-precious metal electrocatalysts for PEM fuel cells. *Energy & Environmental Science* **2011**, *4*, 3167-3192.

(13) Jaouen, F.; Proietti, E.; Lefèvre, M.; Chenitz, R.; Dodelet, J.-P.; Wu, G.; Chung, H. T.; Johnston, C. M.; Zelenay, P. Recent advances in non-precious metal catalysis for oxygen-reduction reaction in polymer electrolyte fuel cells. *Energy & Environmental Science* **2011**, *4*, 114.

(14) Thomas, S.; Zalbowitz, M. Fuel Cells Green Power. **1999**.

(15) EG&G Technical Services, I. Fuel Cell Handbook. *U.S. Department of Energy* **2004**.

(16) Cook, B. An Introduction to Fuel Cells and Hydrogen Technology. *Engineering science and education journal* **2002**.

(17) Wu, J.; Yuan, X. Z.; Martin, J. J.; Wang, H.; Zhang, J.; Shen, J.; Wu, S.; Merida, W. A review of PEM fuel cell durability: Degradation mechanisms and mitigation strategies. *Journal of Power Sources* **2008**, *184*, 104-119.

(18) Kinumoto, T.; Inaba, M.; Nakayama, Y.; Ogata, K.; Umebayashi, R.; Tasaka, A.; Iriyama, Y.; Abe, T.; Ogumi, Z. Durability of perfluorinated ionomer membrane against hydrogen peroxide. *Journal of Power Sources* **2006**, *158*, 1222-1228.

(19) Borup, R.; Meyers, J.; Pivovar, B.; Kim, Y. S.; Mukundan, R.; Garland, N.; Myers, D.; Wilson, M.; Garzon, F.; Wood, D.; Zelenay, P.; More, K.; Stroh, K.; Zawodzinski, T.; Boncella, J.; McGrath, J. E.; Inaba, M.; Miyatake, K.; Hori, M.; Ota, K.; Ogumi, Z.; Miyata, S.; Nishikata, A.; Siroma, Z.; Uchimoto, Y.; Yasuda, K.; Kimijima, K.-i.; Iwashita, N. Scientific Aspects of Polymer Electrolyte Fuel Cell Durability and Degradation. *Chem. Rev.* **2007**, *107*, 3904-3951.

(20) Debe, M. K. Electrocatalyst approaches and challenges for automotive fuel cells. *Nature* **2012**, *486*, 43-51.

(21) M. S. WILSON; S. GOTTESFELD. Thin-film catalyst layers for polymer electrolyte fuel cell electrodes *J Appl Electrochem* **1992**.

(22) James Larminie; Dicks, A. Fuel Cell Systems Explained. *Wiley* **2003**.

(23) Donis, W. R. M. Diagnosis of PEMFC Stack Failures via Electrochemical Impedance Spectroscopy. *University of Victoria* **2002**.

(24) Panha, K. Accelerated Durability Testing via Reactants Relative Humidity Cycling on Polymer Electrolyte Membrane Fuel Cells. *University of Waterloo* **2010**.

(25) Basu, S. Recent Trends in Fuel Cell Science and Technology. *Springer* **2007**.

(26) Office, F. C. T. 2013 Fuel Cell Technologies Market Report. *U.S. Department of Energy* **2013**.

(27) Program, H. a. F. C. 2014 Annual Merit Review and Peer Evaluation Report. *U.S. Department of Energy* **2014**.

(28) Jasinski, R. New Fuel Cell Cathode Catalyst. *Nature* **1964**, *201*, 1212-&.

(29) Wiesener, K. N-4-Chelates as Electrocatalyst for Cathodic Oxygen Reduction. *Electrochimica Acta* **1986**, *31*, 1073-1078.

(30) Baranton, S.; Coutanceau, C.; Roux, C.; Hahn, F.; Leger, J. M. Oxygen reduction reaction in acid medium at iron phthalocyanine dispersed on high surface area carbon substrate: tolerance to methanol, stability and kinetics. *J Electroanal Chem* **2005**, *577*, 223-234.

(31) Ouyang, J. B.; Shigehara, K.; Yamada, A.; Anson, F. C. Hexadecafluoro Phthalocyanines and Octacyano Phthalocyanines as Electrocatalysts for the Reduction of Dioxygen. *J Electroanal Chem* **1991**, *297*, 489-498.

(32) Shi, C.; Steiger, B.; Yuasa, M.; Anson, F. C. Electroreduction of O-2 to H2O at unusually positive potentials catalyzed by the simplest of the cobalt porphyrins. *Inorg Chem* **1997**, *36*, 4294-4295.

(33) Shi, C. N.; Anson, F. C. Catalytic Pathways for the Electroreduction of O-2 by Iron Tetrakis(4-N-Methylpyridyl)Porphyrin or Iron Tetraphenylporphyrin Adsorbed on Edge Plane Pyrolytic-Graphite Electrodes. *Inorg Chem* **1990**, *29*, 4298-4305.

(34) Vanveen, J. A. R.; Visser, C. Oxygen Reduction on Monomeric Transition-Metal Phthalocyanines in Acid Electrolyte. *Electrochimica Acta* **1979**, *24*, 921-928.

(35) Wiesener, K.; Ohms, D.; Neumann, V.; Franke, R. N-4 Macrocycles as Electrocatalysts for the Cathodic Reduction of Oxygen. *Mater Chem Phys* **1989**, *22*, 457-475.

(36) Bezerra, C. W. B.; Zhang, L.; Lee, K.; Liu, H.; Marques, A. L. B.; Marques, E. P.; Wang, H.; Zhang, J. A review of Fe–N/C and Co–N/C catalysts for the oxygen reduction reaction. *Electrochim. Acta* **2008**, *53*, 4937-4951.

(37) Vasudevan, P.; Santosh; Mann, N.; Tyagi, S. Transition-Metal Complexes of Porphyrins and Phthalocyanines as Electrocatalysts for Dioxygen Reduction. *Transit Metal Chem* **1990**, *15*, 81-90.

(38) Zagal, J. H. Metallophthalocyanines as Catalysts in Electrochemical Reactions. *Coordin Chem Rev* **1992**, *119*, 89-136.

(39) Li, W.; Yu, A.; Higgins, D. C.; Llanos, B. G.; Chen, Z. Biologically Inspired Highly Durable Iron Phthalocyanine Catalysts for Oxygen Reduction Reaction in Polymer Electrolyte Membrane Fuel Cells. *J. Am. Chem. Soc.* **2010**, *132*, 17056-17058.

(40) Alt, H.; Binder, H.; Sandsted.G. Mechanism of Electrocatalytic Reduction of Oxygen on Metal-Chelates. *J Catal* **1973**, *28*, 8-19.

(41) Zhang, J. PEM Fuel Cell Electrocatalysts and Catalyst Layers. *Springer-Verlag: London* **2008**.

(42) Fuhrmann, A.; Wiesener, K.; Iliev, I.; Gamburzev, S.; Kaisheva, A. A Contribution to the Characterization of Heat-Treated Electrocatalytically Active Tetramethoxyphenylporphyrinato-Cobalt-Ii. *Journal of Power Sources* **1981**, *6*, 69-81.

(43) Arechederra, R. L.; Artyushkova, K.; Atanassov, P.; Minteer, S. D. Growth of Phthalocyanine Doped and Undoped Nanotubes Using Mild Synthesis Conditions for Development of Novel Oxygen Reduction Catalysts. *Acs Appl Mater Inter* **2010**, *2*, 3295-3302.

(44) Jaouen, F.; Herranz, J.; Lefevre, M.; Dodelet, J. P.; Kramm, U. I.; Herrmann, I.; Bogdanoff, P.; Maruyama, J.; Nagaoka, T.; Garsuch, A.; Dahn, J. R.; Olson, T.; Pylypenko, S.; Atanassov, P.; Ustinov, E. A. Cross-Laboratory Experimental Study of Non-Noble-Metal Electrocatalysts for the Oxygen Reduction Reaction. *Acs Appl Mater Inter* **2009**, *1*, 1623-1639.

(45) Lalande, G.; Tamizhmani, G.; Cote, R.; Dignardbailey, L.; Trudeau, M. L.; Schulz, R.; Guay, D.; Dodelet, J. P. Influence of Loading on the Activity and Stability of Heat-Treated Carbon-Supported Cobalt Phthalocyanine Electrocatalysts in Solid Polymer Electrolyte Fuel-Cells. *J Electrochem Soc* **1995**, *142*, 1162-1168.

(46) Meng, H.; Larouche, N.; Lefevre, M.; Jaouen, F.; Stansfield, B.; Dodelet, J.-P. Iron porphyrin-based cathode catalysts for polymer electrolyte membrane fuel cells: Effect of NH3 and Ar mixtures as pyrolysis gases on catalytic activity and stability. *Electrochim. Acta* **2010**, *55*, 6450-6461.

(47) Lalande, G.; Faubert, G.; Côté, R.; Guay, D.; Dodelet, J. P.; Weng, L. T.; Bertrand, P. Catalytic activity and stability of heat-treated iron phthalocyanines for the electroreduction of oxygen in polymer electrolyte fuel cells. *J. Power Sources* **1996**, *61*, 227-237.

(48) Lefevre, M.; Dodelet, J. P.; Bertrand, P. O-2 reduction in PEM fuel cells: Activity and active site structural information for catalysts obtained by the pyrolysis at high temperature of Fe precursors. *J Phys Chem B* **2000**, *104*, 11238-11247.

(49) Lefevre, M.; Dodelet, J. P.; Bertrand, P. Molecular oxygen reduction in PEM fuel cells: Evidence for the simultaneous presence of two active sites in Fe-based catalysts. *J Phys Chem B* **2002**, *106*, 8705-8713.

(50) Liu, G.; Li, X.; Ganesan, P.; Popov, B. N. Studies of oxygen reduction reaction active sites and stability of nitrogen-modified carbon composite catalysts for PEM fuel cells. *Electrochim. Acta* **2010**, *55*, 2853-2858.

(51) Kramm, U. I.; Abs-Wurmbach, I.; Herrmann-Geppert, I.; Radnik, J.; Fiechter, S.; Bogdanoff, P. Influence of the Electron-Density of FeN4-Centers Towards the Catalytic Activity of Pyrolyzed FeTMPPCl-Based ORR-Electrocatalysts. *J Electrochem Soc* **2011**, *158*, B69-B78.

(52) Matter, P. H.; Zhang, L.; Ozkan, U. S. The role of nanostructure in nitrogen-containing carbon catalysts for the oxygen reduction reaction. *J Catal* **2006**, *239*, 83-96.

(53) Lefevre, M.; Dodelet, J. P.; Bertrand, P. Molecular oxygen reduction in PEM fuel cell conditions: ToF-SIMS analysis of Co-based electrocatalysts. *J Phys Chem B* **2005**, *109*, 16718-16724.

(54) Weng, L. T.; Bertrand, P.; Lalande, G.; Guay, D.; Dodelet, J. P. Surface Characterization by Time-of-Flight Sims of a Catalyst for Oxygen Electroreduction - Pyrolyzed Cobalt Phthalocyanine-on-Carbon-Black. *Appl Surf Sci* **1995**, *84*, 9-21.

(55) Gang Wu; Karren L. More; Christina M. Johnston; Zelenay, P. High-Performance Electrocatalysts for Oxygen Reduction Derived from Polyaniline, Iron, and Cobalt. *Science* **2011**, *332*, 443-447.

(56) Lefevre, M.; Proietti, E.; Jaouen, F.; Dodelet, J.-P. Iron-Based Catalysts with Improved Oxygen Reduction Activity in Polymer Electrolyte Fuel Cells. *Science (Washington, DC, U. S.)* **2009**, *324*, 71-74.

(57) Gang Wu; Zelenay, P. Nanostructured Nonprecious Metal Catalysts for Oxygen Reduction Reaction. *ACCOUNTS OF CHEMICAL RESEARCH* **2013**, *46*, 1878–1889.

(58) Wu, J.; Li, W.; Higgins, D.; Chen, Z. Heat-Treated Nonprecious Catalyst Using Fe and Nitrogen-Rich 2,3,7,8-Tetra(pyridin-2-yl)pyrazino[2,3-g]quinoxaline Coordinated Complex for Oxygen Reduction Reaction in PEM Fuel Cells. *The Journal of Physical Chemistry C* **2011**, *115*, 18856-18862.

(59) Wu, G.; Chen, Z.; Artyushkova, K.; Garzon, F. H.; Zelenay, P. Polyaniline-derived Non-Precious Catalyst for the Polymer Electrolyte Fuel Cell Cathode. *ECS Trans.* **2008**, *16*, 159-170.

(60) Wu, G.; Artyushkova, K.; Ferrandon, M.; Kropf, A. J.; Myers, D.; Zelenay, P. Performance Durability of Polyaniline-derived Non-precious Cathode Catalysts. *ECS Trans.* **2009**, *25*, 1299-1311.

(61) Wu, G.; Mack, N. H.; Gao, W.; Ma, S.; Zhong, R.; Han, J.; Baldwin, J. K.; Zelenay, P. Nitrogen-Doped Graphene-Rich Catalysts Derived from Heteroatom Polymers for Oxygen Reduction in Nonaqueous Lithium–O2 Battery Cathodes. *ACS Nano* **2012**, *6*, 9764-9776.

(62) Bezerra, C. W. B.; Zhang, L.; Liu, H.; Lee, K.; Marques, A. L. B.; Marques, E. P.; Wang, H.; Zhang, J. A review of heat-treatment effects on activity and stability of PEM fuel cell catalysts for oxygen reduction reaction. *Journal of Power Sources* **2007**, *173*, 891-908.

(63) Ohms, D.; Herzog, S.; Franke, R.; Neumann, V.; Wiesener, K.; Gamburcev, S.; Kaisheva, A.; Iliev, I. Influence of metal ions on the electrocatalytic oxygen reduction of carbon materials prepared from pyrolyzed polyacrylonitrile. *J. Power Sources* **1992**, *38*, 327-334.

(64) Peng, H.; Liu, F.; Liu, X.; Liao, S.; You, C.; Tian, X.; Nan, H.; Luo, F.; Song, H.; Fu, Z.; Huang, P. Effect of Transition Metals on the Structure and Performance of the Doped Carbon Catalysts Derived From Polyaniline and Melamine for ORR Application. *ACS Catalysis* **2014**, *4*, 3797-3805.

(65) Proietti, E.; Jaouen, F.; Lefevre, M.; Larouche, N.; Tian, J.; Herranz, J.; Dodelet, J.-P. Iron-based cathode catalyst with enhanced power density in polymer electrolyte membrane fuel cells. *Nat. Commun.* **2011**, *2*, 1427/1421-1427/1429.

(66) Drew Higgins; Zhongwei Chen. Recent Development of Non-precious Metal Catalysts. *Springer* **2013**, *9*, 247-269.

(67) Kramm, U. I.; Lefevre, M.; Larouche, N.; Schmeisser, D.; Dodelet, J.-P. Correlations between Mass Activity and Physicochemical Properties of Fe/N/C Catalysts for the ORR in PEM Fuel Cell via 57Fe Moessbauer Spectroscopy and Other Techniques. *J. Am. Chem. Soc.* **2014**, *136*, 978-985.

(68) Kramm, U. I.; Herranz, J.; Larouche, N.; Arruda, T. M.; Lefevre, M.; Jaouen, F.; Bogdanoff, P.; Fiechter, S.; Abs-Wurmbach, I.; Mukerjee, S.; Dodelet, J.-P. Structure of the catalytic sites in Fe/N/C-catalysts for O2-reduction in PEM fuel cells. *Phys. Chem. Chem. Phys.* **2012**, *14*, 11673-11688.

(69) Stephanie G. Mavilla; Brian J. MacLean; Bradley Easton, E. Preparation and Characterization of Non-Precious Metal Fuel Cell Catalysts via Chemical Modification of Carbon Surfaces. *Electrochemical Society Transaction* **2013**, *53*, 31-41.

(70) Zhao, D.; Shui, J. L.; Grabstanowicz, L. R.; Chen, C.; Commet, S. M.; Xu, T.; Lu, J.; Liu, D. J. Highly efficient non-precious metal electrocatalysts prepared from one-pot synthesized zeolitic imidazolate frameworks. *Advanced Materials* **2014**, *26*, 1093-1097.

(71) Serov, A.; Artyushkova, K.; Andersen, N. I.; Stariha, S.; Atanassov, P. Original Mechanochemical Synthesis of Non-Platinum Group Metals Oxygen Reduction Reaction Catalysts Assisted by Sacrificial Support Method. *Electrochimica Acta* **2015**.

(72) Serov, A.; Artyushkova, K.; Atanassov, P. Fe-N-C Oxygen Reduction Fuel Cell Catalyst Derived from Carbendazim: Synthesis, Structure, and Reactivity. *Adv. Energy Mater.* **2014**, *4*, n/a-n/a.

(73) Serov, A.; Robson, M. H.; Smolnik, M.; Atanassov, P. Tri-metallic transition metal–nitrogen–carbon catalysts derived by sacrificial support method synthesis. *Electrochimica Acta* **2013**, *109*, 433-439.

(74) Tylus, U.; Jia, Q.; Strickland, K.; Ramaswamy, N.; Serov, A.; Atanassov, P.; Mukerjee, S. Elucidating Oxygen Reduction Active Sites in Pyrolyzed Metal-Nitrogen Coordinated Non-Precious-Metal Electrocatalyst Systems. *J Phys Chem C* **2014**, *118*, 8999-9008.

(75) Serov, A.; Robson, M. H.; Artyushkova, K.; Atanassov, P. Templated non-PGM cathode catalysts derived from iron and poly(ethyleneimine) precursors. *Applied Catalysis B: Environmental* **2012**, *127*, 300-306.

(76) Peng, H.; Mo, Z.; Liao, S.; Liang, H.; Yang, L.; Luo, F.; Song, H.; Zhong, Y.; Zhang, B. High Performance Fe- and N- Doped Carbon Catalyst with Graphene Structure for Oxygen Reduction. *Scientific Reports* **2013**, *3*.

(77) Robson, M. H.; Serov, A.; Artyushkova, K.; Atanassov, P. A mechanistic study of 4-aminoantipyrine and iron derived non-platinum group metal catalyst on the oxygen reduction reaction. *Electrochim. Acta* **2013**, *90*, 656-665.

(78) Serov, A.; Robson, M. H.; Smolnik, M.; Atanassov, P. Templated bi-metallic non-PGM catalysts for oxygen reduction. *Electrochimica Acta* **2012**, *80*, 213-218.

(79) Ma, S.; Goenaga, G. A.; Call, A. V.; Liu, D.-J. Cobalt Imidazolate Framework as Precursor for Oxygen Reduction Reaction Electrocatalysts. *Chemistry – A European Journal* **2011**, *17*, 2063-2067.

(80) Chen, Z.; Higgins, D.; Tao, H.; Hsu, R. S.; Chen, Z. Highly Active Nitrogen-Doped Carbon Nanotubes for Oxygen Reduction Reaction in Fuel Cell Applications. *The Journal of Physical Chemistry C* **2009**, *113*, 21008-21013.

(81) Zhang, S.; Zhang, H.; Liu, Q.; Chen, S. Fe-N doped carbon nanotube/graphene composite: facile synthesis and superior electrocatalytic activity. *J. Mater. Chem. A* **2013**, *1*, 3302-3308.

(82) Huang, Z.-M.; Zhang, Y. Z.; Kotaki, M.; Ramakrishna, S. A review on polymer nanofibers by electrospinning and their applications in nanocomposites. *Compos. Sci. Technol.* **2003**, *63*, 2223-2253.

(83) Ramakrishna, S. An Introduction to Electrospinning and Nanofibers. *World Scientific Publishing* **2005**.

(84) Li, D.; Xia, Y. N. Electrospinning of nanofibers: Reinventing the wheel? *Advanced Materials* **2004**, *16*, 1151-1170.

(85) Goldstein, J. Scanning electron microscopy and X-ray microanalysis. *Springer* **2003**.

(86) Egerton, R. F. Electron energy-loss spectroscopy in the TEM. *Reports on Progress in Physics* **2009**, *72*, 016502.

(87) Luo, Z.; Li, D.; Tang, H. L.; Pan, M.; Ruan, R. Degradation behavior of membrane-electrode-assembly materials in 10-cell PEMFC stack. *Int J Hydrogen Energ* **2006**, *31*, 1831-1837.

(88) Ferrari, A. C.; Robertson, J. Interpretation of Raman spectra of disordered and amorphous carbon. *Physical Review B* **2000**, *61*, 14095-14107.

(89) Tuinstra, F.; Koenig, J. L. Raman Spectrum of Graphite. *The Journal of Chemical Physics* **1970**, *53*, 1126-1130.

(90) Weidner, J. W. Membrane Electrode Assembly. *Electrochemical Society Interface* **2003**.

(91) DOE. Technical Plan *Fuel Cells* **2011**.

(92) Zamani, P.; Higgins, D.; Hassan, F.; Jiang, G.; Wu, J.; Abureden, S.; Chen, Z. Electrospun Iron–Polyaniline–Polyacrylonitrile Derived Nanofibers as Non–Precious Oxygen Reduction Reaction Catalysts for PEM Fuel Cells. *Electrochim. Acta* **2014**, *139*, 111-116.

(93) Jaouen, F.; Proietti, E.; Lefevre, M.; Chenitz, R.; Dodelet, J. P.; Wu, G.; Chung, H. T.; Johnston, C. M.; Zelenay, P. Recent advances in non-precious metal catalysis for oxygen-reduction reaction in polymer electrolyte fuel cells. *Energy Environ. Sci.* **2011**, *4*, 114-130.

(94) Wu, J.; Park, H. W.; Yu, A.; Higgins, D.; Chen, Z. Facile Synthesis and Evaluation of Nanofibrous Iron–Carbon Based Non-Precious Oxygen Reduction Reaction Catalysts for Li–O2Battery Applications. *J. Phys. Chem. C* **2012**, *116*, 9427-9432.

(95) Kongkanand, A.; Kuwabata, S.; Girishkumar, G.; Kamat, P. Single-wall carbon nanotubes supported platinum nanoparticles with improved electrocatalytic activity for oxygen reduction reaction. *Langmuir* **2006**, *22*, 2392-2396.

(96) Gong, K.; Du, F.; Xia, Z.; Durstock, M.; Dai, L. Nitrogen-Doped Carbon Nanotube Arrays with High Electrocatalytic Activity for Oxygen Reduction. *Science* **2009**, *323*, 760-764.

(97) Li, W.; Liang, C.; Zhou, W.; Qiu, J.; Zhou; Sun, G.; Xin, Q. Preparation and Characterization of Multiwalled Carbon Nanotube-Supported Platinum for Cathode Catalysts of Direct Methanol Fuel Cells. *The Journal of Physical Chemistry B* **2003**, *107*, 6292-6299.

(98) Higgins, D. C.; Wang, R.; Hoque, M. A.; Zamani, P.; Abureden, S.; Chen, Z. Morphology and composition controlled platinum–cobalt alloy nanowires prepared by electrospinning as oxygen reduction catalyst. *Nano Energy* **2014**, *10*, 135-143.

(99) Park, H. W.; Lee, D. U.; Zamani, P.; Seo, M. H.; Nazar, L. F.; Chen, Z. Electrospun porous nanorod perovskite oxide/nitrogen-doped graphene composite as a bi-functional catalyst for metal air batteries. *Nano Energy* **2014**, *10*, 192-200.

(100) Uhm, S.; Jeong, B.; Lee, J. A facile route for preparation of non-noble CNF cathode catalysts in alkaline ethanol fuel cells. *Electrochimica Acta* **2011**, *56*, 9186-9190.

(101) Shin, D.; Jeong, B.; Mun, B. S.; Jeon, H.; Shin, H.-J.; Baik, J.; Lee, J. On the Origin of Electrocatalytic Oxygen Reduction Reaction on Electrospun Nitrogen–Carbon Species. *The Journal of Physical Chemistry C* **2013**, *117*, 11619-11624.

(102) N. Nakagawa; M. A. Abdelkareem; D. Takino; T. Ishikawa; Tsujiguchi, T. PAN based carbon nanofibers as an active ORR catalyst for DMFC. *ECS Transactions* **2011**.

(103) Qiu, Y.; Yu, J.; Wu, W.; Yin, J.; Bai, X. Fe–N/C nanofiber electrocatalysts with improved activity and stability for oxygen reduction in alkaline and acid solutions. *J Solid State Electrochem* **2012**, *17*, 565-573.

(104) Qiu, Y.; Yin, J.; Hou, H.; Yu, J.; Zuo, X. Preparation of nitrogen-doped carbon submicrotubes by coaxial electrospinning and their electrocatalytic activity for oxygen reduction reaction in acid media. *Electrochim. Acta* **2013**, *96*, 225-229.

(105) Yin, J.; Qiu, Y.; Yu, J. Nitrogen-doped Carbon Nanofibers as Highly Active Metal-free Electrocatalysts for Oxygen Reduction Reactions in Acidic Media. *Chem. Lett.* **2013**, *42*, 413-415.

(106) Yin, J.; Qiu, Y.; Yu, J. Onion-like graphitic nanoshell structured Fe–N/C nanofibers derived from electrospinning for oxygen reduction reaction in acid media. *Electrochem. Commun.* **2013**, *30*, 1-4.

(107) Khomenko, V. G.; Barsukov, V. Z.; Katashinskii, A. S. The catalytic activity of conducting polymers toward oxygen reduction. *Electrochim. Acta* **2005**, *50*, 1675-1683.

(108) Subbiah, T.; Bhat, G. S.; Tock, R. W.; Parameswaran, S.; Ramkumar, S. S. Electrospinning of nanofibers. *J. Appl. Polym. Sci.* **2005**, *96*, 557-569.

(109) Cherevko, S.; Xing, X. L.; Chung, C. H. Electrodeposition of three-dimensional porous silver foams. *Electrochem Commun* **2010**, *12*, 467-470.

(110) Lai, L.; Potts, J.; Zhan, D.; Wang, L.; Poh, C. K.; Tang, C.; Gong, H.; Shen, Z.; Lin, J.; Ruoff, R. Exploration of the active center structure of nitrogen-doped graphene-based catalysts for oxygen reduction reaction. *Energy Environ. Sci.* **2012**, *5*, 7936-7942.

(111) Matter, P. H.; Wang, E.; Ozkan, U. S. Preparation of nanostructured nitrogen-containing carbon catalysts for the oxygen reduction reaction from SiO2- and MgO-supported metal particles. *J Catal* **2006**, *243*, 395-403.

(112) Liu, Q.; Pu, Z.; Tang, C.; Asiri, A. M.; Qusti, A. H.; Al-Youbi, A. O.; Sun, X. N-doped carbon nanotubes from functional tubular polypyrrole: A highly efficient electrocatalyst for oxygen reduction reaction. *Electrochem. Commun.* **2013**, *36*, 57-61.

(113) Higgins, D. C.; Chen, Z.; Chen, Z. W. Nitrogen doped carbon nanotubes synthesized from aliphatic diamines for oxygen reduction reaction. *Electrochim. Acta* **2011**, *56*, 1570-1575.

(114) Fu, X.; Choi, J.-Y.; Zamani, P.; Jiang, G.; Hoque, M. A.; Hassan, F. M.; Chen, Z. Co–N Decorated Hierarchically Porous Graphene Aerogel for Efficient Oxygen Reduction Reaction in Acid. *ACS Appl. Mater. Interfaces* **2016**, *8*, 6488-6495.

(115) Cheng, N.; Banis, M. N.; Liu, J.; Riese, A.; Li, X.; Li, R.; Ye, S.; Knights, S.; Sun, X. Extremely stable platinum nanoparticles encapsulated in a zirconia nanocage by area-selective atomic layer deposition for the oxygen reduction reaction. *Adv Mater* **2015**, *27*, 277-281.

(116) Xia, B. Y.; Wu, H. B.; Li, N.; Yan, Y.; Lou, X. W.; Wang, X. One-Pot Synthesis of Pt–Co Alloy Nanowire Assemblies with Tunable Composition and Enhanced Electrocatalytic Properties. *Angew. Chem. Int. Ed.* **2015**, *54*, 3797-3801.

(117) Higgins, D.; Hoque, M. A.; Seo, M. H.; Wang, R.; Hassan, F.; Choi, J.-Y.; Pritzker, M.; Yu, A.; Zhang, J.; Chen, Z. Development and Simulation of Sulfur-doped Graphene Supported Platinum with Exemplary Stability and Activity Towards Oxygen Reduction. *Adv. Funct. Mater.* **2014**, *24*, 4325-4336.

(118) Su, D. S.; Sun, G. Nonprecious-Metal Catalysts for Low-Cost Fuel Cells. *Angew. Chem. Int. Ed.* **2011**, *50*, 11570-11572.

(119) Fu, X.; Jin, J.; Liu, Y.; Wei, Z.; Pan, F.; Zhang, J. Efficient Oxygen Reduction Electrocatalyst Based on Edge-Nitrogen-Rich Graphene Nanoplatelets: Toward a Large-Scale Synthesis. *ACS Appl. Mater. Interfaces* **2014**, *6*, 3930-3936.

(120) Serov, A.; Robson, M. H.; Halevi, B.; Artyushkova, K.; Atanassov, P. Highly active and durable templated non-PGM cathode catalysts derived from iron and aminoantipyrine. *Electrochem. Commun.* **2012**, *22*, 53-56.

(121) Geng, D.; Chen, Y.; Chen, Y.; Li, Y.; Li, R.; Sun, X.; Ye, S.; Knights, S. High oxygen-reduction activity and durability of nitrogen-doped graphene. *Energy Environ. Sci.* **2011**, *4*, 760-764.

(122) Liu, R.; Wu, D.; Feng, X.; Müllen, K. Nitrogen-Doped Ordered Mesoporous Graphitic Arrays with High Electrocatalytic Activity for Oxygen Reduction. *Angew. Chem. Int. Ed.* **2010**, *49*, 2565-2569.

(123) Byon, H. R.; Suntivich, J.; Shao-Horn, Y. Graphene-Based Non-Noble-Metal Catalysts for Oxygen Reduction Reaction in Acid. *Chem. Mater.* **2011**, *23*, 3421-3428.

(124) Li, S.; Wu, D.; Liang, H.; Wang, J.; Zhuang, X.; Mai, Y.; Su, Y.; Feng, X. Metal–Nitrogen Doping of Mesoporous Carbon/Graphene Nanosheets by Self-Templating for Oxygen Reduction Electrocatalysts. *ChemSusChem* **2014**, *7*, 3002-3006.

(125) Shao, Y.; Zhang, S.; Engelhard, M. H.; Li, G.; Shao, G.; Wang, Y.; Liu, J.; Aksay, I. A.; Lin, Y. Nitrogen-doped graphene and its electrochemical applications. *J. Mater. Chem.* **2010**, *20*, 7491-7496.

(126) Jin, J.; Fu, X.; Liu, Q.; Zhang, J. A highly active and stable electrocatalyst for the oxygen reduction reaction based on a graphene-supported g-C3N4@cobalt oxide core-shell hybrid in alkaline solution. *J. Mater. Chem. A* **2013**, *1*, 10538-10545.

(127) Wang, H.; Maiyalagan, T.; Wang, X. Review on Recent Progress in Nitrogen-Doped Graphene: Synthesis, Characterization, and Its Potential Applications. *ACS Catal.* **2012**, *2*, 781-794.

(128) Jiang, S.; Zhu, C.; Dong, S. Cobalt and nitrogen-cofunctionalized graphene as a durable non-precious metal catalyst with enhanced ORR activity. *J. Mater. Chem. A* **2013**, *1*, 3593-3599.

(129) Pan, F.; Jin, J.; Fu, X.; Liu, Q.; Zhang, J. Advanced Oxygen Reduction Electrocatalyst Based on Nitrogen-Doped Graphene Derived from Edible Sugar and Urea. *ACS Appl. Mater. Interfaces* **2013**, *5*, 11108-11114.

(130) He, C.; Zhang, J. J.; Shen, P. K. Nitrogen-self-doped graphene-based non-precious metal catalyst with superior performance to Pt/C catalyst toward oxygen reduction reaction. *J. Mater. Chem. A* **2014**, *2*, 3231-3236.

(131) Thorum, M. S.; Hankett, J. M.; Gewirth, A. A. Poisoning the Oxygen Reduction Reaction on Carbon-Supported Fe and Cu Electrocatalysts: Evidence for Metal-Centered Activity. *J. Phys. Chem. Lett.* **2011**, *2*, 295-298.

(132) Lee, D. H.; Lee, W. J.; Lee, W. J.; Kim, S. O.; Kim, Y.-H. Theory, Synthesis, and Oxygen Reduction Catalysis of Fe-Porphyrin-Like Carbon Nanotube. *Phys. Rev. Lett.* **2011**, *106*, 175502.

(133) Liang, H.-W.; Wei, W.; Wu, Z.-S.; Feng, X.; Müllen, K. Mesoporous Metal–Nitrogen-Doped Carbon Electrocatalysts for Highly Efficient Oxygen Reduction Reaction. *J. Am. Chem. Soc.* **2013**, *135*, 16002-16005.

(134) Zhang, R.; He, S.; Lu, Y.; Chen, W. Fe, Co, N-functionalized carbon nanotubes in situ grown on 3D porous N-doped carbon foams as a noble metal-free catalyst for oxygen reduction. *J. Mater. Chem. A* **2015**, *3*, 3559-3567.

(135) Parvez, K.; Yang, S.; Hernandez, Y.; Winter, A.; Turchanin, A.; Feng, X.; Müllen, K. Nitrogen-Doped Graphene and Its Iron-Based Composite As Efficient Electrocatalysts for Oxygen Reduction Reaction. *ACS Nano* **2012**, *6*, 9541-9550.

(136) Bo, X.; Li, M.; Han, C.; Zhang, Y.; Nsabimana, A.; Guo, L. Noble metal-free electrocatalysts for the oxygen reduction reaction based on iron and nitrogen-doped porous graphene. *J. Mater. Chem. A* **2015**, *3*, 1058-1067.

(137) Wu, Z.-S.; Yang, S.; Sun, Y.; Parvez, K.; Feng, X.; Mullen, K. 3D Nitrogen–Doped Graphene Aerogel–Supported Fe3O4 Nanoparticles as Efficient Electrocatalysts for the Oxygen Reduction Reaction. *J. Am. Chem. Soc.* **2012**, *134*, 9082-9085.

(138) Zhao, Y.; Hu, C.; Hu, Y.; Cheng, H.; Shi, G.; Qu, L. A Versatile, Ultralight, Nitrogen-Doped Graphene Framework. *Angew. Chem. Int. Ed.* **2012**, *124*, 11533-11537.

(139) Wang, M.; Wang, J.; Hou, Y.; Shi, D.; Wexler, D.; Poynton, S. D.; Slade, R. C. T.; Zhang, W.; Liu, H.; Chen, J. N-Doped Crumpled Graphene Derived from Vapor Phase Deposition of PPy on Graphene Aerogel as an Efficient Oxygen Reduction Reaction Electrocatalyst. *ACS Appl. Mater. Interfaces* **2015**, *7*, 7066-7072.

(140) Vallés, C.; Jiménez, P.; Muñoz, E.; Benito, A. M.; Maser, W. K. Simultaneous Reduction of Graphene Oxide and Polyaniline: Doping-Assisted Formation of a Solid-State Charge-Transfer Complex. *The Journal of Physical Chemistry C* **2011**, *115*, 10468-10474.

(141) Liang, J.; Du, X.; Gibson, C.; Du, X. W.; Qiao, S. Z. N-Doped Graphene Natively Grown on Hierarchical Ordered Porous Carbon for Enhanced Oxygen Reduction. *Adv. Mater.* **2013**, *25*, 6226-6231.

(142) Nabae, Y.; Moriya, S.; Matsubayashi, K.; Lyth, S. M.; Malon, M.; Wu, L.; Islam, N. M.; Koshigoe, Y.; Kuroki, S.; Kakimoto, M.-a.; Miyata, S.; Ozaki, J.-i. RETRACTED: The role of Fe species in the pyrolysis of Fe phthalocyanine and phenolic resin for preparation of carbon-based cathode catalysts. *Carbon* **2010**, *48*, 2613-2624.

(143) Gojković, S. L.; Gupta, S.; Savinell, R. F. Heat-treated iron(III) tetramethoxyphenyl porphyrin chloride supported on high-area carbon as an electrocatalyst for oxygen reduction:: Part III. Detection of hydrogen-peroxide during oxygen reduction. *Electrochim. Acta* **1999**, *45*, 889-897.

(144) Liang, J.; Zheng, Y.; Chen, J.; Liu, J.; Hulicova-Jurcakova, D.; Jaroniec, M.; Qiao, S. Z. Facile Oxygen Reduction on a Three-Dimensionally Ordered Macroporous Graphitic C3N4/Carbon Composite Electrocatalyst. *Angew. Chem. Int. Ed.* **2012**, *51*, 3892-3896.

(145) Pylypenko, S.; Mukherjee, S.; Olson, T. S.; Atanassov, P. Non-platinum oxygen reduction electrocatalysts based on pyrolyzed transition metal macrocycles. *Electrochim. Acta* **2008**, *53*, 7875-7883.

(146) Zamani, P.; Higgins, D. C.; Hassan, F. M.; Fu, X.; Choi, J.-Y.; Hoque, M. A.; Jiang, G.; Chen, Z. Highly active and porous graphene encapsulating carbon nanotubes as a non-precious oxygen reduction electrocatalyst for hydrogen-air fuel cells. *Nano Energy* **2016**, *26*, 267-275.

(147) Jiao, Y.; Zheng, Y.; Jaroniec, M.; Qiao, S. Z. Origin of the electrocatalytic oxygen reduction activity of graphene-based catalysts: a roadmap to achieve the best performance. *Journal of the American Chemical Society* **2014**, *136*, 4394-4403.

(148) Wang, R.; Higgins, D. C.; Lee, D. U.; Prabhudev, S.; Hassan, F. M.; Chabot, V.; Lui, G.; Jiang, G.; Choi, J.-Y.; Rasenthiram, L.; Fu, J.; Botton, G.; Chen, Z. Biomimetic design of monolithic fuel cell electrodes with hierarchical structures. *Nano Energy* **2016**, *20*, 57-67.

(149) Tian, J.; Morozan, A.; Sougrati, M. T.; Lefevre, M.; Chenitz, R.; Dodelet, J.-P.; Jones, D.; Jaouen, F. Optimized Synthesis of Fe/N/C Cathode Catalysts for PEM Fuel Cells: A Matter of Iron-Ligand Coordination Strength. *Angew. Chem., Int. Ed.* **2013**, *52*, 6867-6870.

(150) Armel, V.; Hannauer, J.; Jaouen, F. Effect of ZIF-8 Crystal Size on the O2 Electro-Reduction Performance of Pyrolyzed Fe–N–C Catalysts. *Catalysts* **2015**, *5*, 1333-1351.

(151) Zhao, D.; Shui, J.-L.; Grabstanowicz, L. R.; Chen, C.; Commet, S. M.; Xu, T.; Lu, J.; Liu, D.-J. Highly Efficient Non-Precious Metal Electrocatalysts Prepared from One-Pot Synthesized Zeolitic Imidazolate Frameworks. *Adv. Mater.* **2014**, *26*, 1093-1097.

(152) Higgins, D. C.; Hassan, F. M.; Seo, M. H.; Choi, J. Y.; Hoque, M. A.; Lee, D. U.; Chen, Z. Shape-controlled octahedral cobalt disulfide nanoparticles supported on nitrogen and sulfur-doped graphene/carbon nanotube composites for oxygen reduction in acidic electrolyte. *J. Mater. Chem. A* **2015**, *3*, 6340-6350.

(153) Choi, J.-Y.; Higgins, D.; Jiang, G.; Hsu, R.; Qiao, J.; Chen, Z. Iron-tetracyanobenzene complex derived non-precious catalyst for oxygen reduction reaction. *Electrochim. Acta* **2015**, *162*, 224-229.

(154) Choi, J.-Y.; Higgins, D.; Chen, Z. Highly Durable Graphene Nanosheet Supported Iron Catalyst for Oxygen Reduction Reaction in PEM Fuel Cells. *Journal of The Electrochemical Society* **2012**, *159*, B87-B90.

(155) Choi, J. Y.; Hsu, R. S.; Chen, Z. W. Highly Active Porous Carbon-Supported Nonprecious Metal-N Electrocatalyst for Oxygen Reduction Reaction in PEM Fuel Cells. *J Phys Chem C* **2010**, *114*, 8048-8053.

(156) Ja-Yeon Choi; Ryan Hsu; Chen, Z. Nanoporous Carbon-Supported Fe/Co-N Electrocatalyst for Oxygen Reduction Reaction in PEM Fuel Cells *ECS Transactions* **2010**, *23*, 101-112.

(157) Sahraie, N. R.; Kramm, U. I.; Steinberg, J.; Zhang, Y.; Thomas, A.; Reier, T.; Paraknowitsch, J.-P.; Strasser, P. Quantifying the density and utilization of active sites in non-precious metal oxygen electroreduction catalysts. *Nat Commun* **2015**, *6*.

(158) Park, J.; Mitchel, W. C.; Elhamri, S.; Grazulis, L.; Hoelscher, J.; Mahalingam, K.; Hwang, C.; Mo, S. K.; Lee, J. Observation of the intrinsic bandgap behaviour in as-grown epitaxial twisted graphene. *Nat Commun* **2015**, *6*, 5677.

(159) Huo, X.; Liu, J.; Wang, B.; Zhang, H.; Yang, Z.; She, X.; Xi, P. A one-step method to produce graphene–Fe3O4composites and their excellent catalytic activities for three-component coupling of aldehyde, alkyne and amine. *J. Mater. Chem. A* **2013**, *1*, 651-656.

(160) Zhang, K.; Ang, B. T.; Zhang, L. L.; Zhao, X. S.; Wu, J. Pyrolyzed graphene oxide/resorcinol-formaldehyde resin composites as high-performance supercapacitor electrodes. *Journal of Materials Chemistry* **2011**, *21*, 2663.

(161) Lefèvre, M.; Proietti, E.; Jaouen, F.; Dodelet, J.-P. Iron-Based Catalysts with Improved Oxygen Reduction Activity in Polymer Electrolyte Fuel Cells. *Science* **2009**, *324*, 71-74.

(162) Serov, A.; Artyushkova, K.; Niangar, E.; Wang, C.; Dale, N.; Jaouen, F.; Sougrati, M.-T.; Jia, Q.; Mukerjee, S.; Atanassov, P. Nano-structured non-platinum catalysts for automotive fuel cell application. *Nano Energy* **2015**, *16*, 293-300.

(163) Qingying Jia; Nagappan Ramaswamy; Hasnain Hafiz; Urszula Tylus; Kara Strickland; Gang Wu; Bernardo Barbiellini; Arun Bansil; Edward F. Holby; Piotr Zelenay; Mukerjee, S. Experimental Observation of Redox-Induced Fe-N Switching Behavior as a Determinant Role for Oxygen Reduction Activity. *ACS Nano* **2015**, *9*, 12496-12505.

(164) Kramm, U. I.; Herrmann-Geppert, I.; Bogdanoff, P.; Fiechter, S. Effect of an Ammonia Treatment on Structure, Composition, and Oxygen Reduction Reaction Activity of Fe–N–C Catalysts. *The Journal of Physical Chemistry C* **2011**, *115*, 23417-23427.

(165) Christian L. Mangun; Kelly R. Benak; James Economy; Foster, K. L. Surface chemistry, pore sizes and adsorption properties of activated carbon fibers and precursors treated with ammonia. *Carbon* **2001**, *39*, 1809-1820.

(166) Wang, X.; Lee, J. S.; Zhu, Q.; Liu, J.; Wang, Y.; Dai, S. Ammonia-Treated Ordered Mesoporous Carbons as Catalytic Materials for Oxygen Reduction Reaction. *Chem. Mater.* **2010**, *22*, 2178-2180.

(167) Borup, R.; Meyers, J.; Pivovar, B.; Kim, Y. S.; Mukundan, R.; Garland, N.; Myers, D.; Wilson, M.; Garzon, F.; Wood, D.; Zelenay, P.; More, K.; Stroh, K.; Zawodzinski, T.; Boncella, J.; McGrath, J. E.; Inaba, M.; Miyatake, K.; Hori, M.; Ota, K.; Ogumi, Z.; Miyata, S.; Nishikata, A.; Siroma, Z.; Uchimoto, Y.; Yasuda, K.; Kimijima, K.-i.; Iwashita, N. Scientific Aspects of Polymer Electrolyte Fuel Cell Durability and Degradation. *Chem. Rev.* **2007**, *107*, 3904-3951.

(168) Winter, M.; Brodd, R. J. What Are Batteries, Fuel Cells, and Supercapacitors? *Chem. Rev.* **2004**, *104*, 4245-4270.

(169) Shao, M.; Chang, Q.; Dodelet, J.-P.; Chenitz, R. Recent Advances in Electrocatalysts for Oxygen Reduction Reaction. *Chem. Rev.* **2016**, *116*, 3594-3657.

(170) Hoque, M. A.; Hassan, F. M.; Higgins, D.; Choi, J.-Y.; Pritzker, M.; Knights, S.; Ye, S.; Chen, Z. Multigrain Platinum Nanowires Consisting of Oriented Nanoparticles Anchored on Sulfur-Doped Graphene as a Highly Active and Durable Oxygen Reduction Electrocatalyst. *Adv. Mater.* **2015**, *27*, 1229-1234.

(171) Cheng, N.; Banis, M. N.; Liu, J.; Riese, A.; Li, X.; Li, R.; Ye, S.; Knights, S.; Sun, X. Extremely Stable Platinum Nanoparticles Encapsulated in a Zirconia Nanocage by Area-Selective Atomic Layer Deposition for the Oxygen Reduction Reaction. *Adv. Mater.* **2015**, *27*, 277-281.

(172) Wu, G.; More, K. L.; Johnston, C. M.; Zelenay, P. High-Performance Electrocatalysts for Oxygen Reduction Derived from Polyaniline, Iron, and Cobalt. *Science* **2011**, *332*, 443-447.

(173) Hoon Chung, G. W., Drew Higgins, Pouyan Zamani, Zhongwei Chen and Piotr Zelenay: *Electrochemistry of N4 Macrocyclic Metal Complexes*; Springer,, 2016.

(174) Fu, X.; Zamani, P.; Choi, J.-Y.; Hassan, F. M.; Jiang, G.; Higgins, D. C.; Zhang, Y.; Hoque, M. A.; Chen, Z. In Situ Polymer Graphenization Ingrained with Nanoporosity in a

Nitrogenous Electrocatalyst Boosting the Performance of Polymer-Electrolyte-Membrane Fuel Cells. *Adv. Mater.* **2016**, n/a-n/a.

(175) Wang, Q.; Zhou, Z.-Y.; Lai, Y.-J.; You, Y.; Liu, J.-G.; Wu, X.-L.; Terefe, E.; Chen, C.; Song, L.; Rauf, M.; Tian, N.; Sun, S.-G. Phenylenediamine-Based FeNx/C Catalyst with High Activity for Oxygen Reduction in Acid Medium and Its Active-Site Probing. *J. Am. Chem. Soc.* **2014**, *136*, 10882-10885.

(176) Wu, G.; More, K. L.; Xu, P.; Wang, H.-L.; Ferrandon, M.; Kropf, A. J.; Myers, D. J.; Ma, S.; Johnston, C. M.; Zelenay, P. A carbon-nanotube-supported graphene-rich non-precious metal oxygen reduction catalyst with enhanced performance durability. *Chem. Commun.* **2013**, *49*, 3291-3293.

(177) Fu, X.; Liu, Y.; Cao, X.; Jin, J.; Liu, Q.; Zhang, J. FeCo–Nx embedded graphene as high performance catalysts for oxygen reduction reaction. *Applied Catalysis B: Environmental* **2013**, *130–131*, 143-151.

(178) Chen, Z. W.; Higgins, D.; Yu, A. P.; Zhang, L.; Zhang, J. J. A review on non-precious metal electrocatalysts for PEM fuel cells. *Energy Environ. Sci.* **2011**, *4*, 3167-3192.

(179) Jaouen, F.; Lefèvre, M.; Dodelet, J.-P.; Cai, M. Heat-Treated Fe/N/C Catalysts for O2 Electroreduction: Are Active Sites Hosted in Micropores? *The Journal of Physical Chemistry B* **2006**, *110*, 5553-5558.

(180) Antolini, E. Carbon supports for low-temperature fuel cell catalysts. *Applied Catalysis B: Environmental* **2009**, *88*, 1-24.

(181) Ignaszak, A.; Ye, S.; Gyenge, E. A Study of the Catalytic Interface for O2 Electroreduction on Pt: The Interaction between Carbon Support Meso/Microstructure and Ionomer (Nafion) Distribution. *The Journal of Physical Chemistry C* **2009**, *113*, 298-307.

(182) Zhang, W.; Sherrell, P.; Minett, A. I.; Razal, J. M.; Chen, J. Carbon nanotube architectures as catalyst supports for proton exchange membrane fuel cells. *Energy Environ. Sci.* **2010**, *3*, 1286-1293.

(183) Chen, Z.; Wen, J.; Yan, C.; Rice, L.; Sohn, H.; Shen, M.; Cai, M.; Dunn, B.; Lu, Y. High-Performance Supercapacitors Based on Hierarchically Porous Graphite Particles. *Adv. Energy Mater.* **2011**, *1*, 551-556.

(184) Lu, Y.; Fan, H.; Stump, A.; Ward, T. L.; Rieker, T.; Brinker, C. J. Aerosol-assisted self-assembly of mesostructured spherical nanoparticles. *Nature* **1999**, *398*, 223-226.

(185) Lee, K. T.; Ji, X.; Rault, M.; Nazar, L. F. Simple Synthesis of Graphitic Ordered Mesoporous Carbon Materials by a Solid-State Method Using Metal Phthalocyanines. *Angew. Chem. Int. Ed.* **2009**, *48*, 5661-5665.

(186) Deng, D.; Chen, X.; Yu, L.; Wu, X.; Liu, Q.; Liu, Y.; Yang, H.; Tian, H.; Hu, Y.; Du, P.; Si, R.; Wang, J.; Cui, X.; Li, H.; Xiao, J.; Xu, T.; Deng, J.; Yang, F.; Duchesne, P. N.; Zhang, P.; Zhou, J.; Sun, L.; Li, J.; Pan, X.; Bao, X. A single iron site confined in a graphene matrix for the catalytic oxidation of benzene at room temperature. *Science Advances* **2015**, *1*.

(187) Kudin, K. N.; Ozbas, B.; Schniepp, H. C.; Prud'homme, R. K.; Aksay, I. A.; Car, R. Raman Spectra of Graphite Oxide and Functionalized Graphene Sheets. *Nano Lett.* **2007**, *8*, 36-41.

(188) Charreteur, F.; Jaouen, F.; Dodelet, J.-P. Iron porphyrin-based cathode catalysts for PEM fuel cells: Influence of pyrolysis gas on activity and stability. *Electrochim. Acta* **2009**, *54*, 6622-6630.

(189) Jianlu Zhang, H. Z., Jinfeng Wu, Jiujun Zhang. PEM Fuel Cell Testing and Diagnosis. **2013**.

(190) Saleh FS; Bradley Easton, E. diagnosing degradation within pem fuel cell catalyst layers using electrochemical impedance spectroscopy. journal of the electrochemical society. *Journal of the Electrochemical Society* **2012**, *159*, 546-553.

(191) Group, D. o. E. D. W. Department of Energy Durability Working Group

(192) Nallathambi, V.; Lee, J.-W.; Kumaraguru, S. P.; Wu, G.; Popov, B. N. Development of high performance carbon composite catalyst for oxygen reduction reaction in PEM Proton Exchange Membrane fuel cells. *J. Power Sources* **2008**, *183*, 34-42.

(193) Zamani, P.; Fu, X.; Choi, J.-Y.; Hassan, F. M.; Jiang, G.; Higgins, D. C.; Zhang, Y.; Hoque, M. A.; Chen, Z. In Situ Polymer Graphenization Ingrained with Nanoporosity in a Nitrogenous Electrocatalyst Boosting the Performance of Polymer-Electrolyte-Membrane Fuel Cells. *Adv. Mater.* **2016**, 1604456-n/a.

(194) Rabis, A.; Rodriguez, P.; Schmidt, T. J. Electrocatalysis for Polymer Electrolyte Fuel Cells: Recent Achievements and Future Challenges. *ACS Catal.* **2012**, *2*, 864-890.

(195) Liu, G.; Xu, J.; Wang, T.; Zhao, T.; Wang, M.; Wang, Y.; Li, J.; Wang, X. The performance and mechanism of multi-step activation of MEA for DMFC. *Int. J. Hydrogen Energy* **2010**, *35*, 12341-12345.

(196) Zhang, T.; Cheng, F.; Du, J.; Hu, Y.; Chen, J. Efficiently Enhancing Oxygen Reduction Electrocatalytic Activity of MnO2 Using Facile Hydrogenation. *Adv. Energy Mater.* **2015**, *5*, n/a-n/a.

(197) Fu, X.; Liu, Y.; Cao, X.; Jin, J.; Liu, Q.; Zhang, J. FeCo–Nx embedded graphene as high performance catalysts for oxygen reduction reaction. *Applied Catalysis B: Environmental* **2013**, *130-131*, 143-151.

(198) Gasteiger, H. A.; Marković, N. M. Just a Dream-or Future Reality? *Science* **2009**, *324*, 48-49.

(199) Wang, Y.-C.; Lai, Y.-J.; Song, L.; Zhou, Z.-Y.; Liu, J.-G.; Wang, Q.; Yang, X.-D.; Chen, C.; Shi, W.; Zheng, Y.-P.; Rauf, M.; Sun, S.-G. S-Doping of an Fe/N/C ORR Catalyst for Polymer Electrolyte Membrane Fuel Cells with High Power Density. *Angew. Chem. Int. Ed.* **2015**, *54*, 9907–9910.

(200) Wu, G.; More, K. L.; Xu, P.; Wang, H. L.; Ferrandon, M.; Kropf, A. J.; Myers, D. J.; Ma, S.; Johnston, C. M.; Zelenay, P. A carbon-nanotube-supported graphene-rich non-precious metal oxygen reduction catalyst with enhanced performance durability. *Chemical communications* **2013**, *49*, 3291-3293.

(201) Yang, G.; Choi, W.; Pu, X.; Yu, C. Scalable synthesis of bi-functional high-performance carbon nanotube sponge catalysts and electrodes with optimum C-N-Fe coordination for oxygen reduction reaction. *Energy Environ. Sci.* **2015**, *8*, 1799-1807.

(202) Wu, G.; Nelson, M. A.; Mack, N. H.; Ma, S.; Sekhar, P.; Garzon, F. H.; Zelenay, P. Titanium dioxide-supported non-precious metal oxygen reduction electrocatalyst. *Chem. Commun.* **2010**, *46*, 7489-7491.

(203) Jaouen, F.; Lefevre, M.; Dodelet, J.-P.; Cai, M. Heat-Treated Fe/N/C Catalysts for O2 Electroreduction: Are Active Sites Hosted in Micropores? *J. Phys. Chem. B* **2006**, *110*, 5553-5558.

(204) Chakraborty, S.; Babanova, S.; Rocha, R. C.; Desireddy, A.; Artyushkova, K.; Boncella, A. E.; Atanassov, P.; Martinez, J. S. A Hybrid DNA-Templated Gold Nanocluster For Enhanced Enzymatic Reduction of Oxygen. *J. Am. Chem. Soc.* **2015**, *137*, 11678-11687.